Dissertation

submitted to the
Combined Faculties for the Natural Sciences and for Mathematics
of the Ruperto-Carola University of Heidelberg, Germany
for the degree of
Doctor of Natural Sciences

Presented by
Nicolas Camus
Born in St Doulchard, France

Oral examination: 27.06.2013

Non-sequential double ionization of atoms with phase-controlled ultra-short laser pulses

Referees: **Priv.-Doz. Dr. Robert Moshammer**
Prof. Dr. Andreas Wolf

Summary:

This thesis reports about experimental studies of the non-sequential double ionization of atoms. This mechanism, where an ionized electron, driven by the laser electric field, recollides to further ionize the ion, is investigated using light pulses containing only a few optical cycles. They permit to restrict the interaction time between the laser electric field and the system. The carrier-envelope phase, defining the field-specific shape, is experimentally characterized for every pulse. The coincident detection of the produced ions and electrons is performed using a Reaction Microscope allowing measuring the three-dimensional momentum of each charged particle. The information about the correlated dynamics of the two ionized electrons is extracted. We examine the influence the ionized targets - argon and neon - and the intensity have on these correlations. For argon, by decreasing the intensity of the laser pulses and therefore the electron impact energy, a doubly excited state of the system is formed after recollision. This mechanism is confirmed by semi-classical simulations reproducing the characteristics of our experimental system. Properties of this transition state - such as its decay time - are shown to be strongly correlated to the measured electron momentum. Finally, another experimental realization enabling to control the recolliding electron trajectories is presented.

Zusammenfassung:

Diese Arbeit berichtet über experimentelle Studien zu nichtsequentieller Doppelionisation von Atomen. Dieser Mechanismus, in dem ein ionisiertes Elektron, gelenkt vom elektrischen Feld eines Lasers, mit dem Ion rekollidiert und so weiter ionisiert, wird mithilfe ultrakurzer Laserimpulse untersucht. Dies ermöglicht es, die Interaktionszeit zwischen elektrischem Laserfeld und dem System einzuschränken, um so den Übergangszustand nach der Rekollision zu untersuchen. Die Träger-Einhüllenden-Phasen der Pulse werden experimentell charakterisiert, was bedeutet, dass die Form des elektrischen Feldes von jedem Puls rekonstruiert werden kann. Hierdurch ist es möglich die jeweiligen Trajektorien und Interaktionen, des zu einem bestimmten Feld gehörenden Elektrons, zu studieren. Die koinzidente Messung des doppelt geladenen Ions und der Elektronen wurden mit einem Reaktionsmikroskop vorgenommen, mit dem der dreidimensionale Impuls jedes geladenen Teilchens gemessen werden kann. Der Einfluss des ionisierten Zielobjekts, Argon oder Neon, und der Intensität auf die Korrelation wird außerdem beschrieben. Bei Argon bildet sich, durch Verringerung der Intensität und somit die Stoßenergie der Elektronen, ein doppelt angeregter Zustand des Systems nach der Rekollision. Diese Eigenschaft wird bestätigt mittels einer semi-klassischen Simulation, die die Merkmale des Experiments aufweist. Es wird gezeigt, dass die Eigenschaften des Übergangszustands, wie etwa seine Zerfallszeit, in starker Korrelation mit dem gemessenen Elektron stehen, was Einblicke in dieDynamik erlaubt. Schließlich wird über eine weitere experimentelle Durchführung berichtet, die es ermöglicht, die Trajektorien der rekollidierenden Elektronen zu kontrollieren.

Contents

Introduction

In the 1820s, the first photographic picture taken by Niépce, was obtained by placing a light-sensitive chemical in a "camera obscura" for hours in front of a landscape, revealing for the first time that nature can be recorded with photons. No need to say that the resolution of objects in motion was restrained by this few hours exposure time. Since then the conventional photographic technique has developed and enables temporal resolutions in the order of nanosecond (10^{-9} s). Reaching even shorter time scales and resolving the dynamics of molecular bonds (10^{-15} s) or electronic transitions (10^{-18} s) is achieved only by the utilization of pulsed lasers. Their development is associated with the shortening of the pulse duration down to the attosecond regime (10^{-18} s) as well as a better control of the frequencies and the state of the light, thus entering the field of coherent quantum control.

Lasers are related to a profound quantum mechanical effect: the stimulated emission of radiation. This effect was first discussed by Einstein in a paper on the quantum nature of radiation in 1917 [Ein17]. In order to explain thoroughly Planck's law of black body radiation, stimulated emission has to be considered in addition to the processes of absorption and spontaneous emission of photons associated to a transition between two energy levels. An excited atom/molecule illuminated by a photon emits, within the condition that a given transition is permitted, a photon having the same characteristics (energy and polarization state) as the incident one. It leads to the generation of a beam of spatially and temporally coherent light. The practical realization of such a coherent beam came in 1953 with Charles H. Townes constructing a MASER (Microwave Amplification by Stimulated Emission of Radiation) and few years later, in 1960, its equivalent for visible wavelength (695 nm) was designed by Theodore H. Maiman [Mai60], using a ruby crystal. Considering that this laser light can be pulsed and that the pulses duration is related to the inverse of the laser spectral bandwidth, two directions for improvement were undertaken for different applications:

- In one direction, the development of lasers with the narrowest, most precisely define bandwidth towards performing high resolution spectroscopic measurements.
- In the other direction, the extension of the bandwidth affording a decrease of the pulse duration and with it the time resolution of the processes investigated.

The pulse duration has decreased by several orders of magnitude since the first realization of the laser (figure 1). Different developments in laser science have contributed to this continuous decrease. Until the 90s, the record were set by Q-switching techniques. They enable generation of pulses with solid-state laser having a duration in the order of nanoseconds but were over-passed by mode-locking in dye lasers, which produced as early as 1987, 6 femtoseconds (1 fs = 10^{-15} s) laser pulses after temporal compression [FCBS87]. As shown in figure 1, between 1987 and 2000, the pulse duration did not improve significantly. The utilization of such laser pulses already permitted the time resolved investigation of structural dynamics: molecular rotations (time scale of 10^{-12} s) and vibrations (10-100 fs) and transition states in chemical reactions [Zew88]. These later studies ignited a new field, named femtochemistry, allowing for remarkable new insights into the dynamics of reactions. In 1999, the Nobel prize in Chemistry was awarded to Ahmed Zewail, one of its pioneering contributors [Zew00]. In press releases [Nor13], the utilization of these ultra-fast cameras was compared to "the end of the road" since the temporal resolution achieved is faster than

any chemical reaction and permits the detection of any intermediate state. However, this does not mean the end for the investigation of ultra-fast phenomena. Few years later came the application of the ultra-fast camera to the vibrational dynamics of H_2^+ and D_2^+ [ERF$^+$05, AUT$^+$05, ERF$^+$06], the simplest molecules. Their simplicity is a considerable advantage because it allows for better comparisons with theoretical predictions and extraction of physical information. In contrast, their vibrational motion periods of only 20 fs require stringent experimental conditions.

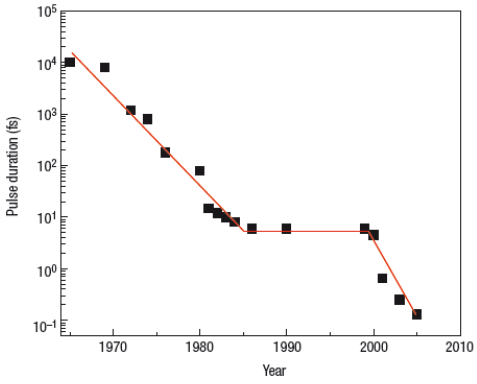

Figure 1: Evolution of the minimum laser pulse duration over the years [CK07].

The laser pulses used in these latter studies already had a duration close to the boundaries of present possibilities with lasers in the visible range, simply because they last only a few optical cycles. One can question whether this measurement scheme is extendable for the detection of electronic dynamics with time scales further down in the attosecond regime? What do we see if we look deeper in the previously mentioned work on molecular reaction or dissociation, is it possible to record the changes in the electronic configuration? If one can access information about one electron, how is it altered by the presence of more electrons? Which role the electronic correlations plays?

Two aspects helped to gain insights on these questions: the possibility to control and shape the electric field of laser pulses with sub-femtosecond precision and the use of the electron recollision mechanism present with strong laser field. Both aspects are intimately related to the development of Titanium:Sapphire (Ti:Sa) lasers. Their development started in the 1980s. Their large bandwidth and the finding of the Kerr Lens Mode-locking (KLM) [SKS91] made them competable in pulse duration with dye lasers. Their main advantage is the laser pulses energy they can deliver. Combined with the Chirped Pulse Amplification scheme [SM85, PM94], such systems can commonly enter the Petawatt intensity regime ($10^{15}\,\mathrm{W/cm^2}$). This high power enables to broaden the spectral bandwidth available through the self-phase modulation in fused silica hollow-core fibers filled with noble gas [NSS96]. Ti:Sa lasers are nowadays table-top systems. They largely contributed to the wide spread of ultra-short laser pulses and the reduction of the time duration towards the single optical cycle at visible wavelength [OK11]. The intensities delivered reach the "strong field" regime. This means that the amplitude of the laser electric field is comparable to the electric field felt by a valence electron in an atom or a molecule due to the Coulomb force. The Coulomb barrier is consequently altered, or even suppressed, and the electron can be ionized. In addition to the influence on the ionization mechanism, the laser field also affects the trajectory of the electron in the continuum and can lead to the observation of electron recollision processes [Cor93] (figure 2). In the first step (A), the electron is tunnel ionized through the lowered Coulomb barrier. In step B) and C), it is driven by the laser field, first away from the ionic core and then back to it until it recollides (D). The energy of the electrons, driven by the laser field, can reached several times the ponderomotive energy where the ponderomotive energy physically corresponds to the maximal energy a free electron at rest can acquire during its quiver motion in an electric field. For example, using a 800 nm laser with an intensity of $2 \cdot 10^{14}\,\mathrm{W/cm^2}$, the maximum kinetic

energy of the returning electron is 1.4 a.u. (38 eV), enough to further ionize an Ar^+ parent ion to Ar^{2+}.

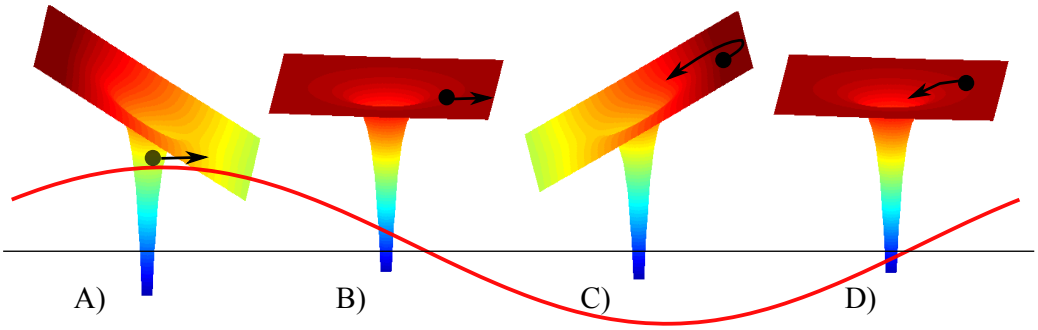

Figure 2: Schematic view of the recollision process over one laser cycle.

Different phenomena rely on electron recollision. The most used and studied process is the recombination of the electron with the ion and the emission of radiation carrying away the excess energy. This radiation extending into the XUV/soft-X-Ray energies is often represented as a burst of light of few hundreds of attoseconds. Isolation of such pulses allows for time resolution in the attosecond entering the field of "attosecond metrology" [HKS$^+$01]. Another phenomenon associated with the recollision is the ionization of the ion under the impact of the electron. This Non-Sequential Multiple Ionization was actually the first reported manifestation of the recollision mechanism with the observation of an increase of the multiple ionization rate in a strong laser field in comparison to the expected rate calculated by tunnel ionization theory [LLMM82, LLMM83, FBCK94, WSD$^+$94, LTC98]. Its investigation was pushed forward by the combination of a Reaction Microscope spectrometer [UMD$^+$03] with strong field laser systems. Detailed information on the momentum of the product fragments could be obtained [MFS$^+$00, WWS$^+$00a, WWS$^+$00b], advocating for the origin of the rescattering in the formation of multiply charged ions over other proposed mechanisms [FBCK92, SLW$^+$98].

The particular case of Non-Sequential Double Ionization (NSDI) is the process studied in the present work. The ion final state is doubly charged and coincident measurements of all fragments involved could be performed [WGW$^+$00, MUF$^+$03, ELR$^+$03, dJRF$^+$04, RdJE$^+$07, SRS$^+$07]. A clear correlation between the two electrons is revealed by the observation of the momentum of one electron as a function of the other electron momentum in a so-called "correlation plot". The studies of these correlation plots helped to identify two main mechanisms for NSDI which are distinguished by the electronic state after recollision. One process is the direct ionization of the ion upon impact of the recolliding electron. This means that the two electrons are freed "together" from the ion and that their mutual interaction can be investigated under no influence of the Coulomb potential of the ion. This is therefore a benchmark system for studying entities where the electronic wave function is delocalized over large distances such as in large molecules or even in solids. The second process is when the ion is only excited by the recollision and is further ionized by the laser pulse with a time delay. This situation offers large prospects concerning the control, the selection and the investigation of given electronic states through laser interaction.

If NSDI represents a privileged process to study the correlation between two electrons compared to other Strong Field processes where the main features can be explained by considering an atom with only one active electron, further questions arise. The aspect that has motivated most effort on NSDI is what state do we obtain right after the recollision and how do we relate it to the correlation plot observed? Can the recolliding electron be also recaptured or does it have the possibility to interact again with the ion, forming multiple recollisions? The problem becomes more complex when taking into account the different intensities used and the different targets to be ionized, increasing the number of possible scenarios to be interpreted.

Over the past few years, two main strategies have been adopted to increase our understanding of the NSDI mechanism. The first one has been to increase available information on the

particles kinematics such as the momentum of the electron transverse to the laser polarization [MFLU+02, WBS+03, WZS+04, RdJE+07]. The second strategy, which is developed in the present thesis, is to confine temporally the NSDI process and the interaction between the ion and the recolliding electron by the employment of ultra-short pulses. This approach has been performed in many theoretical works but only few experimental studies [LRE+04, RZF+04], which did not consider the electron correlations. The utilization of ultra-short pulses permits, independently of the NSDI process, to control efficiently the electric field - and so the electron trajectory - on the sub-femtosecond scale. Such control can be applied to the polarization state of light (direction of the electric field oscillation). It has applications in the optimization of reaction pathways for molecular ionization [BKP+04], the timing of the electron release in ionization [EPC+08, PCS+11b], or even the reduction to only one possible recollision event during a laser pulse [SBC+06]. Alternatively, having a fixed polarization, the control can be performed on the phase of each frequency component. Since the limit of nowadays pulse duration is close to the single-cycle regime, the laser pulses are better described by the electric field they form under the envelope of the pulse. The electric field shape can be defined by the Carrier-Envelope-Phase (CEP), representing the offset between the maximum of the electric field and the maximum of the pulse envelope. This CEP parameter defining the field on the sub-cycle scale depends on the phase of all spectral components of the pulse. Its measurement and stabilization [JDR+00, HUH+00] where made possible through self-referencing techniques which revolutionized the field of frequency metrology and led to the award of the Nobel prize in 2005 to Theodor W. Hänsch and John L. Hall [Hän06, Hal06].

From a stabilized CEP, changes on it are made by introducing a given phase to each spectral component through addition of optical elements. A noteworthy application of this sub-cycle precision is the investigation of electron localization during the dissociative ionization of D_2 and H_2 [KSV+06, KFF+09, FKP+10]. Recently, phase tagging techniques have been developed [WHH+09] which, instead of stabilizing and controlling the CEP, present the experimental advantage of simply measuring it for each pulse. This phase tagging was implemented and used in this work to observe NSDI with ultra-short, CEP-characterized, pulses. Such control on the spectral phase can be extended by splitting the frequency spectrum into different part and treating them separately. Limitations intrinsic to the optical elements properties are avoided and a stronger control on the possible shape of the electric field has been demonstrated [WHG+11, ROA+12]. Similarly, two-color experiments, where a frequency-doubled component is created from the laser and superimposed on the fundamental frequency, have shown the possibility to model in a different way the electric field [XRK+12] and to control the electron recollision trajectory [SSB+12].

The prospect of this thesis is to investigate electron correlation in Non-Sequential Double Ionization by experimentally combining a Reaction Microscope with controlled electric fields. It is organized as follows: the first chapter addresses the common principle about interaction of a molecule or atom with a strong laser fields. First, the different ionization processes in strong laser fields and the mechanism of recollision are reviewed. Second the mechanism of NSDI is considered. Finally the advantage of controlled laser electric fields and their utilization in ionization studies are discussed. Chapter 2 presents the ultra-short laser pulses generation from a commercial Ti:Sa laser, together with characterization methods of these laser pulses. Emphasis is given to the stereo-ATI spectrometer which serves for the phase tagging of single pulse. The two-color Mach-Zehnder type interferometer set-up utilized for the two-color experiment is also described. The main spectrometer, the Reaction Microscope, allowing the recording of the full kinematical information of the reaction products in coincidence is described in chapter 3. In chapter 4, the combination of the phase tagging with the Reaction Microscope is experimentally demonstrated. This permits to obtain experimental correlation plots for NSDI of argon and neon with ultra-short laser pulses. Considering the laser intensity used, their interpretation is viewed in comparison with results reported for longer pulse durations and theoretical results reported with ultra-short laser pulses. In chapter 5, experimental data of NSDI of argon at a different, lower intensity regime is presented together with a semi-classical model developed to interpret the experimental data. In chapter 6, results of a different control experiment performed on the laser electric field through the two-color experiment are reported. Finally, chapter 7 presents a conclusion and an outlook for future experiments.

Chapter 1

Atoms in strong laser fields

In this chapter the general principle of ionization of atoms with strong laser fields (¿ $10^{13}\,\mathrm{W/cm^2}$) is presented. First,the different ionization pictures are described, with a particular focus on the recollision mechanism at the origin of the physical process investigated in the present work: Non-Sequential Double Ionization (NSDI) of atoms which is reviewed in the second part. Since nowadays the pulse duration can be brought to the ultra-short regime (duration of few optical cycles) such that the shape of the electric field can be controlled on the sub-cycle scale, the third part addresses the question why these pulses are an advantage and explains the theoretical perspectives. Unless stated otherwise, units in this chapter are atomic units (a.u.).

1.1 Ionization mechanisms

1.1.1 Single electron processes

When dealing with ionization of atoms in strong laser fields, two pictures appear to describe the mechanism: multi-photon ionization and tunneling ionization. Keldysh [Kel65] gave a convenient description to determine which "regime" is prevalent depending on the ionized target, the wavelength and intensity of the laser pulses. This is compiled in the so-called Keldysh parameter γ:

$$\gamma = \frac{\sqrt{2I_p}}{E_{\mathrm{field}}/\omega}\ , \tag{1.1}$$

where I_p is the ionization potential of the target (e.g. 0.56 a.u. for neutral argon), E_{field} is the laser electric field and ω is the frequency of the laser field (for a 800 nm laser $\omega = 0.058$ a.u.). This factor expresses how the strong field modifies the Coulomb potential. For $\gamma \gg 1$ the electron can be freed by a net absorption of photons (multi-photon picture), while for $\gamma \ll 1$, the Coulomb barrier is modified in such a way that the electron can tunnel (tunneling picture). For ionization of argon at 800 nm in a strong laser field, with typical experimental intensities ranging from $5\cdot10^{13}$ W/cm^2 ($E_{\mathrm{field}} = \sqrt{I} = 0.037$ a.u.) to $2\cdot10^{15}$ W/cm^2 (E_{field}= 0.241 a.u.), the Keldysh parameter goes from 1.65 to 0.25: not a definite regime. Both cases, multi-photon ionization and tunneling, are considered in the following.

Multi-photon ionization

In the multi-photon regime, the ionization is described as the absorption of n photons with $n \in \mathbb{N}$ such that $n\hbar\omega \geq I_p$ as depicted in figure 1.1. The ionization rate for n absorbed photons depends on the intensity I:

$$\omega_n = \sigma_n I^n, \tag{1.2}$$

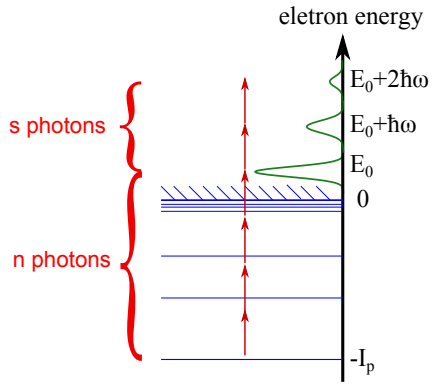

Figure 1.1: Multi-photon ionization: the atom absorb $n + s$ photons from the laser field.

where σ_n is the generalized n-photon cross section. A signature of discrete absorption of photons is the appearance of Above-Threshold Ionization (ATI) peaks [AFM+79]. These are peaks in the electron energy spectrum with an excess energy of $s\hbar\omega$ with $s \in \mathbb{N}$. They are due to the absorption of additional photons by the electron once it is freed but still under the influence of the ion Coulomb potential (otherwise it would not absorb photons). In figure 1.1, photo-electrons are ionized with n photons having an energy $\mathrm{E}_0 = -I_p + n\hbar\omega$. ATI peaks are at energies $\mathrm{E}_0 + s\hbar\omega$. The ionization rate leading to ATI peaks where s-additional photons have been absorbed is:

$$\omega_{n+s} = \sigma_n I^{n+s} \ . \tag{1.3}$$

In the multi-photon picture the Coulomb potential of the target is considered as unchanged. This is no longer valid for higher intensities.

Tunneling ionization

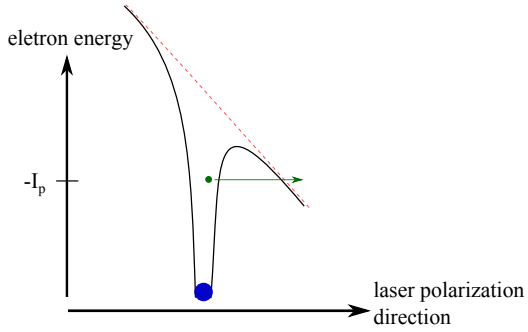

Figure 1.2: Tunneling of the electron through the Coulomb potential.

For a higher intensity such that the electric field created by the laser is of the order of the electric field of an atomic core, the potential of the atom is modified and the electron can tunnel through the Coulomb barrier (figure 1.2). The simplest approximation is to consider the system static and to use the static tunneling rate at the time t_0 [LL77]:

$$\omega_{\mathrm{static}} \propto \exp\left(-\frac{2}{3}\frac{(2I_p)^{3/2}}{|E_{\mathrm{field}}(t_0)|}\right) \ . \tag{1.4}$$

A more complete treatment considering an initial electronic state with orbital and magnetic quantum number m and l, is expressed by the so-called ADK rate [PPt66, ADK86, AMSC91]:

$$\omega_m^{\mathrm{ADK}} = \sqrt{\frac{3E_{field}n^{*3}}{\pi Z^3}}\frac{Z^2}{4\pi n^{*3}}\left(\frac{2e}{n^*}\right)^{2n^*}\left(\frac{2Z^3}{E_{\mathrm{field}}n^{*3}}\right)^{2n^*-|m|-1}\frac{(2l+1)(l+|m|)!}{2^{|m|}(|m|)!(l-|m|)!}\exp\left(\frac{2Z^3}{3E_{\mathrm{field}}n^{*3}}\right) \tag{1.5}$$

where n^* is the effective principle quantum number $n^* = Z/\sqrt{2I_p}$ and Z the charge of the species after ionization.

Over the Barrier Ionization

If the intensity of the laser field is increased even further such that the Coulomb barrier is completely suppressed and the electron is "free" in the laser field, the regime is called Over the Barrier Ionization (OBI). The critical field at which OBI is observed is given by:

$$E_{\mathrm{field}}^{\mathrm{crit}} = \frac{{I_p}^2}{4Z}\ , \tag{1.6}$$

with Z and I_p previously defined. Nonetheless, if this definition holds for a classical barrier where an electrons represents a particle at a given energy which cannot tunnel, this representation is debated when including Stark shifts and the electronic wave function of the initial state in momentum space [AD97]. Also, it has been pointed out that depending on the model used, OBI might not be relevant and do not have to be differentiated from tunneling ionization [PCS+11a].

1.1.2 Multiple ionization and electron recollision

Multiple ionization provides a very convenient way to look for correlations between electrons. The sustaining idea is that, if correlations were absent, the second and further ionizations would happen independently of the first. The equations would be the same as for single ionization except for a larger ionization potential I_p and a final charge state Z. Any deviation from that principle indicates correlation.

The most prominent deviation was found in 1982 by L'Huillier et al. [LLMM82] and was the first step towards the recognition and utilization of the so-called recollision mechanism in strong laser physics. By looking at the ion yield for ionization of krypton by a 1064 nm laser as a function of intensity (figure 1.3, A)) a knee structure was found for multiply charged krypton corresponding to a substantial increase of ionization events for lower intensity in comparison to predictions from the ADK rate. For Kr^{2+} the knee is visible at $1.0 \cdot 10^{13}\mathrm{W/cm^2}$ and for Kr^{3+} at $2.0 \cdot 10^{13}\mathrm{W/cm^2}$. The ionization yield experiment was repeated for different species and wavelengths proofing the presence of a knee structure and an increase of the ionization rate for lower intensities.

Amongst the different interpretations given for this mechanism, the one proposed by Schafer et al. [SYDK93] and Corkum [Cor93], implying the recollision of the electron with the ionic core, was to be generally accepted. This mechanism, also dubbed "three-step model" is represented in figure 2 (in introduction chapter) along one cycle of the electric field.

At a maximum of the laser field an electron is ionized (A), the free electron is driven by the laser field, away (B) and back to the ionic core (C). At the next laser zero crossing (D), the electron recollides with the ionic core. The interaction happening at that moment can be of four types ([KI09]):

1. The electron recombines with the ion. The excess energy of the electron is released by generating high harmonic components of the carrier frequency. This interaction is an efficient way to create intense bursts of light situated in the XUV/soft X-ray region and whose temporal duration can be less than 100 as [GSH+08]. Due to these properties, these sources are more and more used for the study of ultra-short phenomena ([SFK+10, WHG+11]).

2. The electron is elastically back-scattered at the ion. It conserves its energy at the recollision and because the recollision happens close to a zero-crossing of the electric field, which

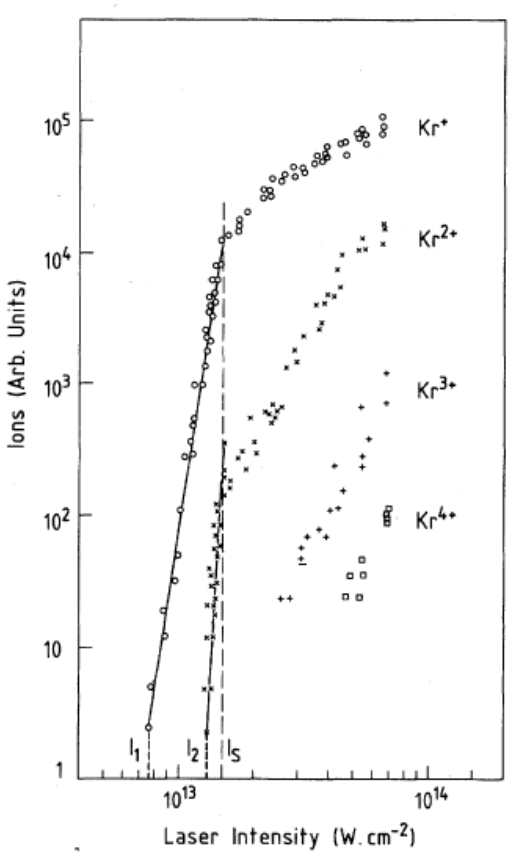

Figure 1.3: Yield of Kr^+, Kr^{2+}, Kr^{3+} and Kr^{4+} as a function of the intensity for ionization by a 1064 nm laser taken from [LLMM82].

changes sign, the electron is further accelerated. This process is called High order Above-Threshold Ionization (HATI) because the electron can reach high energies (few tens of the photon energy). The electrons are a precious tool to characterize ultra-short laser pulses. For instance, they are used in the Stereo-ATI spectrometer (see section 2.3), allowing to determine the carrier envelope phase of the pulses [PGW$^+$01] or their duration [SRM$^+$11a].

3. The electron recollides and is recaptured non-radiatively. It excites the ion but is bound again. This interaction is difficult to observe since the result is a neutral excited atom. The process has however been measured and referred as frustrated tunneling ionization [NGS$^+$08].

4. The electron inelastically recollides and ionizes or induces the ionization of the ion. This process, called Non-Sequential Double Ionization (NSDI), is the origin of the "knee structure" in the yield of the doubly ionized species. The interest in the process is that even though the double ionization rate is low in comparison to the single ionization rate or the high harmonic generation, it offers the possibility to record two electrons and observe their correlated dynamics. The two electrons are freed at the same time at a small distance which allows observing their mutual interaction outside the atomic interaction range.

1.1.3 Double ionization and electron correlation

In order to describe the process of NSDI and to obtain insight into the mechanism, different theoretical approaches are considered. For comparison with experimental results, two observables

are used: the evolution of the ratio of double to single ionization with the intensity and the so-called electron correlation graphs. The correlation plot (figure 1.4) is the longitudinal momentum of one electron $p_{e1||}$ as a function of the longitudinal momentum of the other electron $p_{e2||}$. It can be obtained by using a Reaction Microscope (cf. chapter 3) which permits to record the full kinematical information of the particles in coincidence after interaction with the laser pulse. The experimental graph presented in figure 1.4, was obtained for argon ionized by a 800 nm laser having pulse duration of 220 fs [WGW$^+$00]. Since experimentally no difference can be made between the two electrons, these graphs are symmetrized exploiting either a point like symmetry around the origin of the axes (case of figure 1.4) or along the diagonal $p_{e1||} = p_{e2||}$. The presence of a correlation can be expressed in terms of the momentum distribution function. $\Psi(e_i)$ being the momentum distribution for one electron, a correlation is obtained if $\Psi(e_1, e_2) \neq \Psi(e_1) \times \Psi(e_2)$. For an intensity much higher than the "knee structure" the correlation plot (1.4, B)) resembles a Gaussian function. In this intensity regime the electron momentum distributions seem not to be correlated. This regime is called sequential double ionization (SDI) because the ionization happens in two independent sequential steps[1].

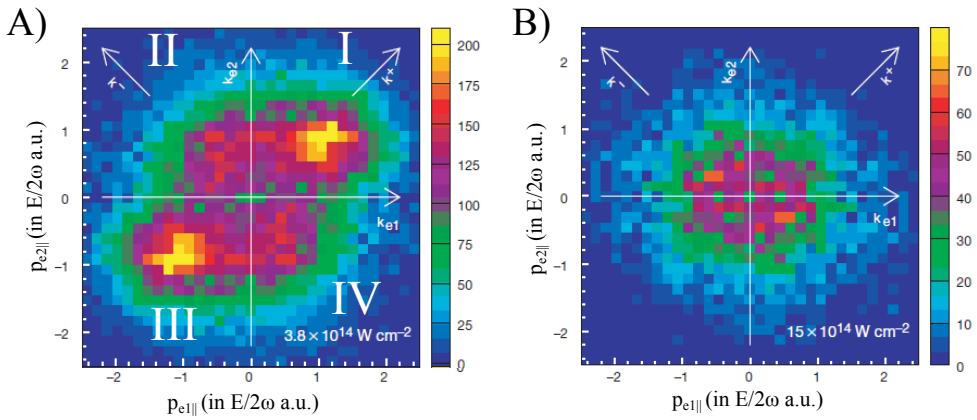

Figure 1.4: Correlation plot for the double ionization of Argon for two different intensities A) $3.4 \cdot 10^{14}$ W/cm^2 B) $1.5 \cdot 10^{15}$ W/cm^2, the pictures where taken from [WGW$^+$00].

For an intensity situated below the knee structure, the pattern is not rotationally symmetrical (1.4, A)). There is a clear correlation between the longitudinal momenta of the two electrons. The first analysis which can be made from such momentum distribution is the relative population of the four quadrants. It indicates how the electrons are leaving the ionic core. Events in the quadrants I and III correspond to electrons escaping the ion in the same direction Events in the quadrants II and IV are cases when the electrons are emitted back to back. To understand more deeply the electron dynamics, theoretical models are essential. They are addressed in the following part.

1.2 Theoretical approaches for double ionization

1.2.1 Quantum mechanical models

Time Dependent Schrödinger Equation

The most straightforward approach is to solve the time dependent Schrödinger Equation (TDSE) in all dimensions. One group has achieved this [PDMT03, PDT$^+$06, PMMT07] for the case of helium ionized at 390 nm. Considering the atom placed at the origin of the coordinate system the Hamiltonian representing the two electron wave function in the presence of the laser field reads:

[1]Nonetheless, this last picture is not so clear as shown by investigation, for this intensity, of spin-orbit wave packet [GLW$^+$10, FWA$^+$11, WC11, WHG$^+$11] or delay between ionization time of the two electrons [PCS$^+$11b], correlations exist, but not as prominent as in NSDI.

$$H = \frac{\mathbf{p_1}^2}{2m_e} + \frac{\mathbf{p_2}^2}{2m_e} + V_1(\mathbf{r}_1) + V_2(\mathbf{r}_2) + V_{12} - e(\mathbf{r}_1 + \mathbf{r}_2) \cdot \mathbf{E}(t) \quad . \tag{1.7}$$

Where $V_n(\mathbf{r}_n) = -\frac{2}{|\mathbf{r}_n|}$ is the binding potential of the electron n at the position $\mathbf{r}_n$, $V_{12} = \frac{1}{\sqrt{(\mathbf{r}_2 - \mathbf{r}_1)^2}}$ is the electron-electron repulsion and $\mathbf{E}(t)$ is the electric field of the laser having a vector potential $\mathbf{A}(t)$. The resulting correlation plot is presented in figure 1.5.

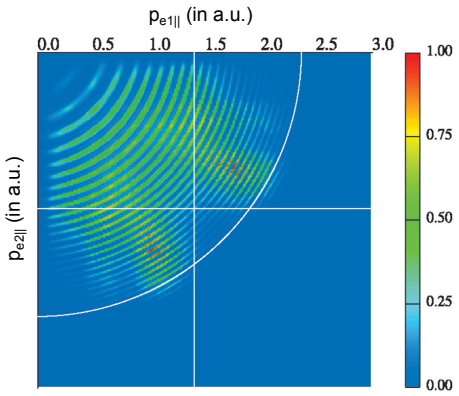

Figure 1.5: Correlation plot for the double ionization of Helium. Theoretical calculation performed for a wavelength of 390 nm and an intensity of 10^{15} W/cm^2, taken from [PDT$^+$06].

TDSE calculations do not permit to look at the system during the interaction which makes it difficult to extract physical picture for the ionization mechanism. However, some features can be extracted and interpreted. The correlation plot exhibits a clear presence of correlation between the two electrons and the presence of NSDI which was not confirmed before at this wavelength. The radial stripes are the signature of absorption of a discrete number of photons equivalently to ATI peaks but for two electrons. The depletion of the distribution along the diagonal echoes the correlated pattern exhibiting a "finger-like structure" identified as an effect of the Coulomb repulsion between the two electrons (more details in section 1.2.2). Though this approach has been realized for helium at a wavelength of 390 nm, it seems for the moment unrealistic to perform such calculations for argon (10 core and 8 valence electrons) at 800 nm, the common experimental investigation of NSDI[2]. Using simplified models also have advantages. They allow to get a more mechanistic view of the problem. The entire interaction is not seen as a single block where given initial conditions (target and laser characteristics) lead to a given correlation plot and where the evolution of the system is opaque. One can look at different intermediate states and their role. For example, in NSDI, different regimes have been pointed out where the state of the system differs after recollision. Having the possibility to look at the system during the interaction allows to select different channels and observe their influence on the final distribution obtained.

The first approximation is to identify different steps within the mechanism. The recollision is divided into three major steps: the first, the tunneling ionization, then the propagation of the electron in the laser field and finally the recollision, the exchange of energy with the ion.

Strong field approximation

The ionization with the ADK rate has been treated in previous section. The propagation in the laser field can be simplified with the Strong Field Approximation (SFA). Two interactions are changed: SFA considers that the bound electron only interacts with the atom but also that the free electron does not feel the binding potential of the atom. In that case the eigenstates for the

[2]for the helium problem at 800 nm, the authors claim in [PDMT03] that it would take 3 years to be run on a normal computer

free electron are known as Volkov states representing a plane wave with momentum $\mathbf{p}$. Their expression follows:

$$\psi_{\mathbf{p}}^{V}(\mathbf{r},t) = |\mathbf{p} + \mathbf{A}(t)\rangle \exp[-iS_{\mathbf{p}}(t)] \tag{1.8}$$

with $|\mathbf{p} + \mathbf{A}(t)\rangle$ a plane wave state

$$\langle \mathbf{r}|\mathbf{p} + \mathbf{A}(t)\rangle = (2\pi)^{-3/2} \exp(i(\mathbf{p} + \mathbf{A}(t)) \cdot \mathbf{r}) \tag{1.9}$$

and $S_{\mathbf{p}}(t)$ the action :

$$S_{\mathbf{p}}(t) = \frac{1}{2}\int^{t} dt'[\mathbf{p} + \mathbf{A}(t')]^2 \quad . \tag{1.10}$$

As stated, splitting the recollision into steps allows distinguishing different paths for the NSDI. When the electron recollides with the ion two main mechanisms have been identified and discussed, depending whether the bound electron is directly ionized ((e,2e)-like ionization) or if it is only promoted to an excited state and ionized by the laser field after some delay. This last mechanism is called Recollision Excitation Subsequent Ionization (RESI). The two mechanisms require therefore a different theoretical treatment as presented with the two transition amplitudes (1.11) and (1.12) (largely described in [FdMFL11]).

In the case of (e,2e)-like ionization the amplitude can be described by:

$$M^{EI}(\mathbf{p}_1, \mathbf{p}_2, t, t') = \int_{-\infty}^{\infty} dt \int_{-\infty}^{t} dt' \left\langle \psi_{\mathbf{p1},\mathbf{p2}}^{V}(t)|V_{12}U_1^V(t,t')V_1U_2^0(t,t')|\psi_g(t')\right\rangle \tag{1.11}$$

where $U_1^V(t,t')$ is the Volkov time evolution operator acting on the electron which gets first ionized and $U_2^0(t,t')$ is the field-free time evolution operator for the second electron. $\psi_g(t')$ is the two electron ground state and $\psi_{\mathbf{p1},\mathbf{p2}}^{V}(t)$ the final state corresponding to the product state of one-electron Volkov states, with asymptotic momenta $\mathbf{p}_1, \mathbf{p}_2$ ([FdMFLSL04, FdMFLBS04]). The time t' corresponds to the ionization time of the first electron recolliding at the instant t. A result obtained with this theoretical treatment is presented in figure 1.6.

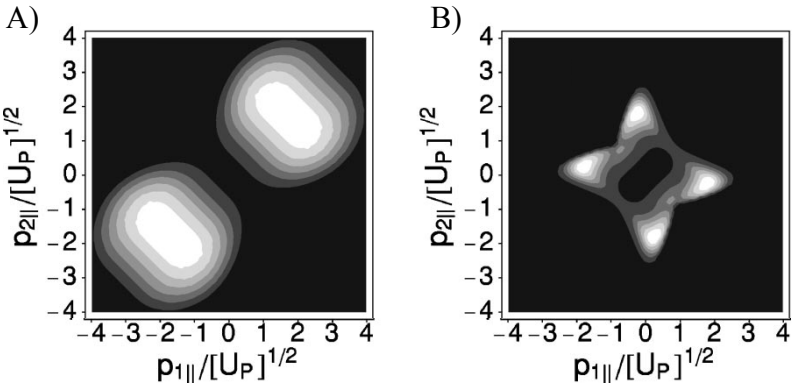

Figure 1.6: Correlation plot for (e,2e)-like ionization for Neon (Ip_1= 0.9 a.u. Ip_2= 1.51 a.u.)and an intensity of 10^{15} W/cm^2, A) The electron-electron interaction V_{12} is a contact interaction, B) V_{12} is a Coulomb potential. Pictures taken from [FdMFLBS04].

Two different electron-electron interactions V_{12} are considered. In the right graph a normal Coulomb potential, on the left graph a three-body contact interaction is used where $V_{12} = \delta(\mathbf{r}_1 - \mathbf{r}_2)$. A radical change between the two types of interaction shows how essential the electronic interactions are in the case of (e,2e)-like ionization. Apart from the influence on the ionization of the second electron and its release in the laser field (this time influences its dynamics in the field and its final momentum), it is commonly assumed that the Coulomb repulsion between the

two electrons disfavors equal momenta leading to a minimum on the diagonal of the correlation plot (corresponding to $p_{e1||} = p_{e2||}$). One feature of the (e,2e)-like mechanism is therefore to be strongly influenced by the electron repulsion as exploited in [RdJE+07] (see section 1.2.2).

For the case of RESI, the transition amplitude is :

$$M^{RESI}(\mathbf{p}_1, \mathbf{p}_2, t, t', t'') = \int_{-\infty}^{\infty} dt \int_{-\infty}^{t} dt'' \int_{-\infty}^{t''} dt' \left\langle \mathbf{p}_1(t), \mathbf{p}_2(t) | V_{ion} \widetilde{U}(t, t'') V_{12} U(t'', t') V | \psi_g^1(t'), \psi_g^2(t') \right\rangle \tag{1.12}$$

where $\widetilde{U}(t, t'')$ and $U(t'', t')$ represent the time evolution operators of the two-electron system, $\left|\psi_g^1(t'), \psi_g^2(t')\right\rangle$ is the initial ground state and $\langle \mathbf{p}_1(t), \mathbf{p}_2(t)|$ the final state with the two electrons in the continuum. V is the atomic binding potential and V_{ion} the potential of the singly ionized core, t' is the tunneling time and t'' the recollision time. The solution and theoretical treatment of equation 1.12 is covered in [SNFdMF10].

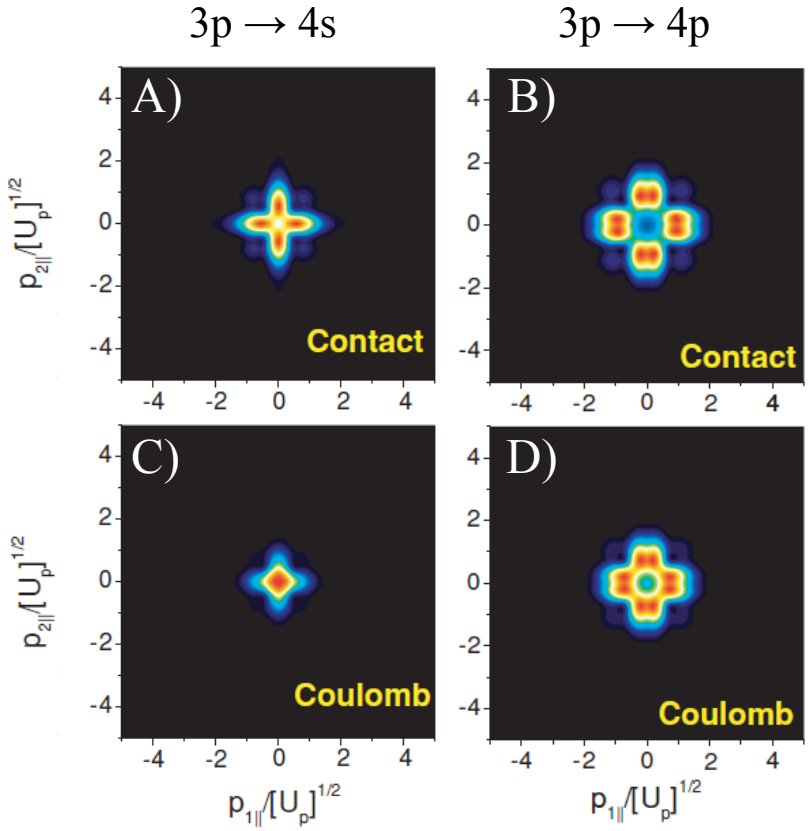

Figure 1.7: Correlation plot for RESI in argon (Ip_1= 0.58 a.u. Ip_2= 1.01 a.u.) at an intensity of $1.5 \cdot 10^{15}$ W/cm^2, A)and B) The electron-electron interaction V_{12} is a contact interaction, C) and D) V_{12} is a Coulomb potential. In A) and C) an excitation of the bound electron to the 4s energy state is considered whereas in B) and D) it is excited to the 4p state. Graphs taken from [SNFdMF10].

For the RESI process the interaction can be also varied as well as the transition state involved (to which state the bound electron is excited). Different results are shown in figure 1.7 for the ionization of argon by $1.5 \cdot 10^{14}$ W/cm^2, 800 nm pulses. The top panels are obtained when a contact interaction is taken between the electrons and the bottom panels when a Coulomb interactions is considered. On the left panels the transition $3p \rightarrow 4s$ is taken for the bound electron, for the

right panels it is $3p \rightarrow 4p$. Due to the delay between the recollision and ionization of the second electron, the electron interaction is less important as seen by the rather similar correlation pattern between Contact and Coulomb interaction. The details of each pattern are linked to the properties of the wave function considered in each transition, but substantial changes can be clearly observed by changing the intermediate state involved.

The changes implied by the model considered and the different interactions or transition-states lead to somewhat very different correlation distributions. This changes show how complicated it is to relate the features of the experimental and theoretical distribution? Experimentally, the different contributions can not be dissociated leading to the overlap of the pattern associated with different process. Disentangling the different contributions from an experimental plot is possible and have been realized [CLL10] but requires to be certain about the correlated graphs (experimental and theoretical ones).

Target dependence

One possibility to differentiate between the processes is to see the influence of the target structure (argument first developed in [dJFZ$^+$04]). Different atoms behave differently under electron impact. By considering the available data for the ionization or excitation of singly charged ions (He^+, Ne^+ and Ar^+) by electron beams, differences can be found. In figure 1.8 the cross-sections for the ionization or excitation of singly charged ions are compiled. This cross-sections can be also detailed for every excitation channel employed [MCLL09, CLML11].

Results show that in the case of argon and helium a prominent RESI mechanism is justified because excitation is more likely than ionization for a broad range of electron energies. On the contrary, in the case of neon the (e,2e)-like mechanism dominates.

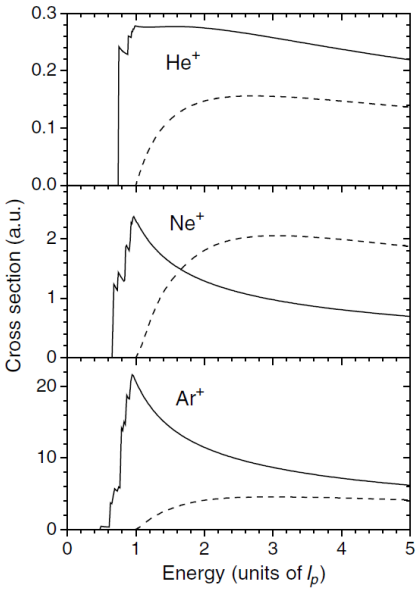

Figure 1.8: Cross section for the excitation (dash lines) and ionization (solid lines) of different singly charged ions as a function of the energy of the colliding electrons (in Ionization Potentials unit). Graphs taken from [dJFZ$^+$04]

This argument is asserted by resembling ion longitudinal momentum distributions of the different ions (1.9). Ion longitudinal momentum distributions are plotted as a function of the atomic species (different rows) and as a function of the intensity such that for each column the value of the maximum energy of the recolliding electron divided by the ionization potential is constant (intensity values in the top left corner of each box in 10^{15} W/cm^2, values of the energy ratio in the

top right corner). Due to momentum conservation all the information visible in these longitudinal momentum distributions are also present in the electron correlation plot (the ion distribution is obtained by projecting the correlation distribution on the $p_{e1||} = p_{e2||}$ diagonal). Nonetheless, less counts and no need for recording electron in coincidence are required, making these information more accessible. For example, for each graph, recording a correlation plot with enough statistics would increase the acquisition time by a factor of 10. For the first three columns the shape of the argon and helium distributions are very similar (the width can not be compared because it scales with the intensities which are not constant over one column) with a slightly pronounced dip in contradiction with neon showing two distinct peaks. A discrepancy is however visible for the last column. The intensity for argon corresponds to the sequential double ionization regime, the associated correlation plot is graph 1.4, B). The observed ion longitudinal momentum distribution is close to a Gaussian (right bottom graph). To be noted, the gray shaded area in each plot indicates the values of momenta expected from the (e,2e)-like process (cf. kinematical consideration in section 1.2.2). Again, a consistency with the cross-sections is found with a momentum distribution in good agreement with (e,2e) conjectures for neon but less agreeing for argon and helium.

This argument connecting the main process with the target is largely employed in literature (cf. review on NSDI [BLHE12]).

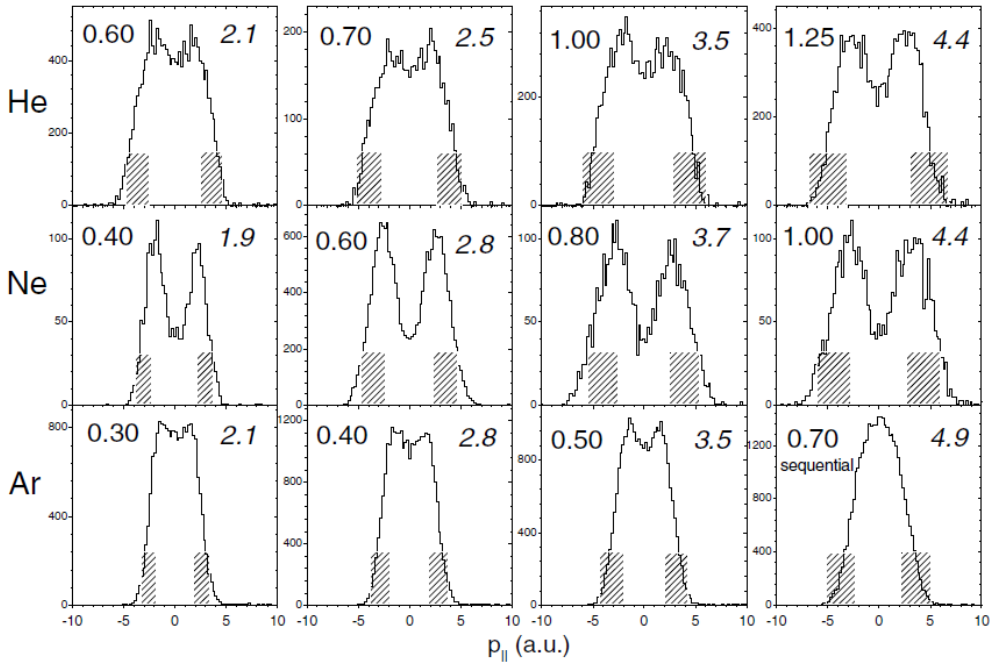

Figure 1.9: Doubly charged ion longitudinal distribution for different target species and different ionization. Each line corresponds to a target as indicated on the left. For each column the ratio of maximum returning kinetic energy by the ionization potential I_p^+ is constant. Graph taken from [dJFZ+04].

1.2.2 Semi-classical models

Description of the model

The theoretical treatment of NSDI can be further approximated with semi-classical simulations. The first step is still considered within the tunnel ionization theory (equation 1.5) describing the

ADK rate[3]. Subsequently, the electron follows a trajectory described by Newton's equations, in atomic units ($m_e = 1/4\pi\epsilon_0 = |e| = 1$) this reads for each electron:

$$\begin{aligned}\frac{d^2 r_i}{dt^2} &= \sum F_{\text{electron}} \\ &= -E_{\text{field}}(t) - \nabla(V_i(r_i) + V_{12}(r_i)) \quad .\end{aligned} \tag{1.13}$$

The $V_i(r_i)$ and $V_{12}(r_i)$ are Coulomb potentials, but "soft-core" potentials can also be used to prevent from having a singularity at zero. Their usual form follows: $V_n(r_n) = -\frac{1}{\sqrt{r_n^2+a^2}}$ and $V_{12} = \frac{1}{\sqrt{(r_2-r_1)^2+b^2}}$. The parameters a and b depend on the target species and on the approximations made (for instance the number of dimensions of the problem). They are calibrated such that the energy levels of the soft-core potential matches literature values. Typically 0.8-2.0 for a and 0.1 for b ([BLHE12]).

The advantages of such models are numerous when considering aspects such as the time and complexity of the computation or the information one may extract. The validity of using a classical model for simulating a quantum system can however be questioned. How to model a RESI mechanism, where the bound electron is excited and is tunnel ionized later by the laser field? A semi-classical model can implement some quantum "ingredients": the possibility for the bound electron to be excited to discrete energy levels, reflecting the energy values given by the literature for the ion, and the possibility for an excited electron to tunnel-ionize following once more the ADK rate.

In favor of the usage of classical models is the fact that they are able to reproduce the knee structure. Figure 1.10 presents the ionization yields of singly and doubly charged helium by a 800 nm laser for different calculations (different semi-classical calculations of NSDI). Experimentally, the knee structure is located at an intensity of $2 \cdot 10^{15}$ W/cm^2 [WSD$^+$94]. If the agreement with theory may not always be striking, the appearance of the knee structure is doubtless. Amongst the different models the one of picture A) from [Cor93] is considered as one of the pioneering theoretical papers on the recollision mechanism, treating the problem classically. It was explaining the main features (knee structure, High Harmonic Generation cutoff). Additionally, one should note picture C) where the calculations are fully classical. In the different calculations, the knee structure can be reproduced, showing that the electronic correlation can be partly revealed by considering the classical behavior of the particles.

The other important observable for NSDI, the correlation plot, was also found in good agreement with classical models. In [PEH01], a first comparison with the quantum model was made bearing good results. Also, as treated in the part concerning helium NSDI, semi-classical models convincingly reproduce the finger-like structure seen in the correlation plot, advocating the possibility of extracting information from such models.

kinematical considerations

As mentioned previously, one of the advantages of semi-classical models is the access to more information during the laser interaction (electron energies and positions) and the possibility to further divide the process into steps. This can be applied to analyze the energy an electron acquires in the field and the kinematical constraints on the correlation plot for each process. Considering an electron ionized at the time t_0, its momentum at the time t, $\vec{P}_e(t, t_0)$, without Coulomb potential, can be expressed through the sum

$$\vec{P}_e(t, t_0) = \vec{P}_{\text{initial}} + \vec{P}_{\text{drift}}(t, t_0) \ . \tag{1.14}$$

$\vec{P}_{\text{initial}}$ is the initial momentum of the electron in the laser field. If the electron is simply ionized by the field, the common assumption is that $\vec{P}_{\text{initial}}$ is zero in the longitudinal direction. In the

[3]For consistency should be mentioned that models being fully classical exist (e.g. [HPHE05]) and where the first step is therefore not a tunnel ionization

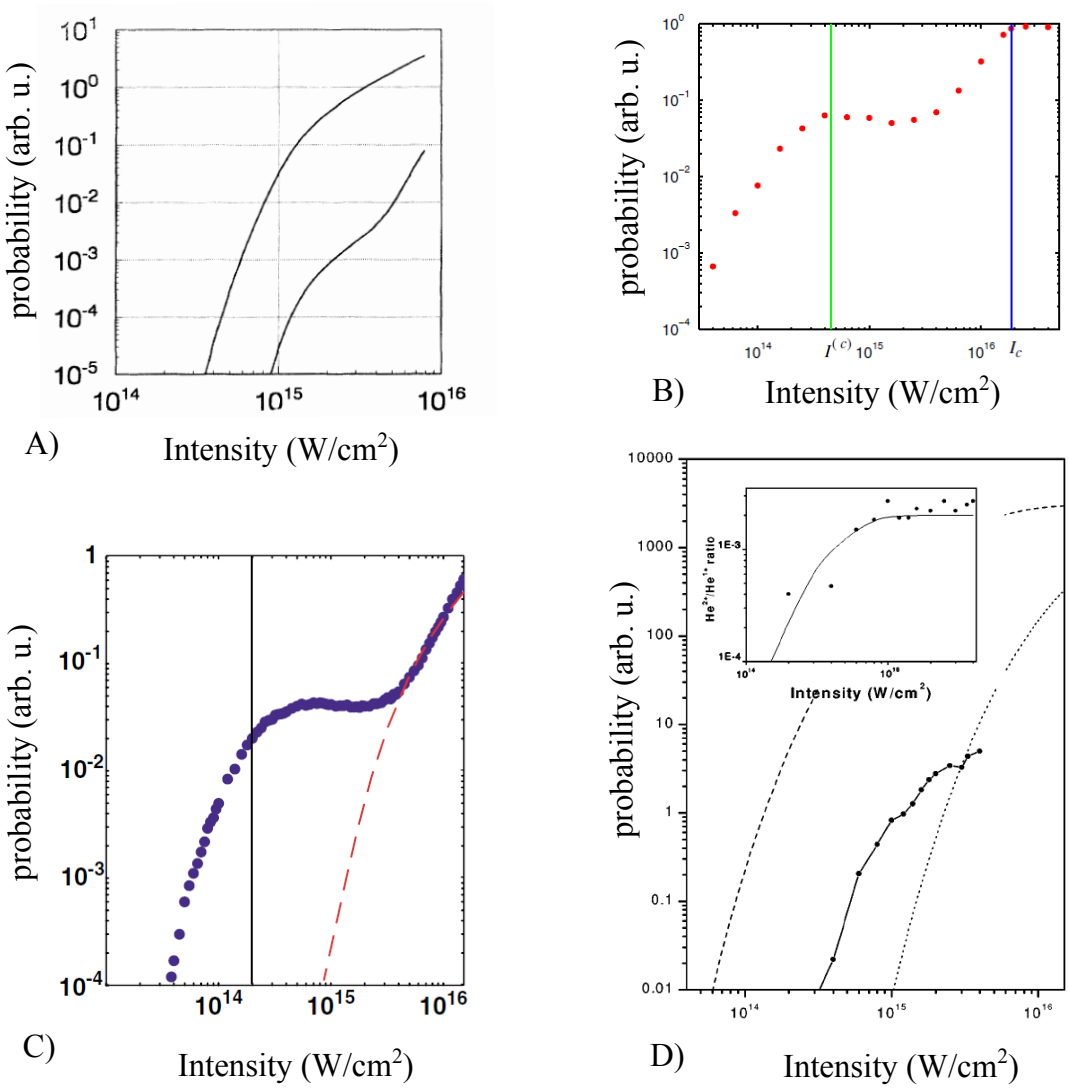

Figure 1.10: Different knee structures obtained in semi-classical models. A) Theoretical probability for single (upper curve) and double ionization of helium taken from [Cor93]. B) Double ionization probability of helium taken from [MCU09], the green line indicates the intensity where the yield of NSDI should be maximum and the blue line where it should completely disappear. C) Double ionization probability of helium taken from [HPHE05], the model used here is fully classical. D) Dashed and dotted lines correspond to the ADK rates for ionization of respectively He and He^+, the solid lines represent the experimental data and the point the theoretical data. Taken from [FLCC01].

transverse direction it has a distribution centered around zero and reproduced by the ADK theory [DK91]. In the case of ionization due to recollision, $\vec{P}_{\text{initial}}$ can be non-zero due to energy sharing between the two electrons.

$\vec{P}_{\text{drift}}(t, t_0)$ is the momentum that the electrons acquires from the laser field, in the laser polarization direction. It depends on the strength and shape of the electric field and the moment t_0 of ionization. Its value $P_{\text{drift}}(t, t_0)$ can be related to the value of the vector potential A of the laser field ($E(t) = -\frac{\partial A(t)}{\partial t}$) through:

$$\begin{aligned} P_{drift}(t, t_0) &= -|e| \int_{t_0}^{t} E(t')dt' \\ &= -|e|[A(t_0) - A(t)] \end{aligned} \tag{1.15}$$

To quantify the energy an electron acquires in the field, it is useful to define the unit $\mathrm{U}_p = I/(4\omega^2)$ (equation in a.u.). This is named the ponderomotive energy and represents the maximum energy an electron has during its quivering motion in a laser wave of frequency ω and intensity I.

In the case the electron does not recollide after being freed (no exchange of energy), the momentum seen at the detector (at $t = +\infty$) is $P_{e,\text{final}}(t_0) = -|e|[A(t_0) - A(+\infty)]$. With the vector potential defined as zero when no laser is present $A(+\infty) = 0$, the momentum of the electron is simply $-|e|A(t_0) = -A(t_0)$ (having a maximum value of $2\,\mathrm{U}_p$) and depends on the time of ionization. This property is the basis for streaking techniques, where the ionization times can be related to the momentum of the recorded electron. It allows to extract properties about the laser pulses [KGU+04] or information about the tunneling time [EPC+08]. The vector potential is highest when the electric field is zero and zero at a maximum of an electric field. The dependence on the ionization time for a recolliding electron ionized in a monochromatic field is described in figure 1.11. Times are expressed in units of the laser period T where at time $t = 0.0\,T$, a maximum of the field is present (following maximum at a phase of $0.5\,T$). The zero-crossings of the field are therefore at $0.25\,T$ and $0.75\,T$.

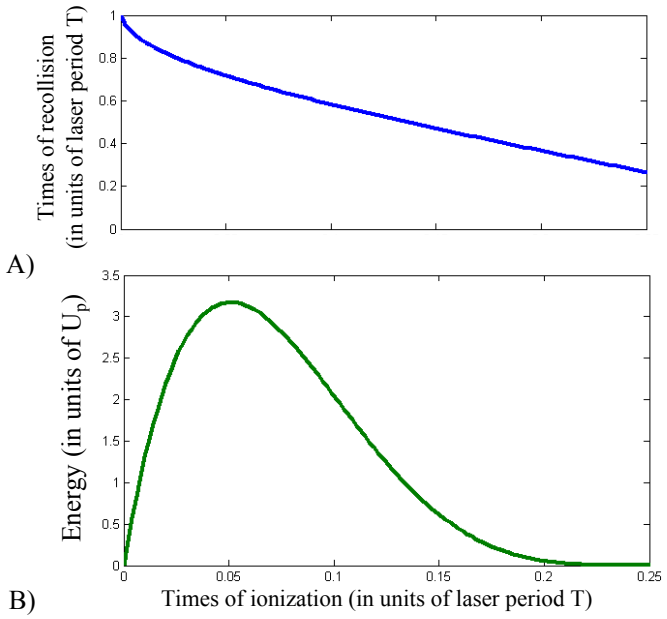

Figure 1.11: Recollision time (A) and energy (B) as a function of the ionization time. The observables are calculated using classical trajectories, without Coulomb potential, in a monochromatic field.

Classical trajectories of electrons, without the influence of the Coulomb field, set free between 0.25 and $0.5\,T$ do not recollide. With the periodicity of the laser, the same kinematics is obtained for ionization between 0.5 and 1.0 T and between 0.0 and $0.5\,T$. Nonetheless, since the laser field has an opposite sign, the electron starts propagating in the opposite direction. In panel A) the time of recollision as a function of the ionization time is shown. The curve shows that the trajectories recolliding close to a zero of the field ($0.75\,T$) are the ones where the electron is ionized close to $0.05\,T$. Knowing the time of recollision enables to extract the energy of the recolliding electron as shown in figure B). The maximum energy is important, it indicates how much energy the electron can exchange with the ion and whether it is sufficient to further ionize the ion ($E_{\mathrm{rec}}^{\mathrm{max}} > I_{p,2}$) or excite it. In the simple case of a monochromatic field: $E_{\mathrm{rec}}^{\mathrm{max}} = 3.17\,U_p$. This maximum energy $E_{\mathrm{rec}}^{\mathrm{max}}$ corresponds to trajectories where the electron is ionized right after $0.05\,T$ and therefore recollides shortly before the zero-crossing of the laser field. From this consideration, it is approximated that in NSDI, the contributing trajectories recollide close to a zero-crossing.

In the case the electron is elastically back-scattered on the ion $\vec{P}_e(t_{\mathrm{rec}} + \epsilon) = -\vec{P}_e(t_{\mathrm{rec}} - \epsilon)$, the final energy of the electron can be as high as $10\,U_p$. This large value is experimentally an advantage because it permits to identify these electrons in comparison to the direct ionized ones.

Two different kinematical constraints are present when considering (e,2e)-like impact ionization or RESI ionization. Looking at these constraints with the mechanisms and associating region of momentum in the correlation plot was first motivated in [FMF+01]. Again, the graph is symmetrized with respect to the $p_{e1||} = p_{e2||}$ diagonal to follow the experimental limitation that we can not distinguish between the first and the second electron.

In (e,2e)-like ionization the allowed regions (figure 1.12, A)) are defined by two circles centered around the points ($X = \pm P_{\mathrm{drift}}(t_{\mathrm{rec}}), Y = \pm P_{\mathrm{drift}}(t_{\mathrm{rec}})$) and having a radius of $\sqrt{2E_{\mathrm{exc}}}$. $P_{\mathrm{drift}}(t_{\mathrm{rec}})$ is the momentum that each electron gains from the laser field after recollision (t_{rec} the time of recollision). Since t_{rec} is close to a zero-crossing of the laser field $A(t_{\mathrm{rec}})$ is taken as constant and equal to $2\sqrt{U_p}$ and so $P_{\mathrm{drift}}(t_{\mathrm{rec}}) = P_{\mathrm{drift}} = 2\sqrt{U_p}$. E_{exc} is the excess energy $E_{\mathrm{exc}} = E_{\mathrm{rec}} - I_{p,2}$ that the two electrons share at the moment of recollision ($I_{p,2}$ is the second ionization potential). It follows that the populated quadrants from (e,2e)-like mechanisms are preferentially quadrants I and III, where the emission direction of the two electrons is the same.

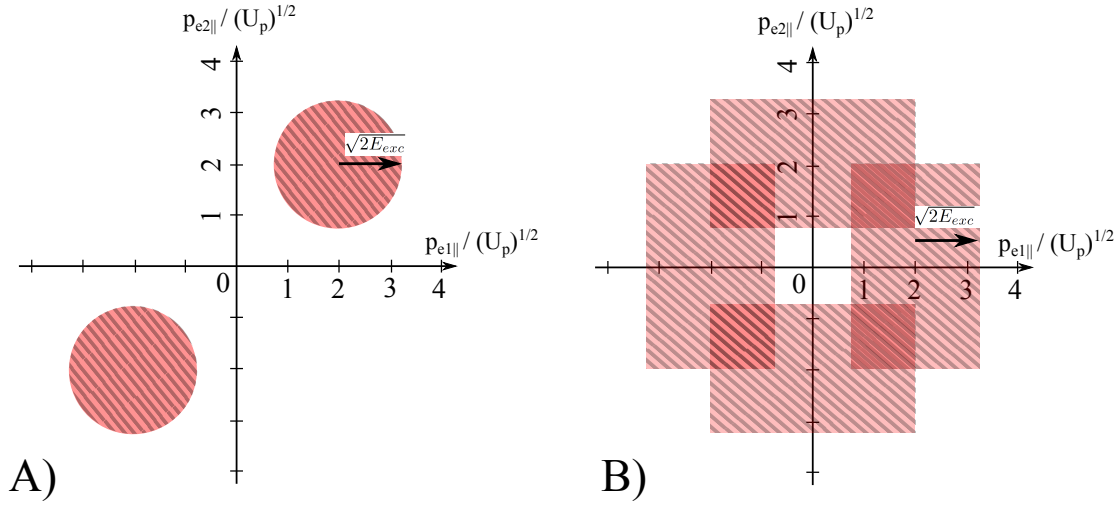

Figure 1.12: Correlation plot expected for different NSDI mechanism A) area covered by the distribution when a (e,2e)-like ionization is assumed B) area when a RESI ionization is assumed.

In the case of RESI, the recolliding electron excites the ion which is subsequently ionized in the laser field at a later time $t_{2,\mathrm{ioniz}}$. The final momentum of the recolliding electron is expressed in the same way than for the previous case: $2\sqrt{U_p} - \sqrt{2E_{\mathrm{exc}}} < |\vec{P}_{e_1,\mathrm{final}}| < 2\sqrt{U_p} + \sqrt{2E_{\mathrm{exc}}}$, the

sign of the momentum is defined by the direction of emission of the electron. For the tunneling electron $P_{e_1,\text{final}} = -|e|A(t_{2,\text{ioniz}})$, with $A_{\max} = 2\sqrt{U_p}$ we obtain : $-2\sqrt{U_p} < P_{e_2,\text{final}} < 2\sqrt{U_p}$. The area covered by this process is shown in figure (1.12, B)). The four quadrants are equally populated.

Multiple recollisions

This separation between the constraints on the longitudinal momentum outlines the interest of using classical models to distinguish the processes. Another feature appears to be important in connection with the classical model. It is the presence of multiple recollisions (figure 1.13) and can be revealed by studying the energy or the position of the electron over time. The pictures are taken from [MCU10a], a semi-classical 1-dimensional model is used with a soft-Coulomb potential (a=b=1). The pulse length is eight cycles, at 800 nm. In figure A) the position of the two electrons (in atomic units) is shown as a function of the laser field (in unit of laser cycles l.c.). The red trajectory corresponds to the first electron ionized, which moves freely in the laser field. The blue curve represents the position of the bound electron, oscillating around zero. At certain times the free electron recollides, comes back to zero where some energy is exchanged with the bound electron visible by the change of its oscillation amplitude until finally the bound electron gets ionized (around 5.0 l.c.). Graph B) shows the number of recollisions for all events (blue distribution) and for the double ionization event (green distribution). For this model, the distribution clearly indicates multiple recollision scenarios. To observe NSDI, more than one recollision is necessary in more than 97% of all cases with the number of recollisions peaking at 3.

Observations of multiple recollisions is not isolated to this study, in most semi-classical models treating NSDI with long laser pulses (pulses duration > 20 fs) this features has been seen. In [LYL$^+$10], each recollision participates in the excitation of the bound electron which can be ionized directly at the next recollision (similar to a (e,2e)-like process) or by the field through tunneling (similar to RESI). Such multiple recollisions actually raise further questions. They change the kinematical constraints drastically: the recolliding electron does not need to have an energy superior to $I_{p,2}$ to further ionize the ion during the impact. It has also implications in the modeling of the process: many simulations consider only one possible recollision (cf. section 1.2.1), are they relevant?

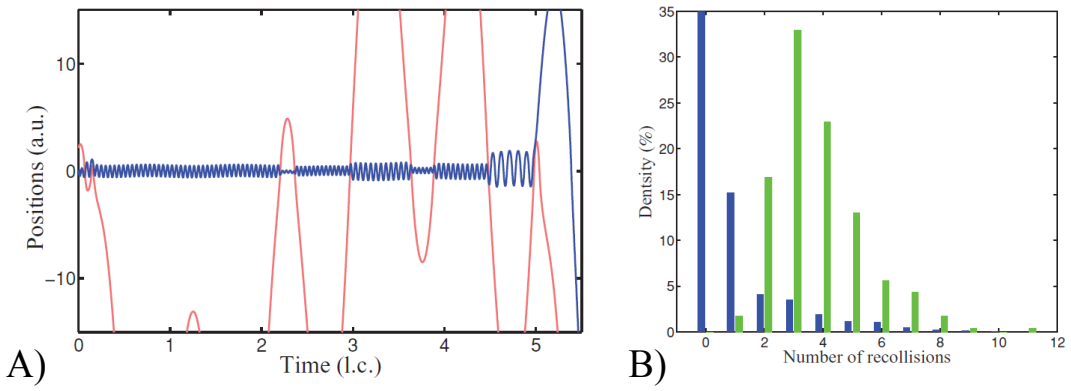

Figure 1.13: A) Position of the two electrons as a function of the time (in unit of laser cycles l.c.) B) Number of recollision events for all trajectories (blue bars), for the double ionization trajectories (green bars) taken from [MCU10a].

Electron correlation for helium

To conclude this section on electron correlations in NSDI, the finger-like (or V-shaped) structure has to be discussed. This is the observation of a depletion of the correlated distribution from the $p_{e1||} = p_{e2||}$ diagonal which was identified in independent experiments for NSDI of helium at different intensities, $0.5 \cdot 10^{15}$ W/cm^2 in [dJRF$^+$04, SRS$^+$07], and $1.5 \cdot 10^{15}$ W/cm^2 in [RdJE$^+$07]. The correlation plots are displayed in figure 1.14 (respectively A), B) and C)). The pattern of the full TDSE calculations [PDT$^+$06] presented in figure 1.5 is also interpreted as a finger-like structure. These features were the focus of many theoretical works.

One argument to discriminate between the processes involved has been to look at electron repulsion, when possible following the work presented for neon in [WZS$^+$04]. In an (e,2e)-like process, the two electrons are in the laser field at the same time and show strong signs of Coulomb repulsion. Consequently, if their longitudinal momentum is similar (data points close to the $p_{e1||} = p_{e2||}$ diagonal), repulsion is visible in the transverse momentum. This features was observed in [RdJE$^+$07] for the events of the finger-like structure implying an (e,2e)-like mechanism responsible. Nonetheless, the similar analysis in [dJRF$^+$04] does not agree with this interpretation. In [PDT$^+$06], the intensity of the laser being $1.0 \cdot 10^{15}$ W/cm^2 and the wavelength being 390 nm, the energy of the returning electron is not sufficient to induce an impact ionization (without multiple recollisions). A semi-classical model has reproduced (quite thoroughly) the finger-like structure and more specifically the experimental correlation plot shown in panel B). The result, from [YLL08] is shown in panel D). Only the anti-correlated electrons (population in quadrants II and IV) are underestimated. In the graph, the black square limits the maximum momentum ($2\sqrt{U_p}$) an ionized electron can acquire in a laser field without interaction. Events outside this square point towards electron interactions. A similar approach than shown in figure 1.6 is done to investigate the interaction's importance: changing the potential. Using a modified electronic potential (not a contact but a Yukawa potential: $V_{12} = \exp(-5.0.r_b)/r_b$ where $r_b = \sqrt{|r_1 - r_2|^2 + 0.2^2}$) leads to counts located on the diagonal implying that the interaction/repulsion between the two electrons is responsible for the finger-like pattern. Investigation of electron repulsion via transverse momentum also indicates an (e,2e)-like process for the structure. This interpretation, that events in quadrants I and III, along the diagonal, are due to (e,2e) is in agreement with the kinematical constraints and the correlation plots obtained from quantum model introduced in section 1.2.1. However, some theoretical studies [HBKE06, XYL10] also indicates a time delay between recollision and ionization (RESI mechanism) for events populating this part of the correlation graph.

The electron correlation plots represent the best observable for studying the NSDI processes. Efforts have been made to interpret the features present and to associate them with a given regime/process. However, the extraction of information reveals to be complicated as shown with the finger-like structures. Semi-classical models prove to be able to reproduce the features observed and permit a to look deeper into the mechanism.

In order to obtain more insights about NSDI, two experimental schemes are proposed. The first scheme is to restrict the temporal interaction between the laser pulses and the atoms. The second is to control the electric field of the laser pulse and relate the kinematical observations with the field. Both aspects can be covered by the utilization of ultra-short laser pulses. The utilization of a two-color field ("sculptured pulses") also permits a different but also large control of the electric field. This two utilizations are treated in the following sections.

1.3 Double ionization studies with few-cycle laser pulses

Definition of the Carrier-Envelope Phase

Dealing with ultra-short laser pulses implies that we approach the boundary, where a limited number of optical cycles are involved, such that the shape of the electric field plays an important role in the ionization process. One additional laser parameter has to be introduced: the carrier envelope phase (CEP, mathematically described as φ_{CEP}). It corresponds to the offset between

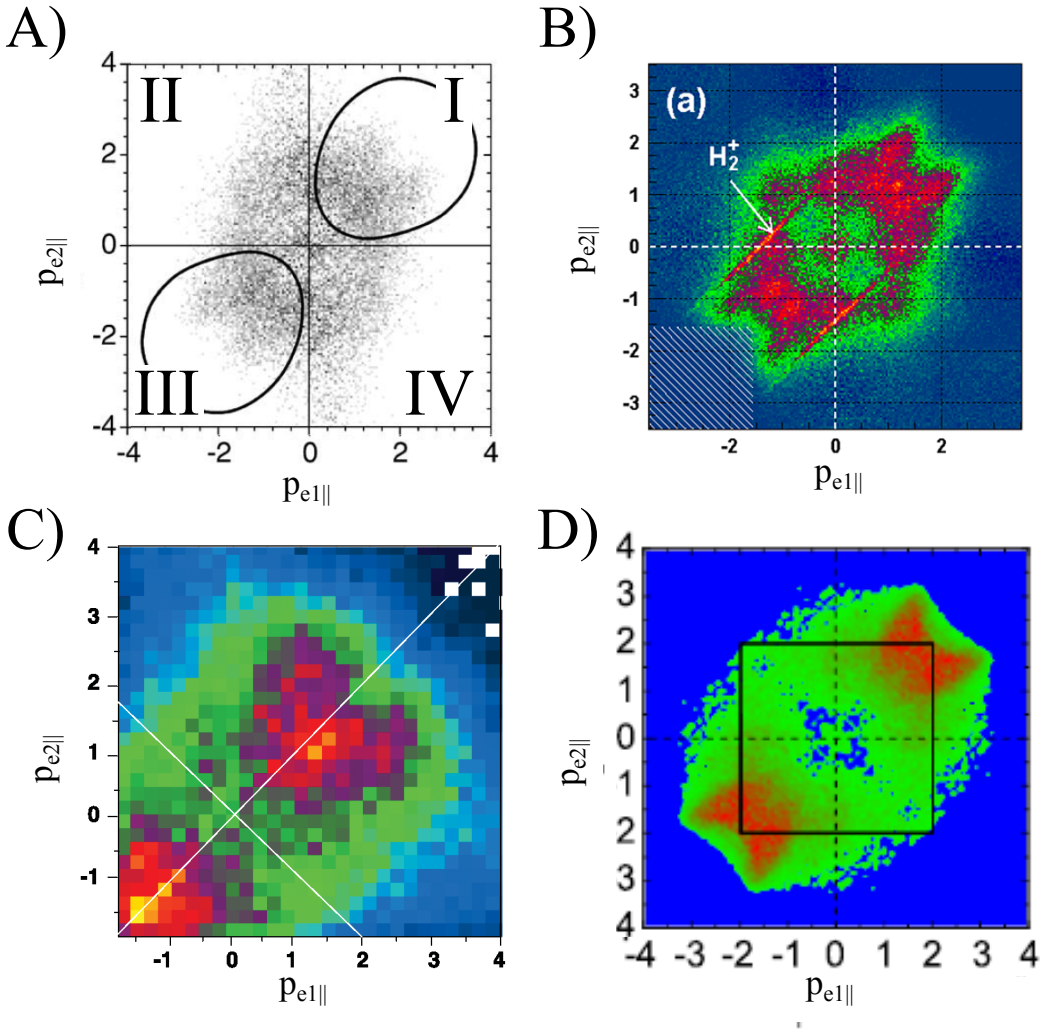

Figure 1.14: A) Correlation plot for the ionization of helium by 800 nm, $0.5 \cdot 10^{15}$ W/cm^2 laser pulses, taken from [dJRF$^+$04]. B) Similar conditions than A) with more statistics, from [SRS$^+$07], note the false line coincidence coming from ionization of H_2. C) Correlation plot for the ionization of helium by a 800 nm, $1.5 \cdot 10^{15}$ W/cm^2 laser, from [RdJE$^+$07]. D) Correlation plot from a semi-classical model for the ionization of helium at $0.45 \cdot 10^{15}$ W/cm^2, taken from [YLL08].

the maximum of the envelope and the maximum of the electric field. In figure 1.15 two pulses with a 6 fs duration are shown for two different CEPs. The definition of the CEP is visually expressed, in figure A), by the delay between the black and red markers.

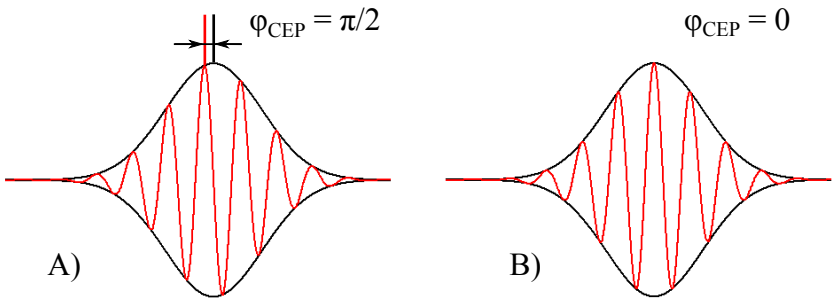

Figure 1.15: Short laser pulses for two different CEP A) $\varphi_{CEP} = \pi/2$ B) $\varphi_{CEP} = 0$

In the case of ultra-short laser pulses the common mathematical expression used to describe them is:

$$E(t) = \epsilon(t)\cos(\omega t + \varphi_{CEP}) \quad , \tag{1.16}$$

where $\epsilon(t)$ accounts for the envelope of the pulses. It is generally a Gaussian or a $\cos^2$ function[4].

Two major advantages can be seen from the use of CEP characterized ultra-short laser pulses. The first one is the reduction of the interaction time between the laser and the target. The second advantage is the possibility to control the characteristics (emission direction and energy) of the photo-electrons with the CEP. This second aspect is considered in the following part.

The main underlying objective behind the reduction of the interaction time is to reduce the effect of multiple recollisions. As discussed in section 1.2.2, semi-classical models looking at electron trajectories leading to NSDI, unravel the role of multiple recollision mechanism for a large number of events. Experimentally, possible multiple returns of the electron were addressed in [LTR$^+$08, LYL$^+$10] by utilizing laser intensities too low for direct impact ionization accessing the so-called "below threshold regime". Although this does not suppress the RESI mechanism happening within a single optical cycle, the correlation plot was interpreted as originating from multiple recollisions.

Nonetheless for a pattern in the correlation plot such as the finger-like structure,the analysis of the trajectories showed that a single recollision was present for these [YCL08, YL10]. Additionally, the theoretical treatment of NSDI of helium using ultra-short laser pulses also revealed the presence of this structure [PBSEZ08, XYL10] indicating that the interaction between the electron and the helium ion is not modified by a decrease of the interaction time.

1.3.1 Carrier-envelope phase effects

Two possible effects of the CEP on the photo-electron characteristics can be distinguished. The first one is the photo-electron emission direction. It is defined by the sign of the vector potential at the moment of ionization (cf. 1.2.2). Because the number of half-cycles is limited in ultra-short laser pulses, the CEP influences the contribution from each and the amount of ionizing event with a downward or upward emission direction. Moreover, due to the electron recollision trajectory specific to each half-cycle, the energy acquired by the photo-electron varies with the CEP. These effects have been observed and calculated in the case of single ionization (cf part 2.3). In this section, we consider these effects for the double ionization case.

[4]the function $\cos^2$(x) is normally periodical but in that case, the envelope is put to zero for $|x| > \pi/2$.

Emission direction

In comparison to the treatment made in the single ionization case, in order to define the probability for an electron to be emitted downwards or upwards an asymmetry parameter can be defined:

$$A = \frac{N_{\text{up}} - N_{\text{down}}}{N_{\text{up}} + N_{\text{down}}} \quad , \tag{1.17}$$

where N_{up} is the number of electrons emitted upwards and N_{down} is the number of electrons emitted downwards. For single ionization, it was found that the larger this parameter, the shorter the pulse duration[SRM+11a], as expected from an intuitive picture: the shorter the laser pulse is, the smaller the number of cycles participating in the ionization process and the more the influence of the CEP on the asymmetry. In the case of double ionization, two electrons are emitted and are experimentally indistinguishable. The asymmetry is taken for the ion (which momentum is the opposite of the sum of the two electrons). An asymmetry dependence on the CEP was predicted theoretically ([LFdMF04]) and measured experimentally in the longitudinal momentum of the ion for the ionization of argon [LRE+04]. Figure 1.16 displays the dependence of the asymmetry with the CEP. When changing the CEP, the distribution varies from events localized at negative momentum (on the left, $p_{||} < 0$) in A) to a distribution localized at positive momentum in E). The intermediate step is given for $\varphi_{\text{CEP}} = \varphi_0$ where the distribution is the most symmetric. For a better comparison the distribution obtained when no stabilization of the CEP is applied is shown in panel F). The asymmetry between the left and the right peak shows that through the selection of the CEP, the emission direction of the electrons is influenced by it and can be controlled.

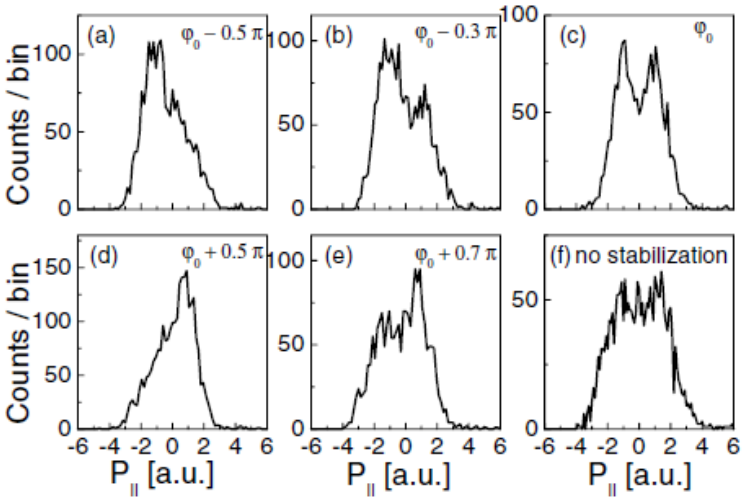

Figure 1.16: Longitudinal momentum of the ion as function of the CEP. A-E) Distribution at different CEP. φ_0 is the CEP where the distribution is the most symmetric. F) Distribution where the CEP is not fixed to a given value. Pictures taken from [LRE+04].

The information which can be extracted from the change in ion longitudinal momentum with the CEP is however limited. One has to consider in addition the influence of the CPE on the energy of the recolliding photo-electron.

Energy of the recolliding photo-electron

The energy of the recolliding electron depends on the propagation trajectory in the laser field and more specifically on the difference between the vector potential value at the time of ionization and the time of recollision (cf equation 1.15). For a monochromatic laser (infinite pulse duration) no difference is made between different half-cycles. When using ultra-short laser pulses, the recollision trajectory is altered from one cycle to the other due to the specific shape of the electric field. The

returning energy depends on the ionization time and on the half-cycle during which the electron is ionized. This introduces a dependence on the shape of the electric field, on the CEP. Figure 1.17 A) shows the calculated energy of the recolliding electron for different CEPs. As a green doted line, the electron-impact inelastic cross section is plotted (similarly to that in figure 1.8), being the sum of the cross section of the ionization and of the excitation from the ground state of Ar^+. Following the fact that the impact energy of the recolliding electron depends on the CEP, the probability for inelastic recollision has also a dependence on the CEP. The first visible observable is the change in yield of NSDI. In figure 1.8 B), this double ionization yield for the theoretical results is shown, for different intensities (colored curve) together with an experimental investigation (black points) [JHW+11]. A clear dependence on the CEP can be observed. The π-periodicity of the curve is due to the amplitude of the field having a periodicity of π. Two pulses having CEP of ϕ and $\phi+\pi$ have the same electric field but with opposite sign and therefore same electron recolliding energy.

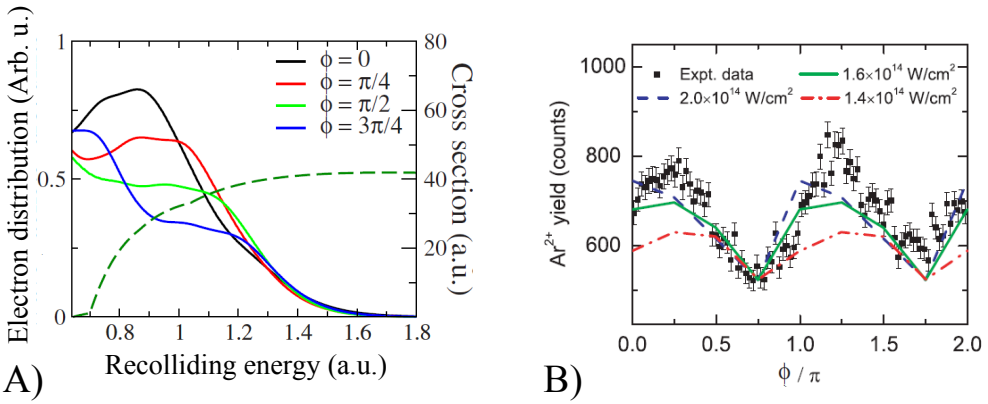

Figure 1.17: A) The solid curves represent the energy of the recolliding electronic wave packet for different phases (here ϕ) of the laser. The laser pulse has a duration of five cycles and an intensity of $2.0 \cdot 10^{14}\,\mathrm{W/cm^2}$. The green doted line corresponds to the electron-impact inelastic cross-section (addition of the direct ionization and the excitation cross-section). Picture taken from [MCLL09] B) NSDI yield for experiment (black dots) and theory (colored curves) as a function of the CEP, taken from [JHW+11] using theoretical calculations of [MCLL09].

One step further is to distinguish the contribution leading to RESI and the one leading to (e,2e)-like ionization in the NSDI process as a function of the CEP. This is represented for NSDI of helium at different intensities in figure 1.18. A selection of the process has been made together with a variation of the CEP. In comparison with the total yield curves, a clear dependence of the CEP is present. More interestingly, this CEP dependence varies with the process considered. For instance, for the higher intensity (green curve), the minimum for the RESI process is located at $0.4\,\pi$ and for the (e,2e)-like process at $0.6\,\pi$. This features is important. It shows that by investigating the modulation as a function of the CEP of a given features (for example the quadrants II in the correlation plot) one can reveal whether it originates from the RESI or (e,2e)-like mechanism. The CEP introduces an additional parameter to possibly distinguished different process. Nonetheless an exact identification of the processes from the experiment seems difficult since the maxima and minima of the yields also vary with the intensity. Experimentally, isolating one, precisely defined intensity is not possible and leads to smoothing of the features over the intensities.

The investigation of NSDI with ultra-short and CEP-characterized laser pulses allows the temporal confinement of the recollision process and provides a new tool to distinguish the possible mechanisms. Experimentally, only ion distributions have been investigated, but electron correlation are expected to reveal more insights. Presently, theoretically studies integrating all processes have been performed [CLML11, XYL10] leading to the observation of the finger-like structures. In this case, the strongest CEP effect is the change in emission direction of the ion. In the next

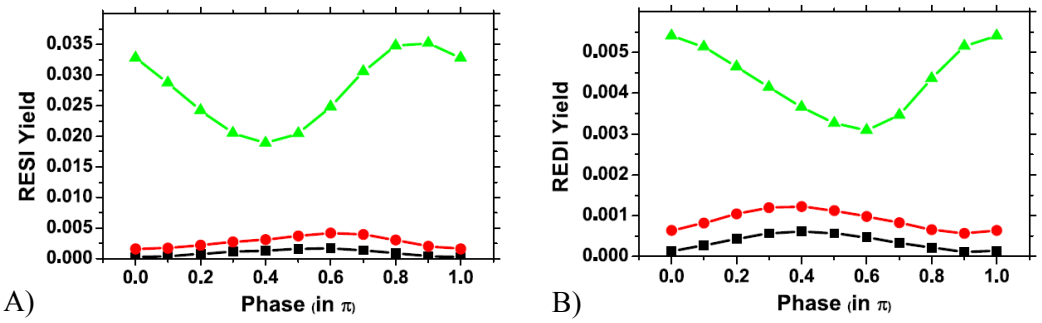

Figure 1.18: Different yields for the NSDI of helium. A) Yield of the RESI process as a function of the CEP. B) Yield of the (e,2e)-like process (called REDI) as a function of the CEP. Different intensities are used: black curve, $2.2 \cdot 10^{15}$W/cm^2 ; red, $3.1 \cdot 10^{15}$W/cm^2 ; green, $5.6 \cdot 10^{15}$W/cm^2. Graphs taken from [EPBSZ10].

part a different technique of modulating the laser electric field is presented: the superposition of the fundamental field and its second harmonic.

1.3.2 Studies with two-color pulses

Description of the two-color pulses

The control of the electron trajectories through the control of the electric field has been demonstrated by using CEP characterized ultra-short laser pulses. A different approach to control the electric field shape is to create and superimpose the second harmonic component to the laser pulses (referred as fundamental). Varying the phase between the two colors introduces a modulation on the form of the electric field. Two configurations are possible and were mainly treated: the two color pulses are linearly polarized and their polarization direction is parallel or orthogonal. The latter case implies that the two colors are in principle independent. Each color modifies the electron trajectory in its polarization direction. The harmonic laser can be seen as a "non-destructive" probe to the recollision mechanism induced by the fundamental simply adding timing constraints on the recollision [SSB$^+$12].

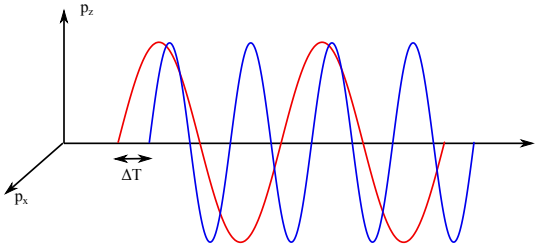

Figure 1.19: Representation of the two-color scheme. The fundamental (wavelength of 800 nm, red curve) and its frequency doubled component (wavelength of 400 nm, blue curve) are superimposed. For a precise control of the electric field a control of the delay ΔT between the blue ad the red is needed. Note: here only a minor part of the multi-cycle pulses is shown.

We focus on the configuration with the two polarizations parallel, where each color influences the same momentum component. Figure 1.19 shows a sketch of the two laser waves. In order to control the electronic trajectories, the phase or delay ΔT between the two pulses has to be controlled and varied. the mathematical expression for the two-color beam is:

$$\begin{aligned} E_{\text{2-color}}(t) &= E_{\text{fund}}(t) + E_{\text{harm}}(t) \\ &= \epsilon_{\text{fund}}(t)\cos(\omega t) + \epsilon_{\text{harm}}(t)\cos(2\omega t + \varphi_{\text{blue}}) \end{aligned} \tag{1.18}$$

the functions $\epsilon(t)$ represent the envelope of each pulse. We consider that they have the same shape (same pulse duration) but that the amplitude of the harmonic component is half of the amplitude of the fundamental pulse.

The corresponding electric field is shown in figure 1.20 in red for four values of φ_{blue}. In green is represented the vector potential of the electric field ($E(t) = -\frac{dA(t)}{dt}$).

The two fields have to be considered for the ionization process. The probability of ionization (equation 1.5) has a dependence on the amplitude of the electric field. It varies therefore with the phase of the blue. It is maximum for $\varphi_{\text{blue}} = 0$ and $\varphi_{\text{blue}} = \pi$ and minimum for $\varphi_{\text{blue}} = -\pi/2$ and $\varphi_{\text{blue}} = \pi/2$. For instance, having a red field at an intensity of $3.0 \cdot 10^{14}\,\text{W/cm}^2$, the ratio between the minimum and maximum probability for ionization of an argon atom integrated over a laser period is 0.70.

The asymmetry introduced in the shape of the vector potential field has also to be taken into account. In the common approximation, the final momentum of the photo-electron is equal to the opposite of the vector potential value at the moment of ionization. For a phase such as $\varphi_{\text{blue}} = -\pi/2$, the vector potential curve extends up to 0.75 Arb. u. on the positive and to 1.5 Arb. u. on the negative side introducing an asymmetry in the maximum value the photo-electron can gain. When considering more than a single phase it can be seen that this asymmetry and the maximum evolves. For instance, for $\varphi_{\text{blue}} = 0$ the maximum value is 1.3 Arb. u. but it is the same on both side.

Considering the two fields shows that the predictions on the photo-electron emission direction are not intuitive to estimate as developed in [RCD+11, BC00, CZB01]. Nonetheless an application on the control of the electron trajectory can be considered.

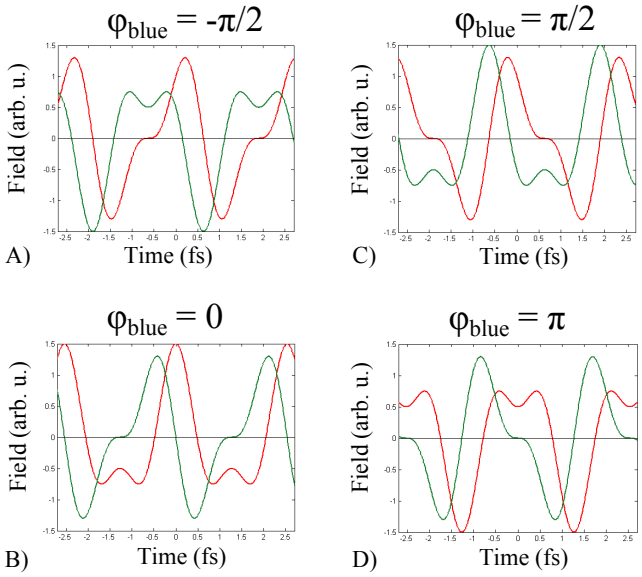

Figure 1.20: A-D) Representation of the electric field (red) and the vector potential (green) for different phase of the blue. The fields are monochromatic and the ratio between the blue and the red electric field amplitude is 0.5.

Energy of the recolliding photo-electron

Because of the asymmetric electric and vector potential fields, the energy of the recolliding electron is strongly influenced by the phase of the blue. Figure 1.21 shows the maximum return energy of the electron as a function of the delay between the two pulses for the case where the ratio is 0.5 between the blue and red amplitude. Similarly to figure 1.11, the simplest approximations are used for finding the recolliding time and the energy of the recolliding electron. The energy is expressed in terms of ponderomotive energy U_p defined for the red field without blue component. A distinction is made between the trajectories where the electron is moving upwards (blue curve) or downwards (red curve) in the field. This two curves are the same by a phase shift of π. This reflects the fact that the shape of fields for a given phase transform into the opposite shape (change of sign and so of emission direction) with a π shift.

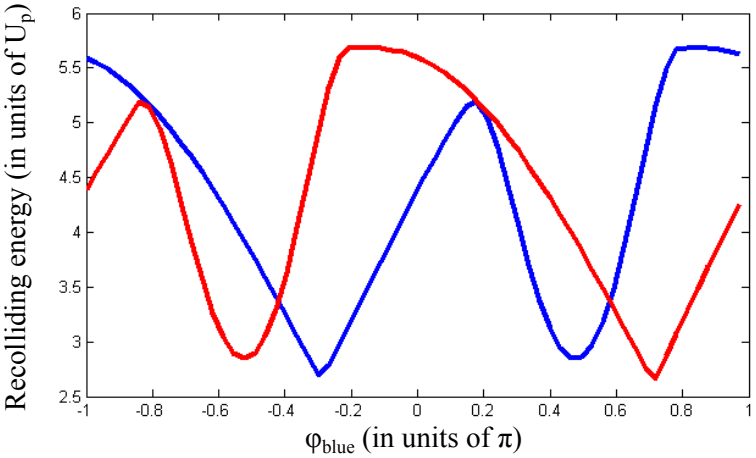

Figure 1.21: Maximum of the recolliding energy of the electron depending on the phase of the blue field. A distinction is made between the red curve which represents the downwards trajectories and blue curve for the upwards trajectories.

Of interest is the large variation of the energy from 2.6 to 5.7 U_p. Taking for instance a red field of intensity $2.0 \cdot 10^{14}\,\mathrm{W/cm^2}$ yields $U_p = 0.42$ a.u.$= 11.5\,\mathrm{eV}$. The highest impact energy ($5.7\,U_p = 65.6\,\mathrm{eV}$) allows the direct impact ionization of helium ions ($\mathrm{I}_p = 24.6\,\mathrm{eV}$) but not the lowest value. This opens perspectives to differentiate between (e,2e)-like process and RESI in NSDI with the phase of the blue field.

In the case of HATI electrons (rescattering electrons which do not ionize the ion), the emission direction and energy dependence on the phase of the blue have been theoretically and experimentally investigated and shown [RCD$^+$11, Che11]. However, up to the present knowledge, no study has yet been reported looking at the dependence of the rescattering electron applied to NSDI when the two polarizations are parallel and the wavelengths are 800 and 400 [5].

Summary

The recollision mechanism is an important process contributing to ionization of atoms and molecules in strong laser field. It has wide applications from the realization of attosecond pulses to the observation of the non-sequential double ionization. NSDI is a prime candidate for studying electron correlation in atomic systems. Comparison between observed and predicted features - even for the most commented ones - shows the difficulties of interpreting mechanisms. Experimentally, progresses can be made by applying the latest electric field control to study the mechanism (in

[5] the closest known studies of NSDI in two-color experiments concern orthogonal polarizations [ZHT$^+$11, TDF12] or parallel field with wavelengths of 1600 and 800 nm [ZLZ$^+$10, ZQC$^+$10].

combination with measurement of the two electrons momentum). Primarily, the utilization of ultra-short laser pulses allows on the one hand to confine the process temporally and on the other hand, when the phase of the laser is characterized, to observe sub-cycle dynamics of the electrons. This control enables a discrimination between the different mechanisms involved. A control of the electric field shape and therefore on the recollision trajectories can be also realized by applying a two-color scheme to the ionization of atoms.

Chapter 2

Generation and characterization of short laser pulses

Experimental studies on photo-ionization of atoms and molecules with visible light have been considerably improved by the development of intense laser source. Alongside, the temporal confinement of the observed phenomena has required to constantly decrease the pulse duration. Today it is possible to produce laser pulses that last only a few optical cycles. The nowadays prime candidate for such sources is the amplified Titanium:Sapphire (Ti:Sa) laser, commercially available and delivering few millijoules over a duration of few tens of femtoseconds. Although the intensity reached is sufficient for observing the recollision process, the raw pulses do not allow, because they are too long, to observe any influence of the electric field shape on the ionization dynamics. Additional experimental implementations are needed to shorten these pulses in duration or to sculpt the electric field. In the first section of this chapter, the generation of the so-called ultra-short laser pulses from our Ti:Sa system is presented. Afterwards, the characterization of such pulses with emphasis on the use of the stereo-ATI spectrometer is discussed. The last part addresses the experimental realization of modeled laser pulses by the use of a two-color Mach-Zehnder interferometer.

2.1 Pulse generation

2.1.1 Definition and properties of short pulses

The most straightforward representation of ultra-short laser pulses is probably to consider the laser as a coherent superposition of a large number of spectral components interfering to form its temporal profile (for an unchirped pulse, its carrier wave is the central frequency of the spectral distribution). At a fixed point in space the time dependent electric field reads the following:

$$E(t) = \Re\left[\int A(\omega)\cdot\exp\left[i(\omega t-\varphi(\omega))\right]d\omega\right], \tag{2.1}$$

where A(ω)is the spectral amplitude of the frequency ω and $\varphi(\omega)$ the corresponding phase. The time duration of the laser pulse τ is linked to the spectral bandwidth $\Delta\omega$ through the bandwidth theorem:

$$\Delta\omega\cdot\tau \geq 2\pi c_B. \tag{2.2}$$

In the case of a beam with a Gaussian temporal profile $c_B = 0.441$ [DR06]. When the equation fulfill the equality, the pulse is "Fourier-limited": it is the shortest possible pulse given the available spectral bandwidth. The function $\varphi(\omega)$ is linear with ω.

Pulse compression

When a laser pulse propagates through a material, each frequency propagates with a different phase velocity $v_\varphi(\omega) = \frac{c}{n(\omega)}$ with $n(\omega)$ the refractive index of the material at the frequency ω. The propagation through a material affects the phase of each frequency. The field after a distance z can be expressed as :

$$E(t,z) = \Re\left[\int A(z,\omega)\cdot\exp\left[i(\omega t - \varphi(z,\omega))\right]d\omega\right] \tag{2.3}$$

The amplitude $A(z,\omega)$ equals $A(\omega)$ if there is no reflection or absorption by the media. The properties of each material define $\varphi(z,\omega)$ and so the change of temporal profile of a given laser pulse. The phase can be decomposed as a Taylor expansion around the central frequency ω_0:

$$\begin{aligned}\varphi(z,\omega) &= \varphi(\omega_0) + (\omega-\omega_0)\frac{\partial\varphi}{\partial\omega}\Big|_{\omega_0} + \frac{1}{2}(\omega-\omega_0)^2\frac{\partial^2\varphi}{\partial\omega^2}\Big|_{\omega_0} + ... \\ &= \varphi(\omega_0) + (\omega-\omega_0)GD + \frac{1}{2}(\omega-\omega_0)^2 GDD + ...\end{aligned} \tag{2.4}$$

where $\varphi(\omega_0)$ is a constant phase offset for all frequencies, GD is defined as the group delay and GDD the group delay dispersion. The group delay is related to the group velocity of the pulse: $GD = \frac{z}{v_{gr}}$, where

$$v_{gr}(\omega) = \frac{c}{n + \omega\frac{\partial n(\omega)}{\partial\omega}}.$$

v_{gr} is the velocity of the envelope of the pulse. If it is different from the phase velocity of the carrier $v_\varphi(\omega_0) = \frac{c}{n(\omega_0)}$, the envelope is delayed with respect to the carrier signal. The first order dispersion only affects the Carrier-Envelope Phase (CEP) of the pulse. The second and following dispersion orders change the temporal profile and duration of the pulse. A pulse is at its Fourier limit when these higher dispersion orders are equal to zero. All "natural materials" (air, glasses) introduce positive dispersion meaning that the red frequency is propagating faster than the blue components leading to an extension of the pulses duration and so called "chirped pulses". For example, two meters of propagation in air transform a Fourier limited 6 fs pulse into a 24.5 fs pulse while a 25 fs pulse is elongated to 32 fs. To compensate these effects one can introduce negative dispersion with prisms or chirped mirrors.

Self-phase modulation

Dispersion is affecting the temporal profile of the pulse but not its spectrum. To broaden the pulse spectrum and shorten its duration one can make use of the self-phase modulation (SPM). This effect appears due to the optical Kerr effect: a dependence of the refractive index on the intensity of the laser field.

Assuming a Gaussian temporal profile, the intensity of the laser pulse is:

$$I(t) = I_0 exp(-\frac{t^2}{\tau^2}) \tag{2.5}$$

with I_0 the maximum intensity. For a given frequency ω_α, the time varying refractive index can be expressed through the equation:

$$n(t,\omega_\alpha) = n_0(\omega_\alpha) + n_2(\omega_\alpha) I_0 exp(-\frac{t^2}{\tau^2}). \tag{2.6}$$

This leads to a time varying phase of the pulse after propagation over a distance L of the medium

$$\varphi(\omega_\alpha, t) = \omega_\alpha t + \frac{2\pi}{\lambda_\alpha} n(t,\omega_\alpha) L \tag{2.7}$$

The instantaneous frequency shift is therefore:

$$\omega_\alpha(t) = \frac{d\varphi(t)}{dt}\Big|_{\omega_\alpha} = \omega_\alpha + A \cdot t \tag{2.8}$$

with

$$A = \frac{d\omega_\alpha}{dt} = \frac{4\pi L n_2 I_0}{\lambda_\alpha \tau^2} < 0 \tag{2.9}$$

This effect adds up to dispersion and leads to frequency broadening. The lowest frequencies, which are the fastest and so are present at the beginning of the pulse (T>0), are shifted towards even lower frequencies. On the contrary, the highest frequencies, present at the end of the pulse, are shifted towards even higher frequencies. The spectrum is broadened.

This dependency of the refractive index on the intensity induces change on the temporal profile of the pulse but also on its spatial profile. This effects is at the origin of the Kerr-lens mode locking (KLM) [SKS91]. When focusing the beam, regions of different intensities will focus at a different positions. This is used to selectively amplify given cavity modes by spatially controlling the overlap between the pump and the laser beam.

In the following, the practical generation of few-cycle laser pulses from a commercial system is presented. The delivered 25 fs pulses are compressed using a hollow core fiber and chirped mirrors.

2.1.2 The laser system

The first part is a commercial laser. It is depicted in figure 2.1. The three main elements of this system are the oscillator, the amplifier and the compressor.

Oscillator

The femtosecond laser pulses are produced by pumping a Titanium:Sapphire (Ti:Sa) crystal with a continuous 532 nm laser beam. This green beam is produced by a commercial Nd:YVO system delivering 3 Watts continuous light. Due to KLM inside the Ti:Sa crystal, the cavity modes can be locked such that they form ultra-short laser pulses. The spectrum after the oscillator cavity is shown in figure 2.2. The bandwidth is 250 nm with a central wavelength of 780 nm. The repetition rate of the laser is 80 MHz with a pulse energy in the order of the nanojoule. The pulses are Fourier-limited and have a duration of less than 10 fs. One possibility of this commercial oscillator is to measure and stabilize the Carrier-Envelope Phase (CEP) of the output pulses. Nonetheless, this control needs some additional feedbacks, independent of the laser system, due to long term (few hours) drift of the CEP (see [Fis10]). Moreover, for this version of the commercial laser, the control often goes out of locking requiring to restart manually the feedback control. These disadvantages, in comparison with the phase tagging technique (see section 2.3) imply that this function was never used for the work presented in this thesis.

Amplifier and compressor

Although the pulse duration after the oscillator is satisfactory, the energy of each pulse is too low to observe ionization. The output beam of the oscillator is therefore amplified by a factor of one million by chirped pulse amplification [SM85, PM94]. The laser beam propagates first through a stretcher in order to elongate the time duration and to reduce the peak energy of the pulses. The stretched pulses pass nine times through the gain medium, a Ti:Sa crystal pumped by 300 ns laser pulses at a wavelength of 527 nm with an energy of 10 mJ (at the beginning of my doctoral work the pump laser was a Nd:Yag laser having very similar characteristics but a wavelength of 532 nm). After the fourth pass through the crystal, the repetition rate is reduced from 80 MHz to 3 kHz using a Pockel cell and associated wave plates.

The output is sent to a compressor to reduce the pulse duration. Chirped mirrors and prisms compensate second and third orders dispersion to reach a final pulse duration of 25 fs. The pulse energy is 1.0 mJ. At this point the pulses are Fourier limited and the spectral bandwidth has been

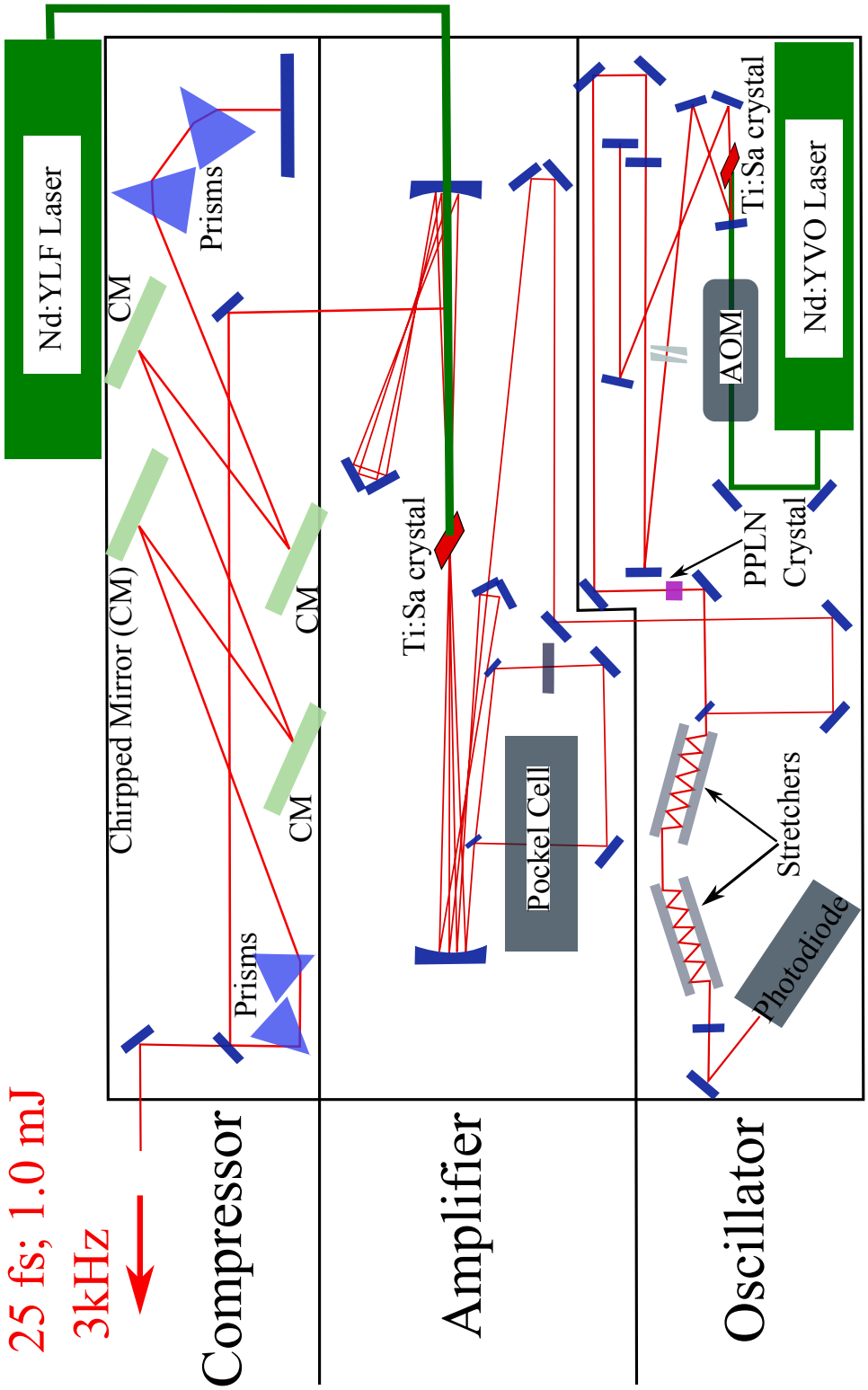

Figure 2.1: Schematic drawing of the laser setup, see text for description.

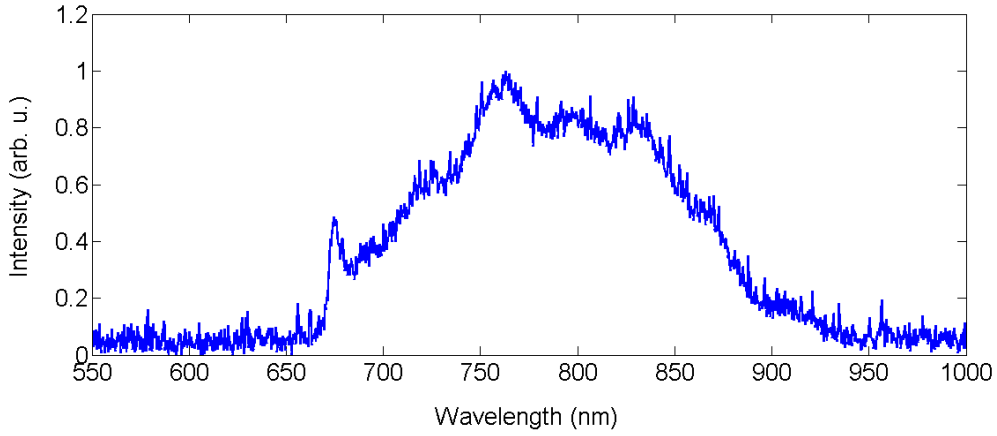

Figure 2.2: Spectrum after the oscillator.

reduced by the amplification process (see figure 2.4) such that the pulses are 25 fs long. It is therefore needed to broaden the spectral bandwidth to be able to obtain few-cycle laser pulses as described below.

2.1.3 Spectral broadening

The spectral broadening of the laser pulses is made using SPM (cf. section 2.1.1). The beam is focused inside a one meter long hollow-core fiber filled with 3 bars of neon gas (figure 2.3). The diameter of the fiber is 250 μm leading to the selection of the zeroth mode of the Gaussian beam. The dispersion of the pulses therefore depends on the propagation of the laser pulses in the gas and the dispersion introduced by SPM. The phase is usually assumed to be flat at the output of the fiber leading to Fourier-limited pulses. As seen in figure 2.4 the spectral width is extended from 40 to 250 nm supporting a pulse duration of 3.8 fs. The central frequency, being the averaged frequency, is also shifted from 780 to 740 nm. Nonetheless, due to optical elements along the beam path filtering out high frequencies (UV, blue and green), the final spectrum in our main experimental chamber is not as broad leading to an estimated pulse duration of 6 fs.

After the spectral broadening, the pulses pass through a compressor stage made of chirped mirrors. They introduce negative dispersion such that the blue components are first in time, in order to pre-compensate for all the dispersive elements present in the beam path until the main reaction chamber, in which the red frequencies propagate faster than the blue ones. Although the introduced dispersion can be calculated, imprecisions of optical elements (thickness of glass, length propagation in air) forbid relying exclusively on theoretical predictions. In order to assure the shortest pulse possible in the main experiment chamber, different analysis tools can be used as explained in the next section.

2.2 Pulse characterization

No detectors or electronics can record directly the ultrafast change of the envelope of the pulses or the even faster change of the carrier wave. Different methods exist to characterize pulse durations.

The basic principles of two relevant techniques are introduced. In the first part the autocorrelation technique based on interferences between the pulse and a delayed copy of it is presented. In the second part an optical technique will be discussed, the f-2f, based on the characterization of the spectral phase in order to reconstruct the electric field of the pulse.

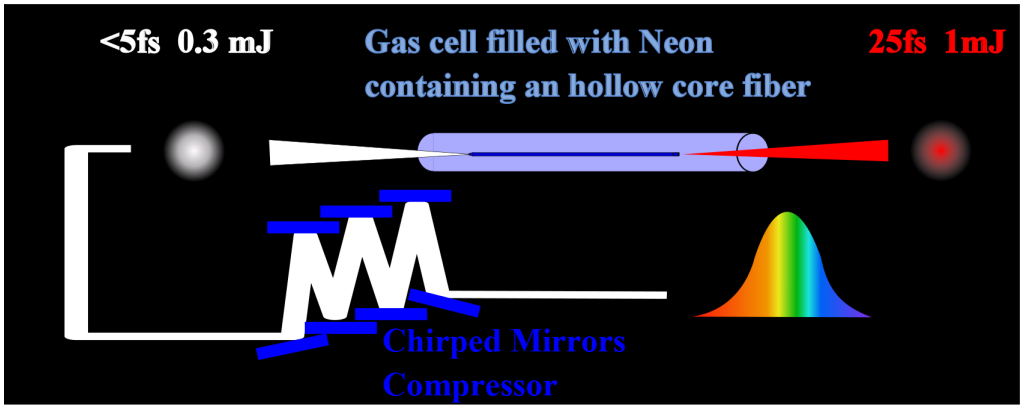

Figure 2.3: Schematic drawing of the fiber compressor. The 25 fs laser pulses are focused inside a hollow core fiber filled with neon where the process of SPM enlarges the spectral bandwidth. In order to compensate for dispersive elements present in the beam path, the laser is sent through a chirped mirror compressor where the red frequencies are delayed relatively to the blue/green components.

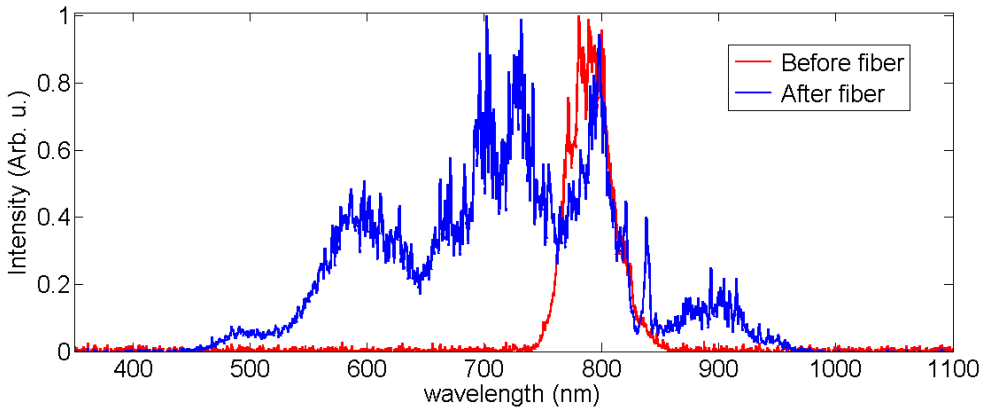

Figure 2.4: Effect of SPM: Comparison of spectra before and after the fiber.

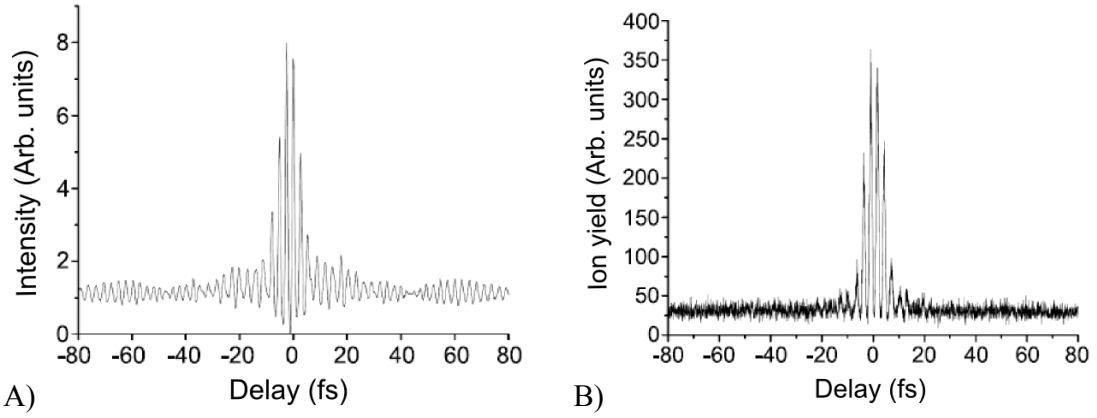

Figure 2.5: Autocorrelation signals obtained from measurement of the second harmonic field (n=2) A) and ionization of argon (n>10) B). Taken from [Kre09].

2.2.1 Autocorrelation

The principle of autocorrelation is to probe the electric field E(t) of a laser pulse with a copy of itself. By looking at the intensity of the interfering two laser pulses as a function of the delay between them one can reconstruct the temporal shape of the pulse. Mathematically the autocorrelation signal reads:

$$I(\tau) = \int_{-\infty}^{+\infty} \left[\left(E(t-\tau) + E(t) \right)^2 \right]^n dt, \tag{2.10}$$

"n" is the order of the autocorrelation. In the most common case, where the autocorrelation signal is issued from second harmonic generation, n=2. An example is given in figure 2.5 A) for 6 fs laser pulses. The autocorrelation trace can also be retrieved from the ionization of atoms as shown in figure 2.5 A) for single ionization of argon (n>10). Chirp is a major problem to reconstruct a pulse from the autocorrelation trace. If a pulse is Fourier-limited, assuming a given temporal profile (e.g. Gaussian), it can be reconstructed from the autocorrelation trace. However, this reconstruction and extracting a unique value of the dispersion involved is not always possible for a given trace. The autocorrelation technique gives an indication about the pulses length, but finding the right amount of dispersion to compensate the chirp is not straightforward.

2.2.2 F-2f method

In order to determine the temporal profile of the pulses, few techniques have been developed based on the characterization of the spectral phase of the pulses. Techniques such as spectral phase interferometry for direct electric-field reconstruction (SPIDER) [IW98] or frequency-resolved optical gating, (FROG) [KT93] are the most common. They are based on the characterization of the complete phase relation of the spectrum and the reconstruction of the temporal profile. The same principle is used in the f-2f technique but only the phase relation between the blue and red frequencies is measured and a linear relation is assumed for all spectral phases (which is true close to Fourier limited configuration).

The first experimental realization of the f-2f technique was proposed in [KTK$^+$01]. To measure the phase between two frequencies, we have to observe interferences between them. The red component is therefore doubled (leading to blue frequencies). Assuming the definition (2.1), the electric field for each frequency is:

$$f(\omega_\alpha, t) = \Re \left[A(\omega_\alpha, t) \cdot \exp \left[i(\omega_\alpha t - \varphi(\omega_\alpha)) \right] \right]. \tag{2.11}$$

Passing the red frequencies through a frequency doubling crystal creates a component having twice the original frequency $2\omega_\alpha$. This component is added to the original signal:

$$\begin{aligned} result(t) &= g(2\omega_\alpha, t) + \tilde{f}(\omega_\alpha, t) \\ &= \Re\left[B(2\omega_\alpha, t) \cdot \exp\left[i(2\omega_\alpha t - \varphi(2\omega_\alpha))\right]\right] + \tilde{f}(\omega_\alpha, t) \end{aligned} \tag{2.12}$$

$\tilde{f}(\omega_\alpha, t)$ is the original component modified in phase and amplitude by the frequency doubling process. It does not interfere with blue frequencies and is therefore unimportant in the following. Intrinsically to the frequency doubling process, we obtain $\varphi(2\omega_\alpha) = 2 \cdot \varphi(\omega_\alpha)$. The new created component $2\omega_\alpha$ can interfere with the frequency $\omega_\beta = 2\omega_\alpha$ originally present in the laser pulses. This leads to interferences in the frequency domain and the possibility to measure the phase difference $\Delta\varphi$ between the two frequency component ω_α and ω_β.

$$\Delta\varphi = \varphi(2\omega_\alpha) - \varphi(\omega_\beta) = 2\varphi(\omega_\alpha) - \varphi(\omega_\beta) \tag{2.13}$$

Considering ω_α being the carrier frequency, $\varphi(\omega_\alpha) = \varphi_{CEP}$ and using equation 2.4:

$$\varphi(\omega_\beta) = \varphi_{CEP} + \frac{1}{2}(\omega_\beta - \omega_\alpha)^2 GDD + ...$$

By measuring the interference fringes with a spectrometer, the phase relation can be measured. The fringes spacing in frequency gives information on the higher order term of dispersion and therefore on the pulses length (equivalently on the time delay between the blue and the red).

An other information that one can extract from the fringe-pattern is the φ_{CEP} of the pulse. Practically only the variation in φ_{CEP} is determined. The determination of the absolute value φ_{CEP} is related to the determination of the central frequency in the interference pattern which is not accessed precisely. A long term control of φ_{CEP} is possible by combining this technique with CEP stabilization of the laser inside the oscillator of the amplifier system [Kre09, Fis10]. Somehow, the limitations of this characterization technique are linked to the phase stabilization of the laser. Although some f-2f measurements have been demonstrated on a shot-to-shot basis [KTK$^+$01], in the present case, integration of the interference measurements over few pulses is required and therefore we need to stabilize the CEP of the laser. As mentioned in section (2.1.2), the phase stabilization for our laser setup is not very convenient obliging to often reset the feedback control during a measurement. Experimentally, the solution utilizing the stereo-ATI spectrometer for phase tagging (section 2.3) is more adequate. Another disadvantage of controlling the phase using the f-2f technique concerns the control of the CEP. From the oscillator, the CEP is fixed at one value. Changes of φ_{CEP} are possible by adjusting the amount of dispersion, by moving a glass-wedge by few μm inside the beam path. Nonetheless, the dispersion introduced for the control is limited by the used material. At the same time second and third order dispersion is introduced leading to non-linear phase shifts [KHF$^+$11]. A better approach than stabilization and feedback control of the phase is done through phase tagging: the measurement of the CEP of each pulse. The set-up for this tagging is the stereo-ATI spectrometer[1] described in the next section.

2.3 CE-phase determination

The phase determination is relying on an asymmetry in the process of atomic ionization. In a first part, we will see how one can rely on atomic ionization to characterize the pulse and the experimental set-up implemented to realize it. In a second part, we will see how the signal can be extracted to produce the so-called phase ellipses and extract the φ_{CEP} for each pulse. And finally, it is described how this technique can allow a precise and long term characterization of the laser.

[1] ATI stands for Above-Threshold Ionization

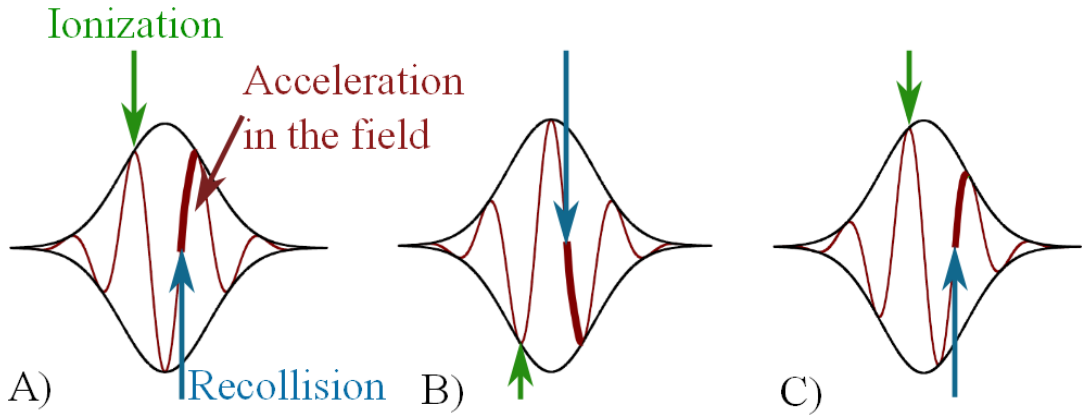

Figure 2.6: Effect of the CEP on the motion of the photo-electron in the laser field. Three pulses with different values of the CEP are represented. A) $\varphi_{CEP} = -\pi$, B) $\varphi_{CEP} = 0$, C) $\varphi_{CEP} = -\pi/2$. In each case, the instant of ionization (green arrow), the time of recollision (blue arrow) and the acceleration period of the electron over the electric field (part where the pulse is bold is shown).

2.3.1 The stereo-ATI spectrometer

The stereo-ATI technique is based on the analysis of High Above-Threshold Ionization (HATI) electrons from xenons atoms. These electrons are ionized and driven by the laser field until recollision and back-scattering on the ionic core. Their production is schematically shown in figure 2.6 where the temporal profile of an ultra-short laser pulse for three different φ_{CEP} is shown. Through classical considerations, we can estimate how the shape of the electric field affects the emitted photoelectrons. In all cases, an electron is ionized close to the maximum of a laser pulse and is driven by the electric field of the laser until it recollides close to a zero-crossing of the electric field. Considering the electrons being elastically backscattered from the ion, they are further accelerated by the laser field. Their direction of emission strongly depends on the ionization time and the sign of the electric field at this moment as can be seen by comparing the phases for figure 2.6 A) and figure 2.6 B). To quantify the probability of one electron being emitted to the right or to the left (for figure 2.6, emission to the top or to the bottom) for one specific laser pulse, one can define the asymmetry parameter:

$$A = \frac{N_{\text{left}} - N_{\text{right}}}{N_{\text{left}} + N_{\text{right}}} \tag{2.14}$$

where N_{left} is the number of electrons being emitted left and N_{right} the number of electrons emitted to the right. The influence of the pulse duration on the asymmetry parameter can be seen already from classical considerations of HATI electrons trajectory. Decreasing the pulse duration influence the electric shape, the ionization probabilities of the positive or negative peaks and so the asymmetry parameter. It then appears that the shorter the pulse duration is, the larger asymmetry parameter is. This is confirmed experimentally in [SRM+11a]. Another effect of the φ_{CEP} is the final energy the photo-electron has after the laser pulse. By comparing figure 2.6 A) and 2.6 C), we can see that φ_{CEP} affects the time between ionization and recollision and more importantly, it affects the acceleration the electrons undergo after back-scattering, leading to different final energies. These backscattered electrons, which can acquire an energy up to ten times the ponderomotive energy[2] U_p, are sensitive to the φ_{CEP} and the asymmetry parameter varies with respect to their energy.

[2]The ponderomotive energy corresponds to the maximum energy an electron can acquire during its quiver motion in a laser field.

Experimentally, a spectrometer has been build to characterize the asymmetry and the energy of the photoelectrons [Hof09] (figure 2.7). The laser beam from the setup described in section 2.1.2 is split into two identical paths. One of the beams is focused inside the stereo-ATI spectrometer into a xenon gas. The electrons emitted are guided, with a magnetic field, to two detectors allowing to characterize their direction. The times of flight of the electrons to the detector are a measure of the energy.

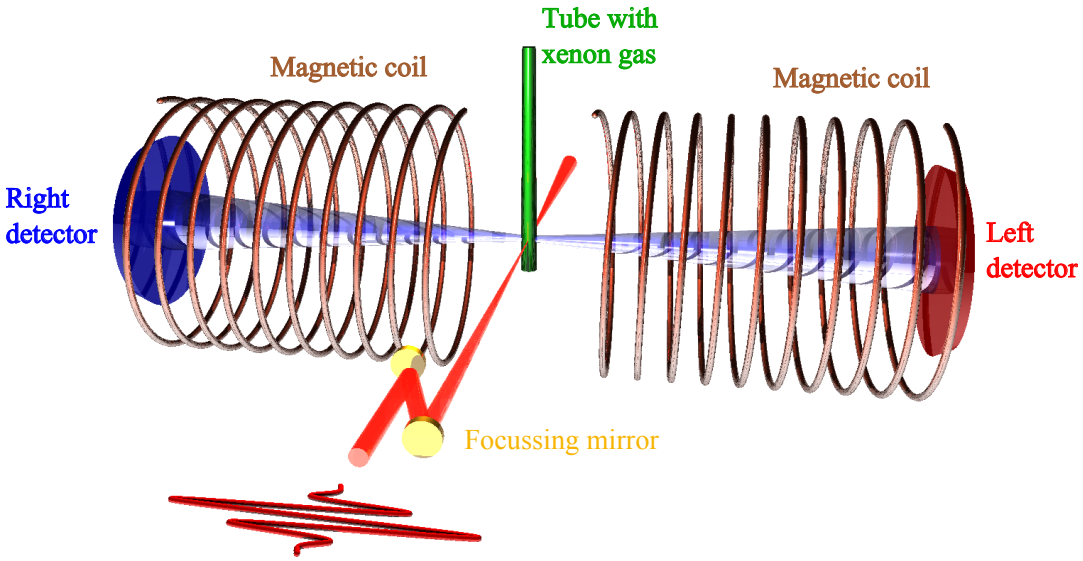

Figure 2.7: Schematic drawing of the Stereo-ATI spectrometer. The laser pulses are focused into a xenon gas. The photo-electrons are guided with a magnetic field to detectors delivering information about their emission direction and their energy.

2.3.2 The "phase ellipse"

The spectrogram obtained with the stereo-ATI (figure 2.8) represents the asymmetry A as a function of the φ_{CEP} of the laser (for that purpose the CEP was stabilized and recorded with a f-2f spectrometer) and the energy of the photo-electrons for a given laser beam. The maximum photo-electron energy is 75 eV, corresponding to $10\,U_p$. As described in the part 2.3.1, the asymmetry depends on the phase and on the energy of the photo-electrons. Observing the evolution of the asymmetry as a function of the φ_{CEP} for one energy would not deliver the full information about the phase because two different φ_{CEP} can lead to the same asymmetry parameter. For instance considering in the spectrogram (2.8) the "energy range 2" two phases (modulo 2π) leads to an assymetry value of zero (color green): 0.3 and 1.3 π rad. Taking into account the asymmetry for two energy ranges solves this uncertainty. The common process is to plot the asymmetry for one energy range as a function of the asymmetry for the other asymmetry range. We obtain an ellipse (also known as "phase potato") as shown in figure 2.9 A). The value of the CEP is not directly retrieved. To extract the phase, the axes are transformed such that the ellipse form a circle in the new basis as shown in figure 2.9 B). Each laser pulses represents a point on the circle. φ_{CEP} is equal to the angle that this point makes with the axes. The experimental advantages are that for each laser shot we are able to extract φ_{CEP}, it is referred as "phase tagging" and prevents from using any control on the phase. Furthermore, phase tagging is based on atomic processes like those we want to investigate in our main experimental chamber, meaning that we are sensitive to features of the pulses which are important for our main experiment. One example is the polarization of

the beam. It plays an important role in ionization through the recollision mechanism because this electron recollision is strongly suppressed when the polarization is not fully linear ([FBCK94]). For NSDI, we are looking for perfect linear polarization. This aspect can be characterized by looking at the recolliding electrons and can be investigated with the stereo-ATI.

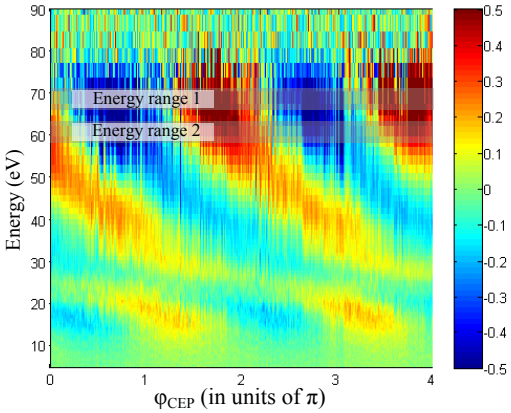

Figure 2.8: Spectrogram obtained from the stereo-ATI: asymmetry as a function of φ_{CEP} and the energy of the electrons.

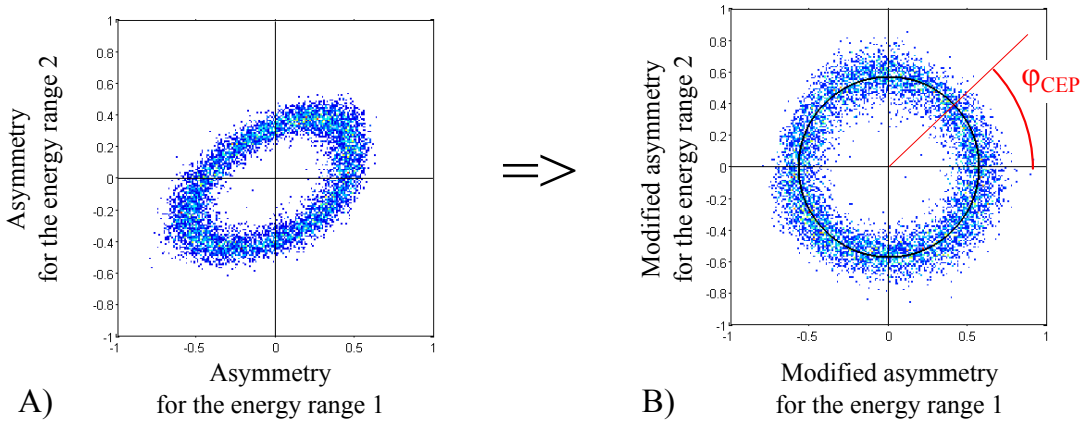

Figure 2.9: Phase ellipse. A) Raw phase ellipse obtained from representing the asymmetry parameter for one energy range as a function of the asymmetry parameter for another energy range. B) Modified phase ellipse where φ_{CEP} can be directly read from the angle of one point with the axis.

An important feature when comparing different phase measurement techniques, is the phase sensitivity of the detection scheme. In the case of phase tagging it can be approximated [SRM+11b] by

$$\Delta\varphi = \frac{\Delta r}{r}, \tag{2.15}$$

the width of the ellipse line divided by the radius of the ellipse. This value, for example for the phase ellipse of figure 2.9, corresponds to 300 mrad. This is larger than for the f-2f spectrometer where this value was calculated to be 100 mrad [Fis10] but under different conditions. First the

feedback control was used for the measurement of this last value but more importantly, this value was taken as an average over consecutive shots, stabilized at a given CEP, decreasing the noise. The implementation of the stereo-ATI in the feedback control of the CEP has been reported [SRM+11b], but the aim of the present work is to avoid CEP stabilization and to show that phase determination through CEP tagging is possible.

2.3.3 Long term pulse monitoring

Additionally, the stereo-ATI has two other very useful experimental applications. First of all, it is possible to optimize the pulses by changing the dispersive elements in order to look for the shortest duration. Relying on the fact that the asymmetry increases with shorter pulse duration [SRM+11a], a way to optimize the laser is to maximize the area of the ellipse by adjusting the prisms in the laser compressor, the pressure of gas in the hollow-core fiber and the amount of glass in the beam path. One could expect that optimizing once these parameters would lead to the same laser characteristics over time. Practically, a daily optimization is required and so a straightforward way to characterize the laser pulses.

Secondly, it allows to observe changes in the laser over time. Experimentally, running the laser with ultra-short pulses is only stable over few-hours. Its properties can be influenced by different changes such as temperature, humidity, laser alignment, etc. On the other hand, to study NSDI, the typical required time for obtaining enough statistics is 24 hours. During that time, one needs to make sure that the laser properties do not drift leading to a different pulse duration or intensity regime. The stereo-ATI allows this characterization.

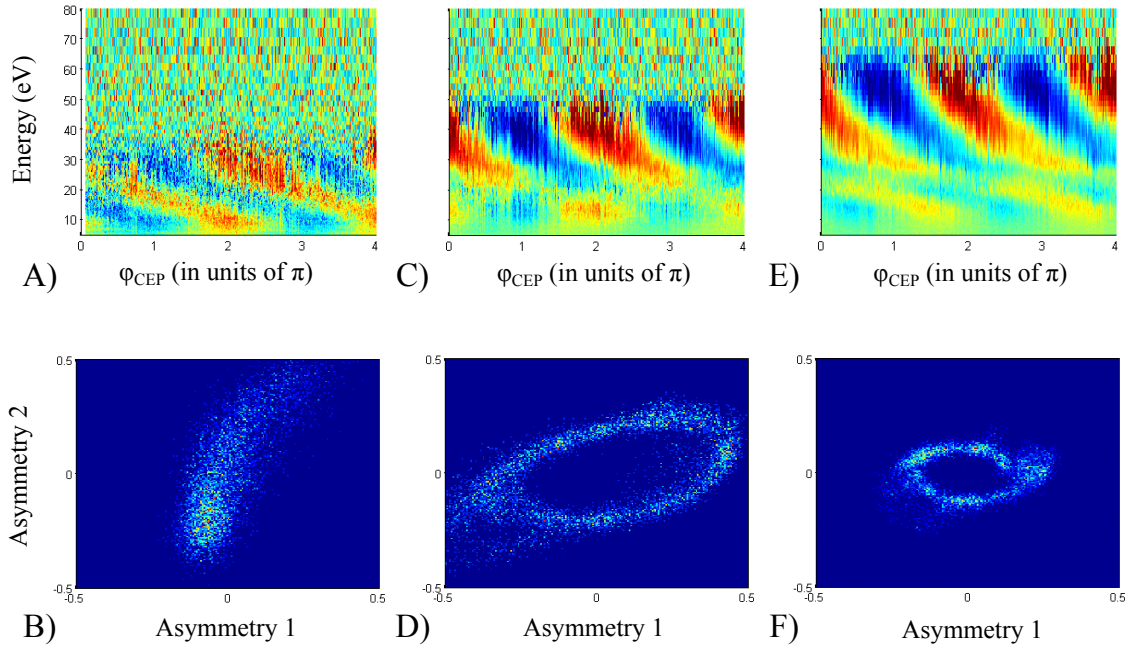

Figure 2.10: Spectrogramm (A,C,E) and the corresponding phase ellipse (B,D,F) for different pulse energy but with the same laser settings. For the left column the pulse energy is 13.3 μJ, for the middle one it is 15.3 μJ and for the right one it is 17.3 μJ.

Figure 2.10 shows different spectrograms (top row), for a given setting of the laser, when changing the pulse energy by means of an aperture in front of the spectrometer. Even though the change of pulse energy from 15.3 to 13.3 μJ and from 15.3 to 17.3 μJ is only of 13 %, the intensity shifts by respectively by 25 % and 35 %. This relative shifts is calculated by measuring the limit between the asymmetry pattern and the noise, corresponding to 10 U_p and being proportional to

the intensity of the laser. Because the change in pulse energy are made with an aperture size, this indicates that the laser intensity is sensitive to the beam profile. However, the contribution of each spatial coordinate of the beam to the intensity and pulse duration is unknown. Any change in one of this properties propagates to the phase ellipse. It can be clearly seen in the bottom row of figure 2.10. The energy ranges are chosen such that the best phase ellipse is obtained for the middle pulse energy. When using the same energy windows[3] for the photo-electrons, the phase ellipse for other pulse energies are strongly modified. The energy window is partly in the noise region for the low intensity case and is in a region with less asymmetry for the high intensity case.

To help understanding how such a phase ellipse changes over time, the evolution of the ellipse over 20 hours is shown in figure 2.11. This evolution represents a typical evolution of the laser. The figure shows the ellipse after different time, respectively at the beginning (figure 2.11 A)), after 6 hours (B), after 12 hours (C) and after 20 hours (D). The ellipse shrinks over time, confirming an elongation of the pulse duration over time. Unfortunately, the visible changes are only qualitative. One can extract the asymmetry parameters or the area covered by the ellipse but to which value does one consider that the laser has dramatically changed or has still similar characteristics? What are similar characteristics? This is mainly depending on what is currently achievable for such laser sources. After many tests of measuring phase ellipses over time (also performed at other laser facilities) we estimate that a change in the phase ellipse such as observed from the pattern of panel A) and the pattern of panel C) is reasonable and exploitable. The changes from the pattern of panel A) to the pattern of panel D) is considered as significant. The laser has drifted too much from its original characteristics.

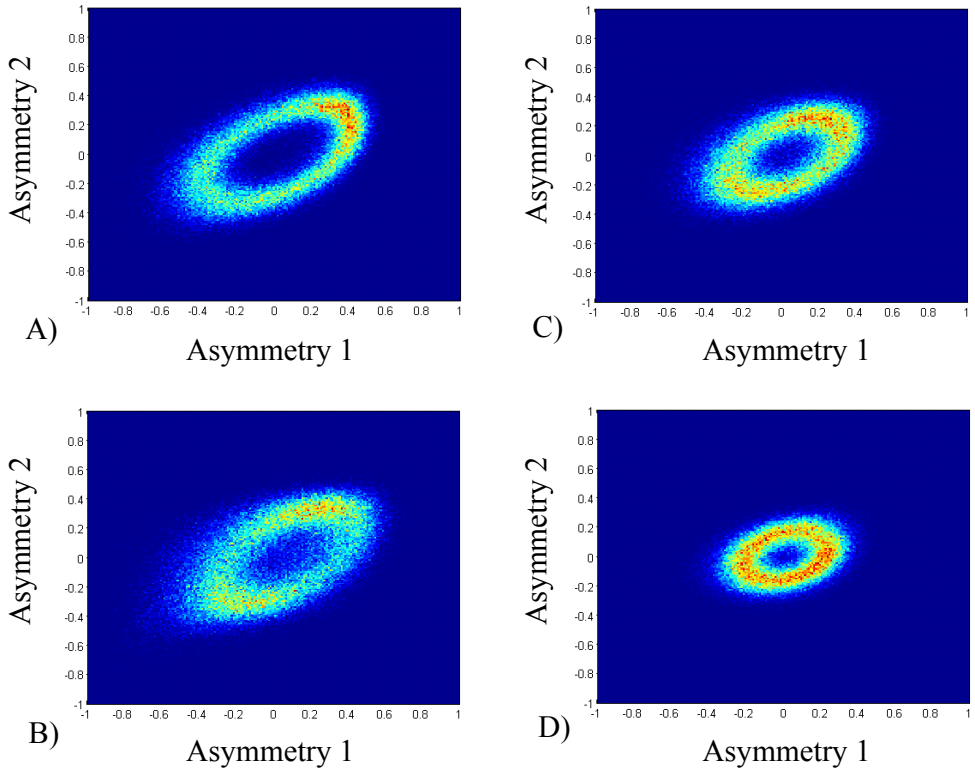

Figure 2.11: Phase ellipses measured over 20 hours. A) Phase ellipse at the beginning of the measurement. B) Phase ellipse after 6 hours. C) Phase ellipse after 12 hours. D) Phase ellipse after 20 hours.

[3]During one NSDI measurement these values are fixed.

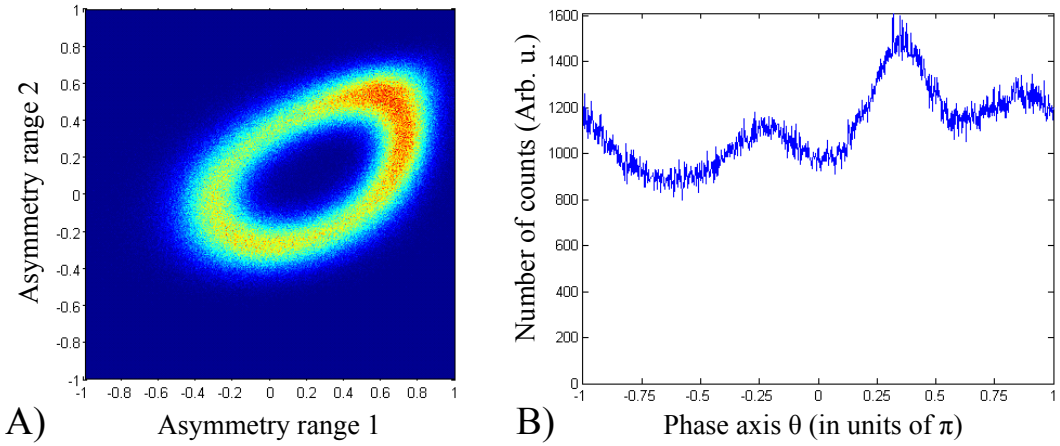

Figure 2.12: A) Phase ellipse. B) the "raw" phase distribution $\rho(\theta)$ extracted from it, being the number of laser shots for a given phase.

2.3.4 CE-phase tagging of individual pulses

During a measurement of few hours, if the extraction of the phase for each pulse is possible, one has however to calibrate the phase tagging method such that the phase distribution is uniform over 2π and that no drift is observed over time.

Homogenization of the phase probability

In figure 2.12, A) a phase ellipse measured with the phase tagging technique over a period of few hours is presented. Since it is not a perfect ellipse, the extraction of the phase leads to an inhomogeneous distribution as seen in figure 2.12, B), describing the number of laser shots per CEP. Because the phase of the laser is random, the distribution should be uniform over the $2\,\pi$ range. The distortion of the phase axis can result in a deviation of more than 30 % between the reconstructed and the real CE-phase. This effect counteracts the observation of CEP-effects and needs to be compensated. A procedure for the homogenization of the phase is realized by following the method described in [SRM+11b].

Defining $\rho(\theta)$, the phase distribution as represented in figure 2.12, B), the new phase axis θ_n must satisfies $\frac{d\rho(\theta_n)}{d\theta_n} = 0$. Mathematically this uniformity translates into the following: for any value a between 0 and 2π, the equation

$$\int_0^a \rho(\theta_n) = \frac{2\pi}{a} \int_0^{2\pi} \rho(\theta) d\theta \ , \tag{2.16}$$

must be satisfied. To build the new axis θ_n, the value of a is iteratively increased from 0 to $2\,\pi$. The conversion between the new axis θ_n with a uniform phase distribution and the old axis θ is calculated and shown in figure 2.13, A). In case the initial distribution would be uniform, the conversion curve would be represented by the black diagonal. The distribution in the new axis of coordinate is shown in panel B) where it is confirmed that the phase distribution is uniform over 2π. Since the $\rho(\theta)$ distribution is varying over time this procedure must be repeated continuously during the experiment. The only condition being that the segments of time contain sufficient number of events to allow such an implementation (e.g. steps of 20 minutes).

Long term calibration of the CE-phase

The variations of the phase ellipse over time such as displayed in figure 2.11 introduce a drift of the value of the extracted phase over time. To compensate for this drift we use the measurement of the asymmetry in the emission direction of the target which is ionized and studied in the Reaction

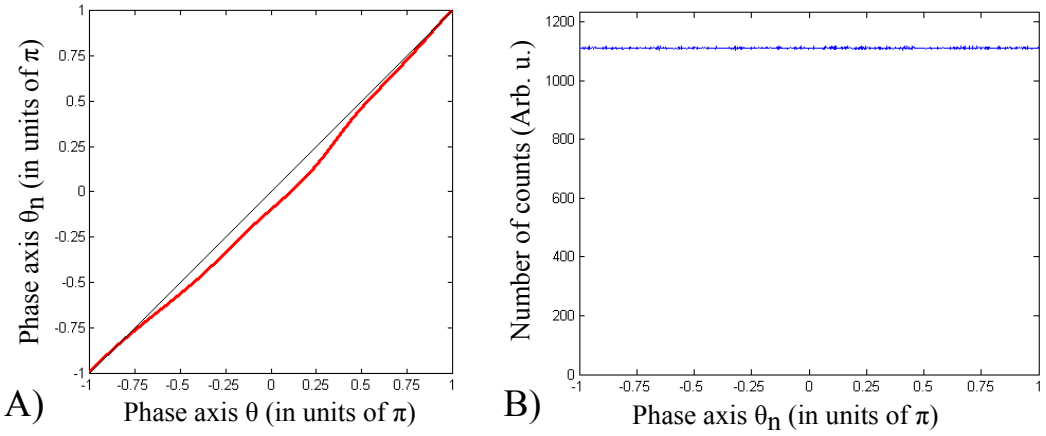

Figure 2.13: A) Red curve: Representation of the change of coordinate between the calibrated phase θ_n and the raw phase θ. Black curve: diagonal of the graph to outline the deviation of the red curve. B) Calibrated phase distribution $\rho(\theta_n)$.

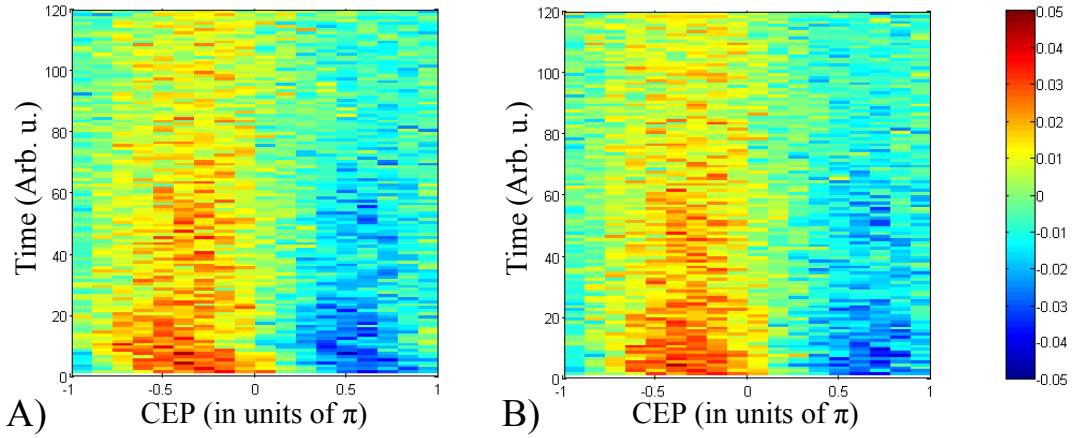

Figure 2.14: CEP asymmetry for different time segments for Ar^+. A) Raw data. B) Corrected data.

Microscope. The procedure follows the study made in [KBJ+12]. The assumption is that the maximum of asymmetry in the singly charged ion stays at a constant CEP value over time. The CEP axis is changed in consequence. In figure 2.14 A) the asymmetry of Ar^+ is represented for different time segments over a total time of 20 hours. Deviations of the maximum in asymmetry can clearly be identified, for example at a time of 15 Arb. u., the phase shifts by -0.3π. Similarly to the deterioration of the phase ellipse over time, the value of the maximum in asymmetry decreases due to an elongation of the pulse duration. Applying a correction for CEP drifts we obtain graph B).

This algorithm was applied to the data presented in the chapters 4 and 5 in order to obtain clearer CEP-effects and therefore observe more easily the CEP dependence of the ion and electron momentum distributions.

The stereo-ATI spectrometer relies on ionization of xenon atoms. When dealing with ultrashort pulses, it is a preferential tool for characterizing the laser pulses, optimizing the optical elements on the beam path and investigating the long term stability of the laser. These characterizations are due to the large sensitivity of the spectrometer to the pulse shape of the laser which depends on the wavelength, the polarization, the intensity and the pulse duration.

2.4 Generation of two-color laser pulses

This section treats a different topic but is also related to the modification of the electric field of the laser pulses. In order to achieve this we superimpose a second harmonic (SH) field with the fundamental.

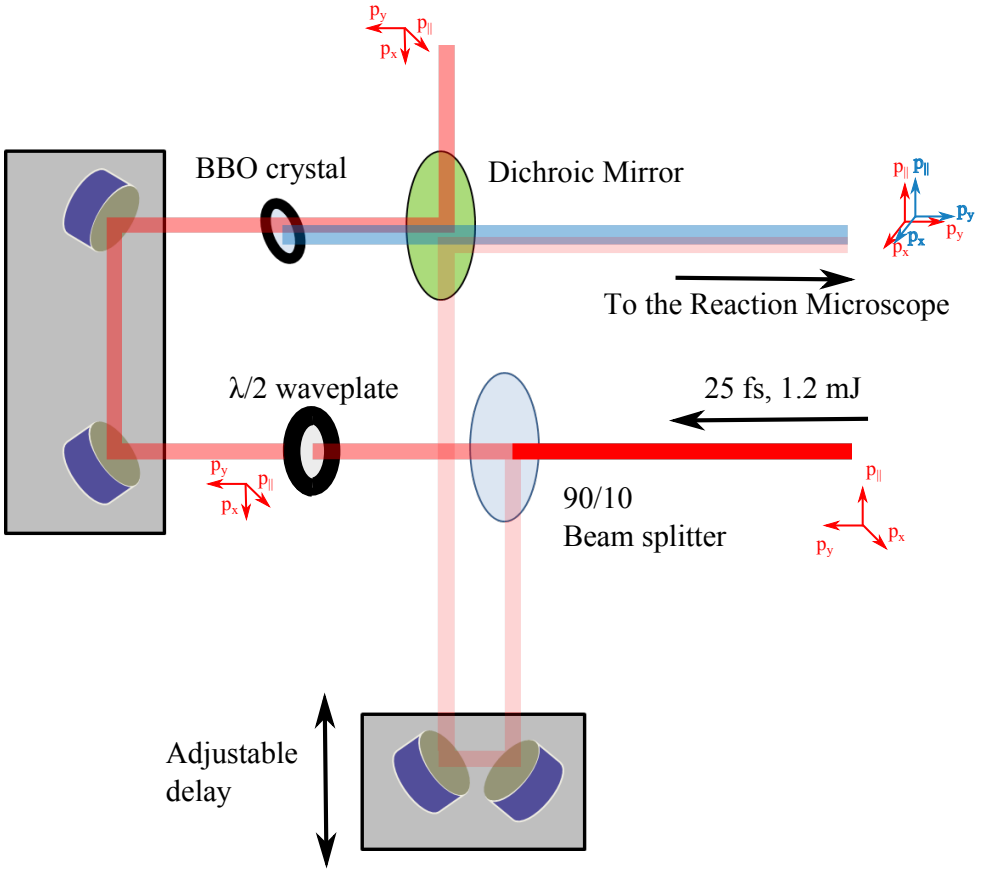

Figure 2.15: Two-color Mach- Zehnder type interferometer, see text for description.

The set-up developed for the creation and addition of a second harmonic (SH) laser field is a two-color Mach-Zehnder (MZ) type interferometer as depicted in figure 2.15 (already introduced in [EEN+95]).

The red fundamental beam is split into two parts. One part creates the SH and is afterwards dumped. The other part is unaffected and goes to the Reaction Microscope. Because of the conversion efficiency from red to blue, the two parts are not equally intense, a 90/10 entrance beam splitter is used. The part containing 90% of the original beam is sent to maximize generation of SH in a 200 μm type I BBO crystal. This harmonic generation process induces that the polarization direction of the SH and the fundamental are perpendicular. Since we are interested in having the

two colors wih parallel polarizations in the Reaction Microscope, we turn the polarization of the fundamental with a $\lambda/2$ waveplate.

The other arm of the interferometer contains two reflecting mirrors mounted on a high accuracy delay stage. This stage can selectively change the length of the arm such that a maximum delay of 3 picoseconds can be introduced to the pulse with a precision of 80 as [Erg06]. Both beams are recombining on a dichroic mirror, having good reflection properties for the fundamental and good transmission properties for the SH. The two beams propagates towards the Reaction Microscope.

The temporal overlap of the two beams after the MZ is verified through two methods. The first, optical one is the investigation of interferences between the SH beam and the doubled frequency component of the fundamental one. This method is equivalent to the f-2f method (section 2.2.2). The fine tuning of the zero delay of the interferometer is realized by studying the ionization yield of krypton[4] as a function of the delay between the red and the blue beams. This ionization yield as a function of the MZ delay is shown in figure 2.16. The maximum yield signal is obtained for the best temporal overlap between the two beams. The measurement of the center of the shallow peak on the left of the curves determines the position of the MZ where the delay between the two colors in the Reaction Microscope is zero.

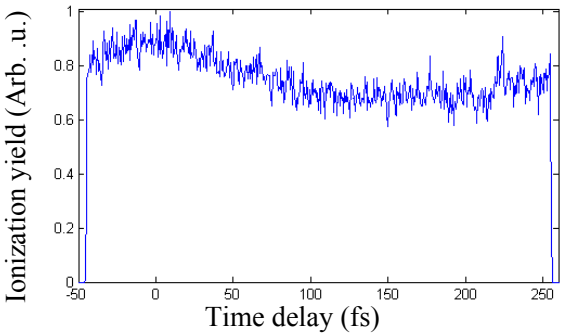

Figure 2.16: Ionization yield of Kr^+ as a function of the delay between the two colors.

[4]Krypton is more easily ionized than argon: $I_p^{Kr} = 13.99\,\text{eV}$ while $I_p^{Ar} = 15.76\,\text{eV}$.

Chapter 3

The Reaction Microscope

One main goal in experimental physics is to increase the amount of information that is accessible in a measurement of a physical process while at the same time increasing the precision associated with the measurement. In the case Non-Sequential Double Ionization (NSDI) in strong laser field, this increase of experimental information has been capital for its present understanding. The first manifestation of NSDI was observed in the early 1980s with a reported increase of ion yields of the multiply charged krypton in comparison to the theoretical predictions from tunneling theory [LLMM82]. Different theoretical approaches were proposed (recollision, multi-electron tunneling, shake off), but one had to wait for the first measurements of the ion momentum distributions [MFS$^+$00, WGW$^+$00] to confirm the origin of NSDI to be the recollision mechanism. These measurements were made possible by the use of a Reaction Microscope (ReMi, also called COLTRIMS) [UMD$^+$03]. At the same time, again with a Reaction Microscope, electrons were recorded in coincidence with the doubly charged ion [WWS$^+$00a], allowing to measure the correlation between the two electrons, confirming the recollision mechanism. This correlation was observed in the momentum components of the electrons parallel to the laser polarization. In later studies looking at the perpendicular momentum components [WBS$^+$03, WZS$^+$04, RdJE$^+$07] permitted a deeper look into the mechanism. Further indications on the electron interaction and the state of the system after recollision were obtained.

The ReMi is also the spectrometer used for the measurements presented in this work. In the first part, we will describe the principle of the ReMi and its advantages and limitations. The second part explains how to use it in order to retrieve the momenta of electrons and ions measured in coincidence.

3.1 Working principle

The reaction microscope (figure 3.1) allows to record the momentum vectors of charged particles in coincidence. The laser is focused onto a supersonic gas jet inside an ultra high vacuum chamber (10^{-11} mbar). An electic field accelerates the charged particles to the different detectors. The advantage in comparison to conventional time of flight spectrometers is the implementation of a magnetic field [MUU$^+$96] with Helmholtz coils. Due to the Lorentz force, all electrons are guided to the detector following a cyclotron trajectory. This enables the detection of electrons with large transverse momentum and to reach a 4π detection angle for almost all particles.

The coincidence measurement of the detected particle is an additional advantage of the spectrometer. Due to momentum conservation, the coincidence allows to determine, for a given pulse, all the emitted particles belonging to the same atom/molecule and thus to reconstruct the full kinematical information of the ionization reaction. In case the use of momentum conservation is restricted, if some particles are not detected, the missing information can be reconstructed from the measured ones. In return of this possibility, the number per laser pulses of ionization events which can be investigated is limited.

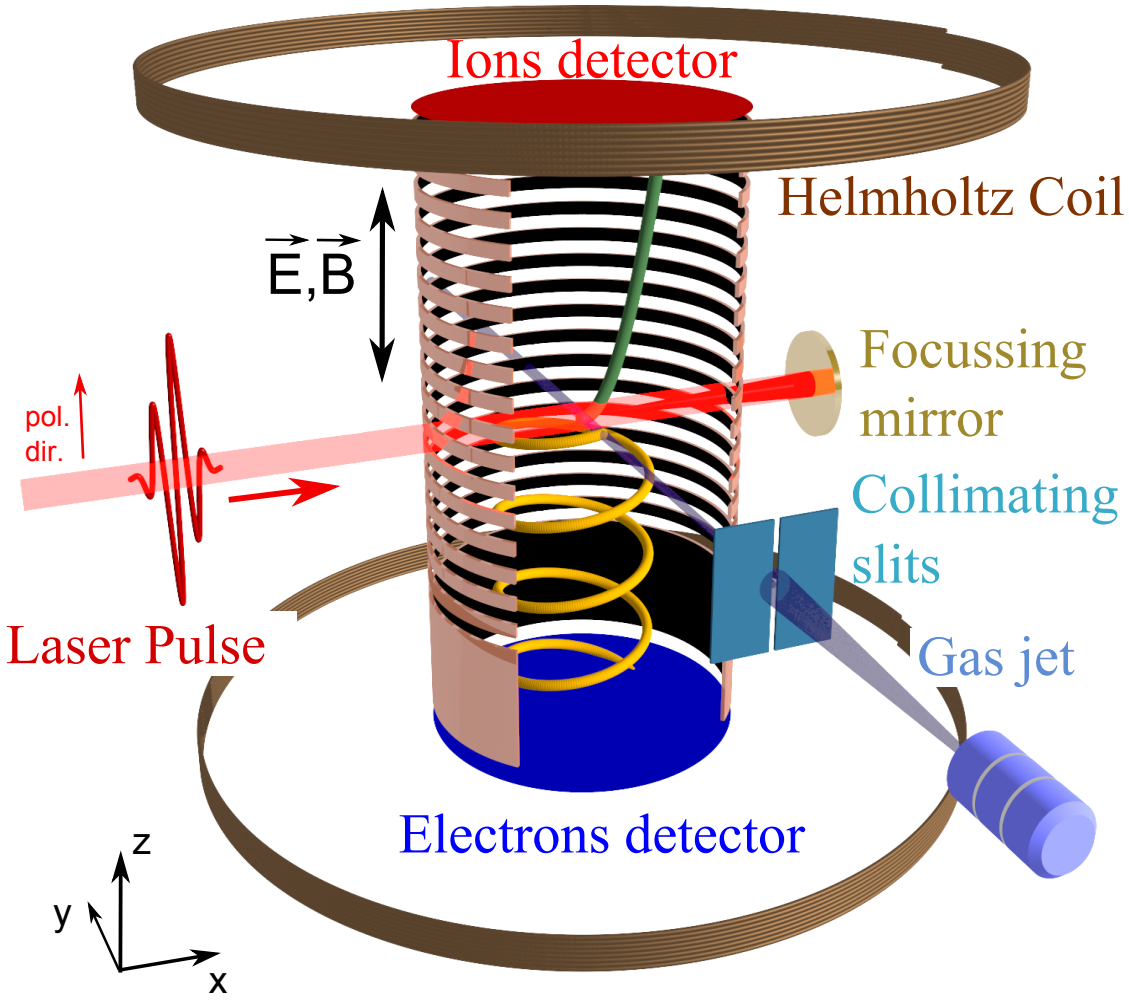

Figure 3.1: Schematic drawing of the Reaction Microscope. A laser pulse (red) is focused inside the spectrometer onto an ultra-cold gas jet (blue). The typical trajectories of an ion (green) and an electron (yellow) are depicted. They are guided by the electric and magnetic fields to their respective detector. Two parts of the spectrometer can be distinguished: the ion part, where the electric field along the spectrometer is constant (acceleration part, equal metal rings connected by identical resistors) and the electron part composed of an acceleration part and a drift part where the voltage is constant (equal metal rings connected by a wire).The directions are defined such that "z" is the main axis of the spectrometer, along which the electric and magnetic fields are applied, "y" is the direction of propagation of the gas jet and "x" is the remaining axis, perpendicular to "y" and "z". The laser polarization (longitudinal direction) is chosen such that it is parallel to the z-axis.

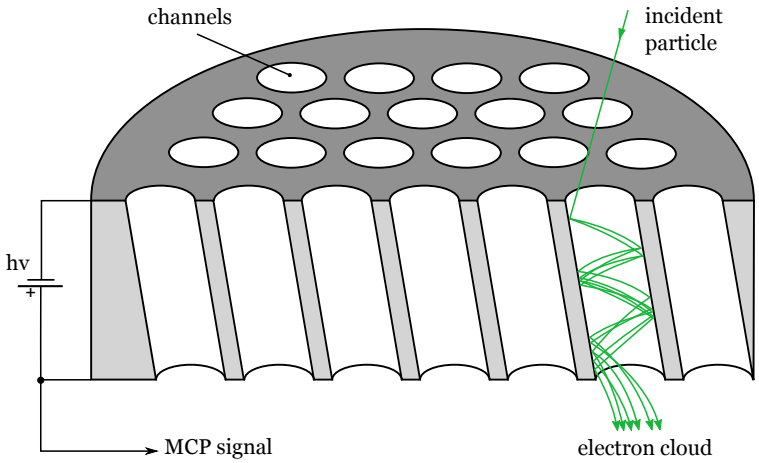

Figure 3.2: Schematic drawing of a micro-channel plate, taken from [Pfl12].

3.1.1 Particle detectors

The detectors are composed of two micro channel plates (MCP) (figure 3.2). Charged particles impinging on the MCP release electrons from the channel surface. These secondary electrons are accelerated to the back of the plate by a high voltage ($\approx 1\,\text{keV}$ across the channel). The channels act as an electron multiplier producing an electron cloud at the output of the channel, in order to record a measurable signal per particle. A position sensitive anode (delay line anode) is used to detect the electron cloud together with the particle impact position on the MCP.

An important parameter is the detection efficiency of the MCPs. Taken that every particle entering a channel is detected, those impacting on the surface of the partition walls between the channels are not. The efficiency is given by the geometrical ratio between this inter-space and the channel area and is estimated to be 50%. Experimentally, this means that some coincidences are not recognized. For instance, if only one electron is recorded in coincidence with two singly charged ions having a difference in momentum smaller than the resolution of the apparatus, one can not know to which ion it belongs. To circumvent this drawback, there should be one and only one ionization per pulse. Unfortunately, this decreases the acquisition rate and elongates the measurement time. For the work presented in this thesis, the probability of ionization was set to 0.40. This also means that if we record an ion of interest (doubly charged), the probability of having another ionization event during the same laser pulse is 0.4.

Another limiting effect linked to the detector and the electronic system used to read incoming signals is the dead time it corresponds to the minimum time required between two different incoming particles on the detector so that the two electronic signals can be separated. It is equal to 15 ns for this setup. This time is comparable to the average time difference between two different electrons and influence electron detection. For the spectrometer and the voltage applied in the presented experiments, 70% of all electrons arrive within an interval of only 120 ns. This means that two electrons emerging from the same event with similar longitudinal[1] momentum can not be detected. In experiments where NSDI is studied, the "correlation plot" representing the longitudinal momentum of one electron as a function of the longitudinal momentum of the other is analyzed. Because of the dead time, an area of the correlation plot is inaccessible when recording the two electrons in coincidence. In figure 3.3 the influence of this dead time is shown. The longitudinal momentum distribution for two electrons is depicted. Per definition, electron with positive momentum value are the fastest (arrives first on the detector). Therefore only the bottom right half of the graph is populated. An event appearing on the diagonal $p_1 = p_2$ would

[1] longitudinal means parallel to the laser polarization and is, by choice, also parallel to the spectrometer axis

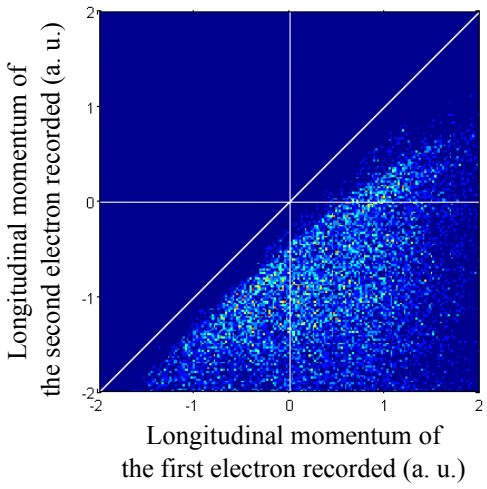

Figure 3.3: Distribution of the longitudinal momentum of the second electron recorded as a function of he first electron recorded

correspond to the two electrons arriving at the same time. An area below the diagonal is not populated due to dead time. This area, below the diagonal, is not constant in size because the longitudinal momentum value is not proportional to the time of flight. Additionally some structure can be seen in the momentum plot (lines close to the $p_1 = p_2$ diagonal). There are due to noise created by the first electronic pulse (ringing artifacts) and modifies the second pulses. Therefore, recording processes involving a doubly charged ion and two electrons is biased when looking at the two electrons in coincidence. For NSDI, we do not consider the events where two electrons or more are detected. We reconstruct the second electron from the ion and the detected electron. We take into account only events where one and only one electron is recorded. In principle, the events where the second electron is not detected due to dead time should add to the events with only one electron detected. We do not correct the correlation plot for these.

Again, since we can not verify that the electron detected is the relevant one, the probability of having more than one ionization event per pulses should be kept low.

The physical limitations from the detector and the associated electronics leads to a loss of coincidence and a restriction on the reconstruction of the events. This requires a decrease of the statistics and a longer measurement time, itself restricted by the laser stability as discussed in part 2.3.

3.1.2 The gas jet

The properties of the gas jet also influence the measurement of the ionization processes. First, the temperature of the gas defines the spread in the initial momentum of the particles. For example, for argon at room temperature the momentum spread is Δp= 13.4 a.u. This is much larger than the typical momentum a photo-ion acquires from the laser field, of the order 0.5 a.u. The gas is cooled by supersonic expansion. This is done by passing the gas through a nozzle, where the background pressure behind the nozzle is much lower than in front of it. In the ideal case, the gas undergoes an adiabatic expansion where its enthalpy is converted into a directed motion. Its temperature decreases to few mK in the direction perpendicular to the propagation of the gas jet and few K in the direction of propagation. Practically, the expansion and the temperature depend on many parameters (pressures, nozzle size) extensively covered in [Mil88]. The jet temperatures define the momentum resolutions of the spectrometer which value can be measured (cf. section 3.2.3).

The size of the gas jet is also an important factor. It defines the size of the interaction volume between the gas and the laser in the direction of laser propagation[2]. In this direction the Gouy effect [Gou90] has to be considered. It is a shift of the phase of light through the focus along the propagation direction of the laser. The phase relation over the distance "z" from the focus is described by the expression:

$$\phi(z) = -\arctan(\frac{z}{z_R(\lambda)}) \tag{3.1}$$

where $z_R(\lambda)$ is the Rayleigh range, depending, for a given laser mode and focusing, on the wavelength. It indicates the distance from the focus where the beam diameter is twice the focal waist. Because of its wavelength dependence, the phase and group velocities are different leading to a shift of the value of the CEP close to the focus. For laser characteristics similar to ours, this shift was estimated to be linear close to zero and equal to $\pi/2$ over less than two millimeters [LPW+04]. This effect provides from seeing ionization of atoms for a single CEP since different part of the interaction volume have different value of CEP. To decrease the CEP averaging effect and the size of the interaction volume, two slits (collimating slits in figure 3.2) are implemented, to cut the gas jet spatially in the propagation direction of the laser beam.

3.2 Momentum reconstruction

As mentioned in section 3.1.1, the observables directly measured from the spectrometer are the time of flight and the position of impact of the detected particle. In the following we will present how they relate to the momentum of the ions and the electrons through the dimensions of the spectrometer and the applied electric and magnetic fields.

3.2.1 Reconstruction of the ion momentum

The component of the momentum parallel to the spectrometer axis can be reconstructed from the time the particle needs to reach the detector. The general expression for this time, for a particle of mass m, charge q, and initial momentum $p_\parallel$ parallel to the spectrometer, is:

$$t(p_\parallel) = m\left(\frac{2a}{\sqrt{p_\parallel^2 + 2mqU} + p_\parallel} + \frac{d}{\sqrt{p_\parallel^2 + 2mqU}}\right) \tag{3.2}$$

where a is the length of the acceleration region, across which the electric field is constant, d the length of the drift region, across which the voltage is constant, and U the extraction voltage. In the present case, for the ion spectrometer, $d = 0$ and assuming that the kinetic energy $E_\parallel = \frac{p_\parallel^2}{2m}$ is small in comparison to qU, the momentum follows the expression:

$$p_\parallel = \frac{qU}{a}(t_0 - t) \tag{3.3}$$

with t_0 the time taken for an ion with no initial momentum to reach the detector. When considering $p_\parallel$, q in a.u., qU in eV, a in cm and t, t_0 in ns,

$$p_\parallel = 8.04 \cdot 10^{-3} \cdot \frac{qU}{a}\Delta t \tag{3.4}$$

Figure 3.4 shows the time of flight obtained for ionization of argon by 25 fs laser pulses at 800 nm. On the large scale (A) it can be seen that the species can be differentiated with respect to their mass by charge ratio (m/q). In the present example, $^{40}Ar^+$, $^{36}Ar^+$, $^{40}Ar^{2+}$ originate from the jet, while H_2O^+ and H_2^+ are from the residual gas in the chamber. The position of the peaks follows equation 3.2. In figure 3.4 B) the peak for $^{40}Ar^+$ is represented as a close up. The equivalence between time and momentum is described by equation 3.4.

[2]The width of this interaction volume perpendicular to the laser propagation depends on the focal spot size. It is of the order of few tens of microns.

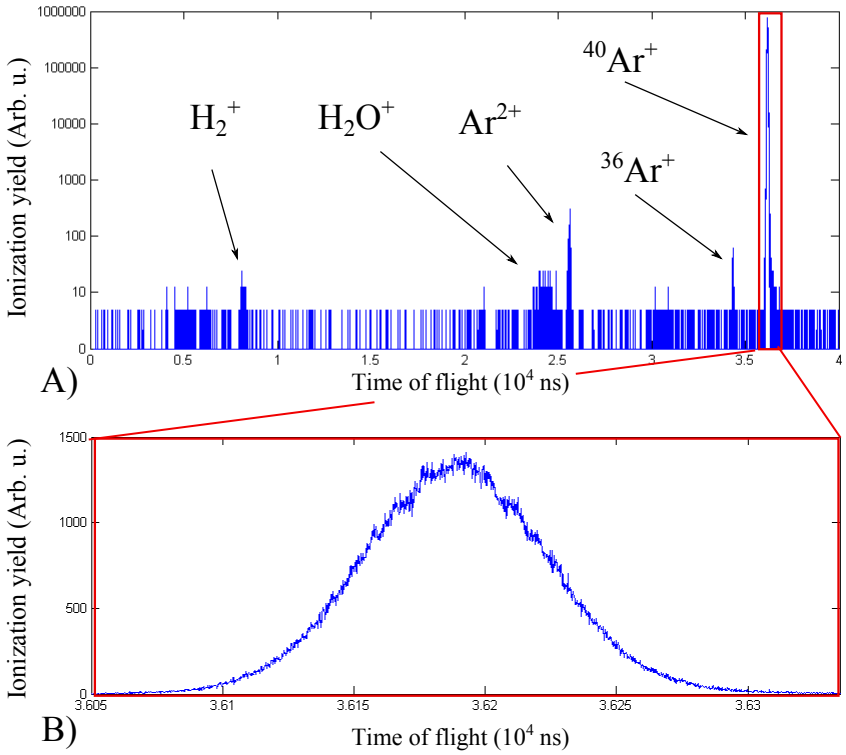

Figure 3.4: Time of flight spectra for the ionization of argon (and residual gas) by a 25 fs, 800 nm laser pulses. A) Span of few tens of microns where all the different products of ionization are visible. B) Zoom on the peak of $^{40}Ar^+$.

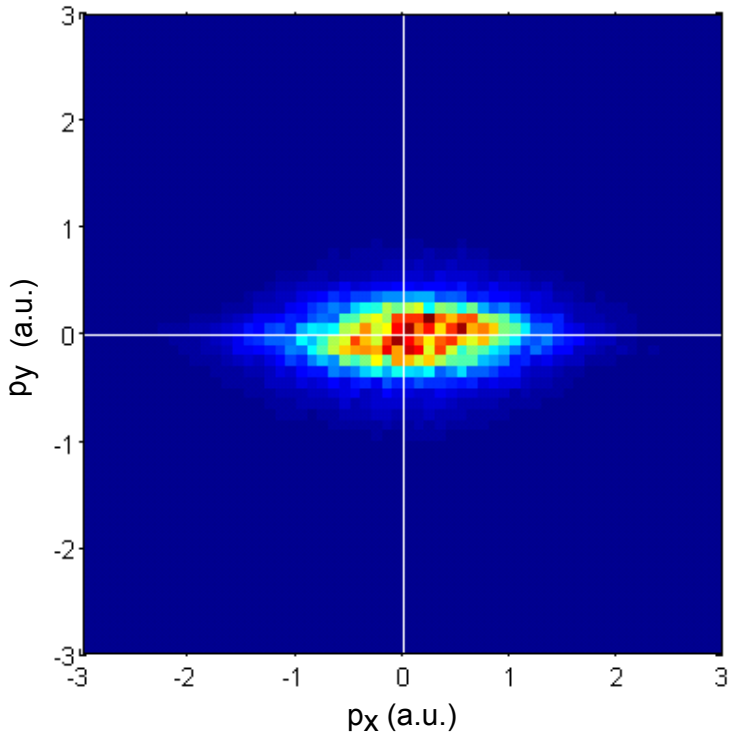

Figure 3.5: Tranverse momentum py as a function of px for $^{40}Ar^{+}$ ions.

The transverse momentum can be calculated from the time of flight of the ion and the position (x_p,y_p) on the detector, following the expression:

$$p_{\perp} = \frac{R \cdot m}{t} \tag{3.5}$$

With $R = \sqrt{x_p^2 + y_p^2}$ the distance from the center. Assuming the time of flight of the ion to be t_0 ($\Delta t << t_0$), the transverse momentum of a particle of charge q and mass m is:

$$p_{\perp} = 11.6 \cdot \frac{R \cdot \sqrt{mqU}}{2a} \tag{3.6}$$

With $p_{\perp}$ in a.u., R in cm, m in amu, qU in eV and a in cm.

In figure 3.5 the transverse momentum (the two components p_x and p_y forming it) for $^{40}Ar^{+}$ are shown. The momentum is calibrated such that the x-axis corresponds to the gas jet direction. One can clearly see the spread in momentum due to the temperature which is not the same in both directions of the expansion as described in 3.1.2. This has a consequence on the reconstruction of the electron momentum via momentum conservation. Since the ion distribution is not rotationally symmetric but the electron distribution is, the reconstructed transverse momentum is not rotationally symmetric. This provides a bias on the angle, define in the transverse plane, measured between the recorded and the reconstructed electron. Therefore, the transverse momentum of the ion is not used for the present study of NSDI.

3.2.2 Reconstruction of the electron momentum

For the detection of electrons, the overall principle is the same as for the ion imaging, but due to their low mass, electrons with a large transverse momentum would not reach the detector if no additional magnetic field would be applied. For instance, an electron having a 150 ns time of flight

(average value) and a transverse momentum superior to 0.12 a.u. does not reach the detector, without magnetic field. The applied magnetic field is parallel to the spectrometer in order to "guide" the particles onto a helical trajectory to the detector. It does not affect the longitudinal motion of the electron and equation 3.2 for the time of flight holds. In the present case, the drift region is non zero and $p_{\parallel}$ is calculated by solving equation 3.2 numerically. The transverse momentum is related through the position of the electron on the detector and its time of flight (figure 3.6). Considering the projection of the electron trajectory on a plane perpendicular to the spectrometer axis, an electron with an initial transverse momentum $p_{\perp}$ will travel on the dark green circle of radius R in figure 3.6:

$$R = \frac{p_{\perp}}{qB}, \tag{3.7}$$

where B is the magnetic field, resulting in a cyclotron frequency of $\omega_c = \frac{qB}{m_e}$.

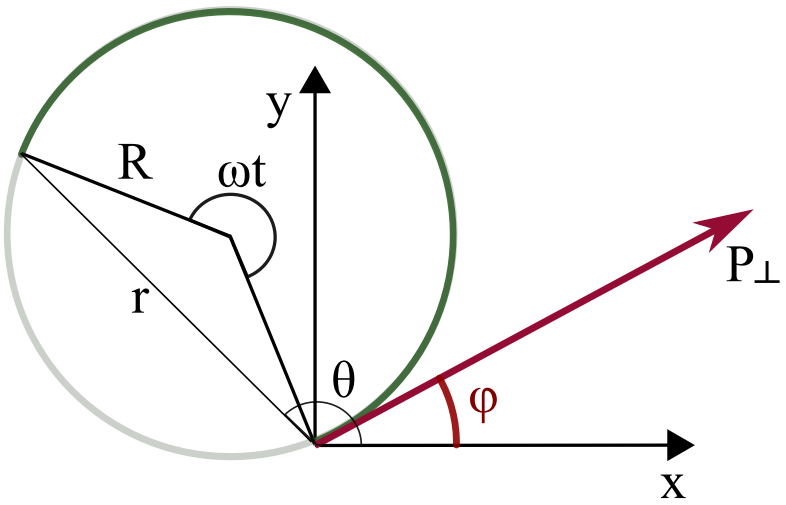

Figure 3.6: Schematic drawing of the trajectory of an electron in a plane perpendicular to the spectrometer axis.

Depending on the time t the electron needs to reach the detector, the angle ωt varies, and from the position (r,θ) on the detector and the time of flight t, R and φ can be extracted. φ is the initial angle between $p_{\perp}$ and the perpendicular axis of the spectrometer.

$$R = \frac{r}{|2\sin(\omega t/2)|} \tag{3.8}$$

$$\varphi = \theta - \omega t/2 \mod(2\pi) \tag{3.9}$$

The cyclotron trajectory implies that when the time of flight is equal to $n \cdot \omega_c$ with n an integer, all the electrons arrive on a single point on the detector, placed on the same transverse position than the interacting volume.

In figure 3.7, the top panel shows the radial position of the electron as a function of the time of flight. Time of flight values of 68, 135 and 203 ns are the nodal points, when all electron trajectories come back to the original (x_p,y_p), after an integer number of cyclotron periods (corresponding to a magnetic field of 5.3 Gauss). These nodes are used in the calibration to determine precisely the value of the magnetic field and the value of the offset time t_0 when the interaction happens and the electrons start their trajectory. Calculating the transverse momentum leads to a spectrum

shown in figure 3.7 B). The nodal points have a different shape, forming lines. At these times no information about the transverse momentum can be extracted. The width of these lines depends on the spectrometer resolution and the field applied (at best they should be infinitely small), in the present case the width is less than 1.5 ns.

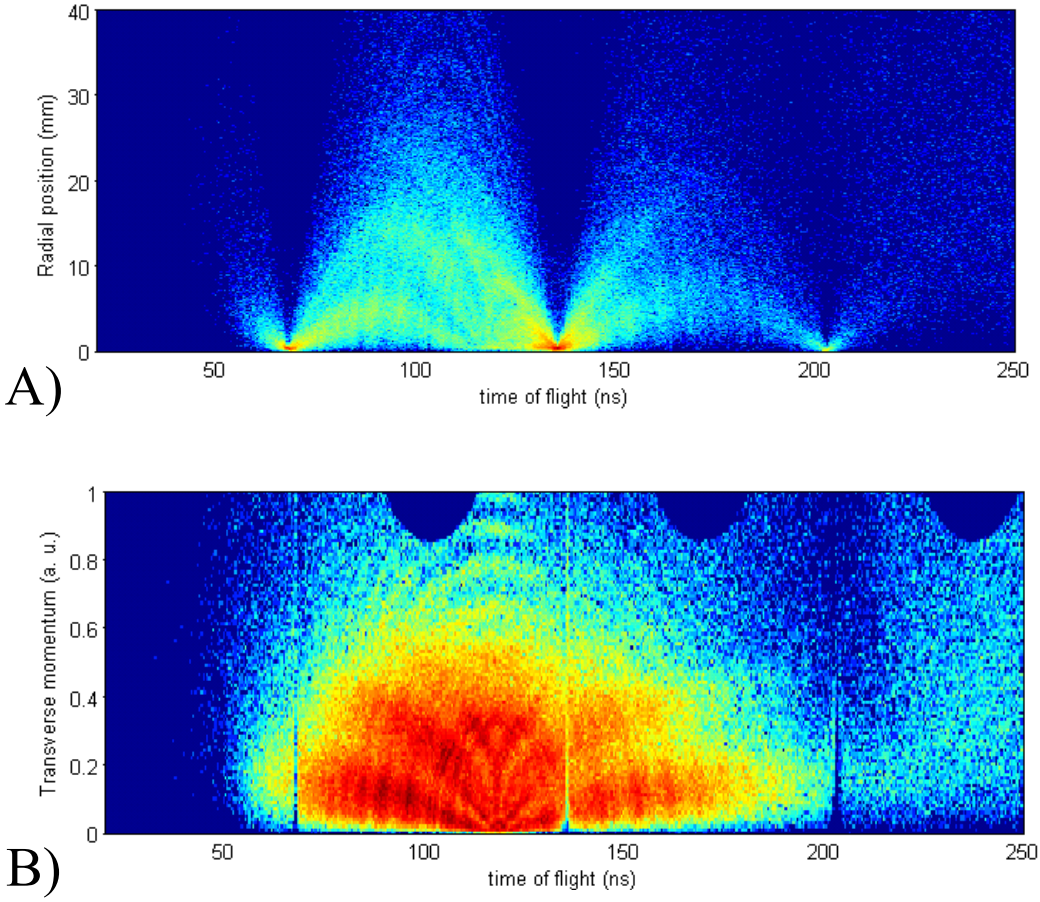

Figure 3.7: A) Radial distribution of the electron on the detector as function of the time of flight, B) Transverse momentum calculated as a function of the time of flight. In both graphs, the color scale is logarithmic in order to outline details.

3.2.3 Momentum acceptance and resolution

The acceptance is defined as the maximum energy/momentum the considered particles can have in order to still be detected. As shown by equations 3.2, 3.5 and 3.7, it is directly linked to the spectrometer voltages and detector size. For the longitudinal direction, the acceptance can be seen if the particles go in the direction opposite to their detector and if their energy is such that the electric field cannot compensate for this. This is given by the condition

$$p_{\parallel}^{\max} = \sqrt{2mqU} \tag{3.10}$$

For the ions (e.g. $^{40}Ar^{+}$), due to their large mass, this value is not a restriction. For an applied electric field (2 V/cm), we have $p_{\parallel}^{\max} > 300$ a.u. For electrons, we obtain $p_{\parallel}^{\max} = 2.1$ a.u., this value is still higher than the typical value of longitudinal momenta obtained with linear polarized light at 800 nm. This becomes problematic for experiments with longer wavelength or circular polarized light.

Concerning the transverse momentum acceptance, the condition for the ions follows equation 3.5 and is described by:

$$p_{\perp}^{\max} = \frac{R_{\mathrm{det}} \cdot \sqrt{mqU}}{2a} \tag{3.11}$$

with R_{det} the radius of the ion detector, being equal to 6 cm and for $^{40}Ar^{+}$, $p_{\perp}^{\max} > 30$ a.u.

For the electron the expression is:

$$p_{\perp}^{\max} = \frac{R_{\mathrm{det}}}{2} \cdot qB \tag{3.12}$$

with B being of the order of 10 Gauss and $R_{\mathrm{det}} = 4$ cm, $p_{\perp}^{\max} = 1.61$ a.u. also larger than the common value as can be seen in figure 3.7, B).

The experimental resolutions for this specific spectrometer are referenced in [dJRF^{+}04]. For the electrons, the longitudinal momentum resolution is limited by the resolution of the time of flight measurement and gives $\Delta p_{\mathrm{long}} \leq 0.01$ a.u. For the transverse resolution, the value depends on the time of flight, a factor $\frac{1}{|2\sin(\omega t/2)|}$ has to be considered. At the node of the magnetic field the resolution is zero (all $p_{\perp}$ are at the same position). For the point exactly in between two nodes in time ($|2\sin(\omega t/2)| = 1$), the resolution depends on the position resolution of the detector, estimated to be 100 μm and giving $\Delta p_{\perp} \leq 0.01$ a.u.

For the ion resolution, the internal temperature of the jet is the main limitation. In [dJRF^{+}04], this value was obtained for helium. For argon, we look at the sum momentum between an ion and the coincident electron. Figure 3.8 shows the longitudinal momentum sum of Ar^{+} and the electrons recorded in the same pulses. The wide background, extending to 1.0 a.u. corresponds to events where the two particles do not originate from the same atom. The middle sharp peak corresponds to coincident events. Its width at half maximum is equal to 0.1 a.u. Considering that the electrons have a much better resolution, the maximum value for the ion resolution is $\Delta p_{\parallel} = 0.1$ a.u. We use the same consideration for the values transverse to the spectrometer axis. We find, for argon, for the direction parallel to the jet propagation: $\Delta p_{\mathrm{jet}\parallel} = 0.6$ a.u. and for the component perpendicular to the jet propagation $\Delta p_{\mathrm{jet}\perp} = 0.25$ a.u.

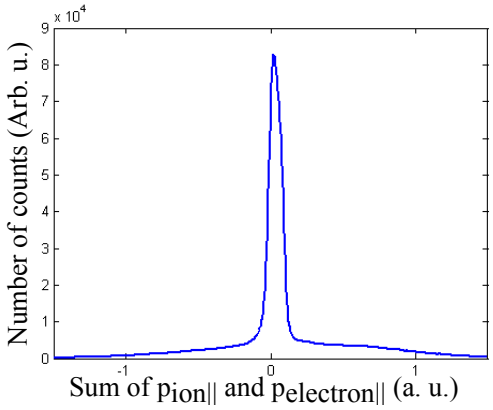

Figure 3.8: Sum of the longitudinal momenta of Ar^{+} and the different electrons which are recorded in the same pulse.

Chapter 4

Measurements with CE-phase tagged few-cycle pulses

In this chapter the experimental results for NSDI of argon and neon are presented. The first part is dedicated to CE-phase effects in energy and emission direction of the particles. That serves as a method to ensure the short duration of the laser pulses inside the main chamber and the working combination between the stereo-ATI and the Reaction Microscope (ReMi). In the second part we investigate the electron correlation patterns for Non-Sequential Double Ionization (NSDI) of argon at an intensity of $1.5 \cdot 10^{14}\,\mathrm{W/cm^2}$ with ultra-short pulses. We interpret the correlation plots in view of results at longer pulse duration and considering the experimental study done in [BKJ$^+$12]and the quantum mechanically model addressing the same set of experimental data [FdMFSN12]. Finally, correlation distributions for NSDI of neon are reported.

4.1 CE-phase effects in single and double ionization

In the chapters 2 and 3, it has been shown that the stereo-ATI spectrometer allows for a phase characterization of the ultra-short laser pulses. Simultaneously, these pulses are used in the ReMi to obtain fully kinematical measurements of NSDI. The pulses are split such that they are identical in both chambers, the ReMi and the stereo-ATI chamber. The working combination is ensured through the investigation of changes in the ions characteristics which are related to the CEP of the laser.

4.1.1 Asymmetries in ion emission directions

CEP dependence of the electron recolliding energy

In section 1.3 it was introduced how the CEP is related to the shape of the electric field and therefore influences the trajectories for the recolliding electron and its returning energy. One observable of this change of energy is the yield the doubly charged ions varying with the CEP [MCLL09, JHW$^+$11, KBJ$^+$12]. Considering a study with ultra-short laser pulses, this is one of the first effect to be investigated because it provides information on the absolute phase of the laser and does not require any calculation of the momentum of the particles. In figure 4.1 the ionization yields for argon (A) and neon (B) are presented. The intensities used are $1.5 \cdot 10^{14}\,\mathrm{W/cm^2}$ and $5.3{\cdot}10^{14}\,\mathrm{W/cm^2}$ for argon and neon, respectively. The energy of the recolliding electron depends on the amplitude of the field (not on the sign) and is π-periodical with the CEP. No clear dependence on the CEP is visible for argon and neon in contrast to the observation in [JHW$^+$11, KBJ$^+$12]. This is mainly because the number of counts is too low to observe any clear modulation of the yield. The pulse duration also influences the observation of the modulation. Using longer pulses

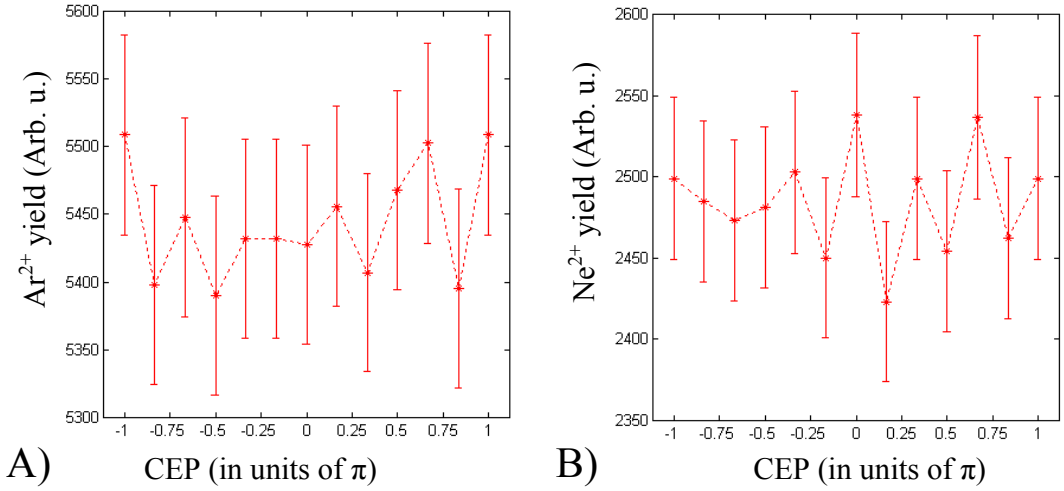

Figure 4.1: Doubly charged ion yield as a function of the CEP for A) argon and B) neon.

decreases the CEP-effects. The pulse length is 6 fs for the yields presented in figure 4.1 against 4 fs reported in [JHW+11].

CEP dependence of the emission direction

The other observable which is influenced by the CEP is the emission direction. In figure 4.2 and 4.3 the longitudinal momentum distribution is shown for respectively the Ar^{2+} and Ne^{2+}. In panel A) the distribution without any selection on the CEP is presented. For both atoms the double hump structure can be recognized attesting for NSDI. Reproducing the observations for both target at longer pulse durations or with ultra-short pulses, the structure is more pronounced and wider in the case of neon. Nonetheless the comparison can not be extended due to the difference in laser intensity for both experiments.

In graphs B-E) a selection on the CEP is made such that the graphs B) and C) are the one where the distribution is the most asymmetric and the graph D) and E) the one where it is the most symmetric. The events are integrated over a window of 0.11 π around the central phase value indicated above each graph. To account for these asymmetries between the right and left peak the asymmetry parameter A is introduced and defined as:

$$A = \frac{N_{\text{right}} - N_{\text{left}}}{N_{\text{right}} + N_{\text{left}}} \tag{4.1}$$

Where N_{right} and N_{left} are the number of particles emitted to the right and left directions respectively[1].

In the graphs F) the asymmetry parameters as a function of the CEP are plotted. As expected from the momentum distributions, a variation of the asymmetry is noticeable which resemble a sine function. This variation confirms the presence of ultra-short laser pulses in the Reaction Microscope. In figure 4.2 and 4.3, from graphs B)-E), it appears that change with the phase is not only a left/right asymmetry. The shape of the peaks changes implying a dependence of the asymmetry on the longitudinal momentum involved. This is particularly visible in graphs D) and E), where the value of the asymmetry is zero but the distributions still look asymmetric (larger peak on one side than the other,especially in the case of argon). Actually if one peak seems to contain less counts, it extends to larger momentum values. Shoulders can be observed around 2.0 a.u. for argon and 4.0 a.u. for neon. The asymmetry distribution as a function of the CEP

[1] depending on the geometry of the experiment it can sometimes be referred equivalently as an up/down asymmetry

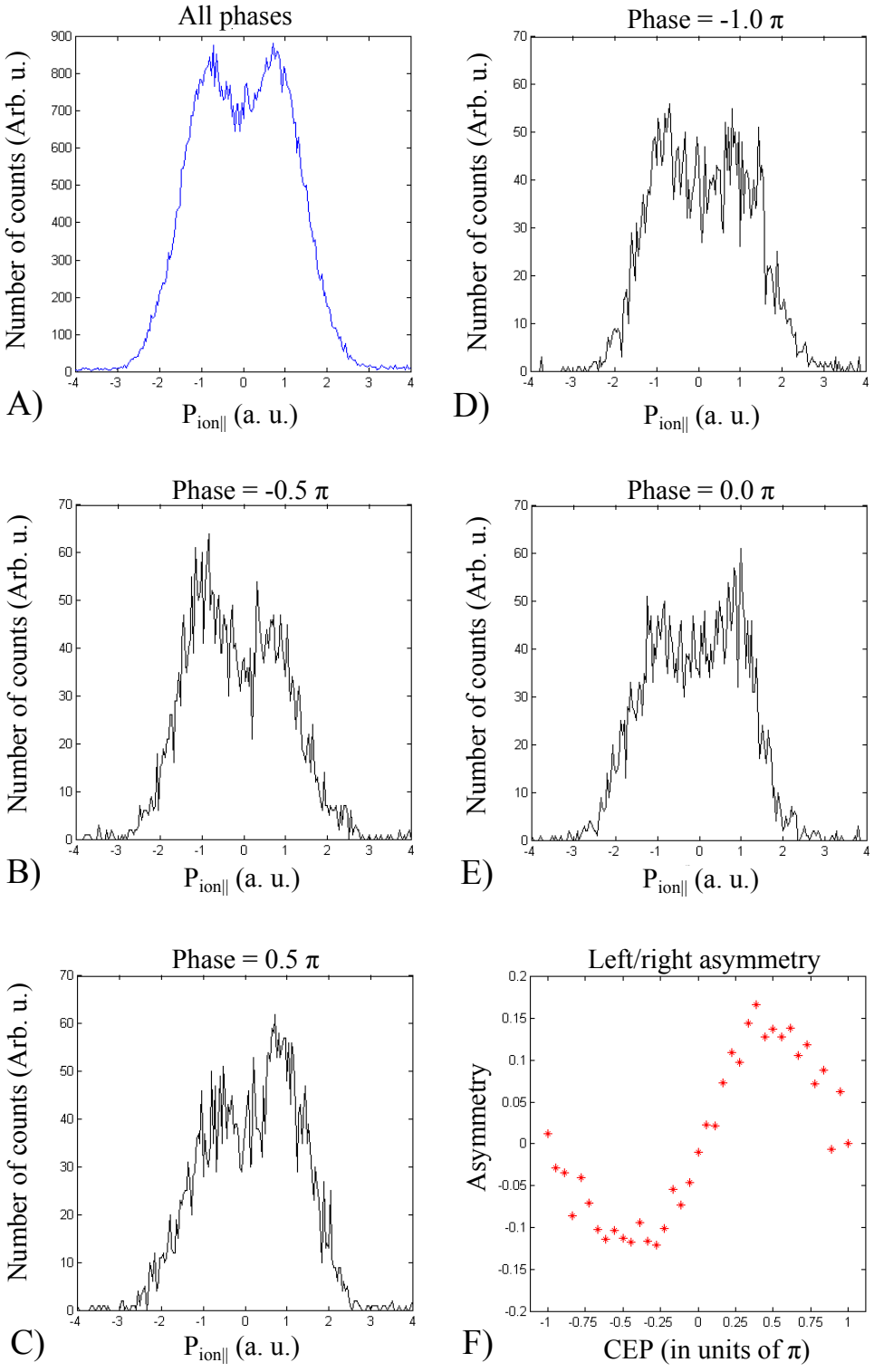

Figure 4.2: Ar^{2+} longitudinal momentum distributions as a function of the CEP for A) no phase selection, B) and C) the two CEP values with maximum asymmetry and D) and E) the two CEP values with no asymmetry. F) Representation of the asymmetry as a function of CEP.

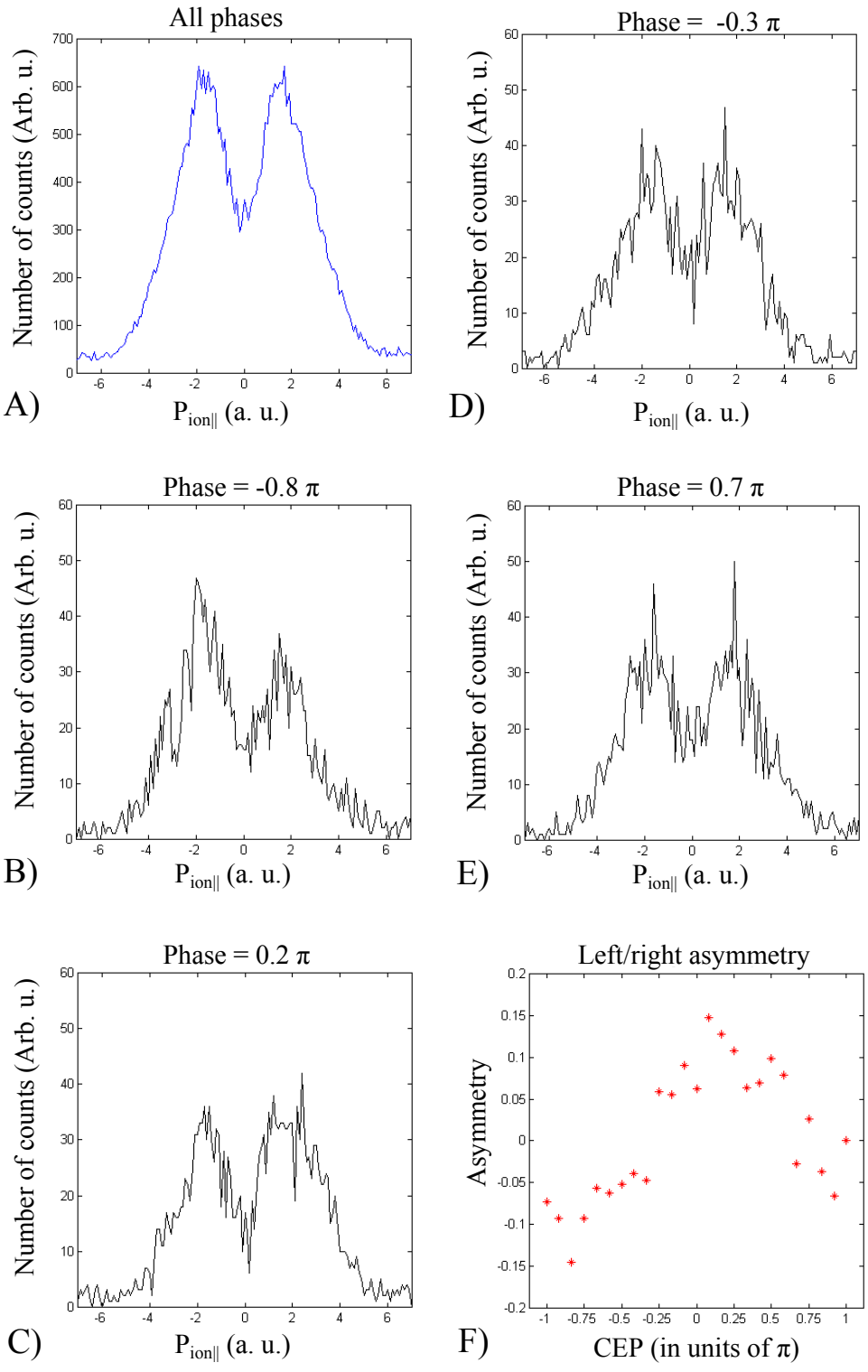

Figure 4.3: Same as figure 4.2 for Ne^{2+}

and the absolute value in longitudinal momentum is shown for the two target species in figure 4.4. As for the stereo-ATI spectrograms obtained for ionization of xenon, the ion asymmetry depends also on the momentum. A tilted part with larger asymmetry values can be observed for larger momentum values: for argon it extends from 1.0 and 2.5 a.u. and for neon between 3.0 and 6.0 a.u. For even larger values, only noise is visible bearing random asymmetry values. Below the tilted area the asymmetry value is less pronounced and seems to be independent of the momentum of the particle.

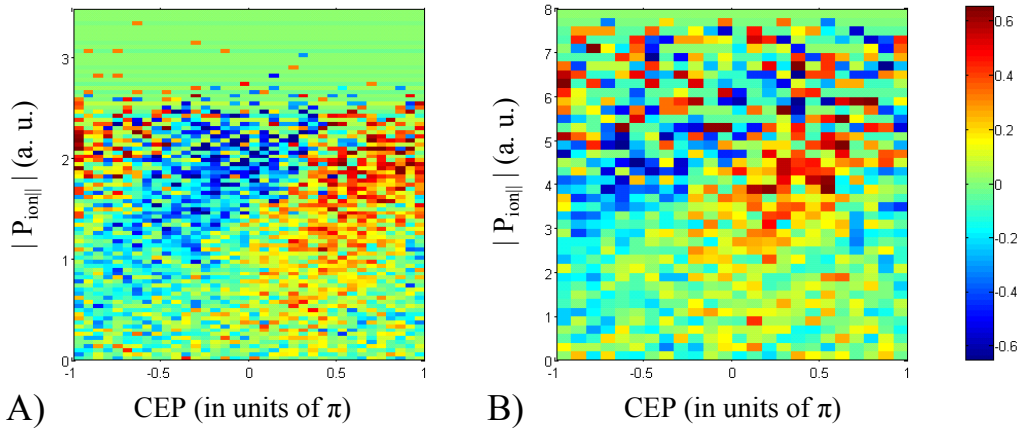

Figure 4.4: Asymmetry of the doubly charged ion as a function of the CEP and the absolute value of the longitudinal momentum A) argon B) neon.

The same analysis is possible with singly charged ions as represented in figure 4.5 for argon (left column) and neon (right column), respectively. Graph 4.5 A) shows the Ar^+ distribution integrated over all CEPs. Noticeable are the peaks/shoulders at ± 0.3, ± 0.5 and ± 0.8 a.u. This are above threshold ionization (ATI) peaks. Their observation is in principle in contradiction with having ultra-short pulses. One explanation could be the presence of a pedestal in the laser pulses that may last for tens of femtoseconds.The neon distribution for all phases in graph 4.5 C) does not possess peaks/shoulders. It can signify that the pulses were shorter, without pedestal. However, because for neon the ionization potential is higher, requiring a higher laser intensity (in the present case $5.3 \cdot 10^{14}\,\mathrm{W/cm^2}$), the tunnel ionization process is considered as the proper picture. In that regime, even though the ATI peaks are still present (cf [RZS+04]) they are less pronounced. The asymmetry as a function of the CEP are shown in panels B) and D), they are much less pronounced than in the case of doubly charged ions and reach barely 5 %.

For single ionization the amplitude of the asymmetry is lower than for the doubly charged ions. The main mechanism generating Ar^+ and Ne^+ does not depend on the recollision. The electrons are ionized through "direct" ionization and leave the core without rescattering. Nevertheless there are still CEP effects visible. The atoms are ionized by the asymmetric electric field. This introduces an asymmetry. After ionization, the electron trajectory in the field depends on the CEP and so the final electron momentum is CE-dependent (cf equation 1.14 and 1.15). Some of the electrons, in particular the ones with high energies (more than $2\,U_p$) experience rescattering on the ionic core. They present more dependence on the CEP as can be seen in figure 4.6. Figure 4.6 shows the asymmetry of the ions as a function of the CEP and of the absolute value of their longitudinal momentum. Two distinct areas can be seen: an area with low value of asymmetry (less than 1.5 a.u for argon and 2.4 a.u for neon) for direct photo-electrons and the area with higher value of asymmetry for rescattering electrons. The absolute value of asymmetry is larger for these electrons. It is at a value of 0.2 for the rescattering electrons and for the direct electrons, especially close to zero momentum where the maximum counts are, it does not exceed 0.1.

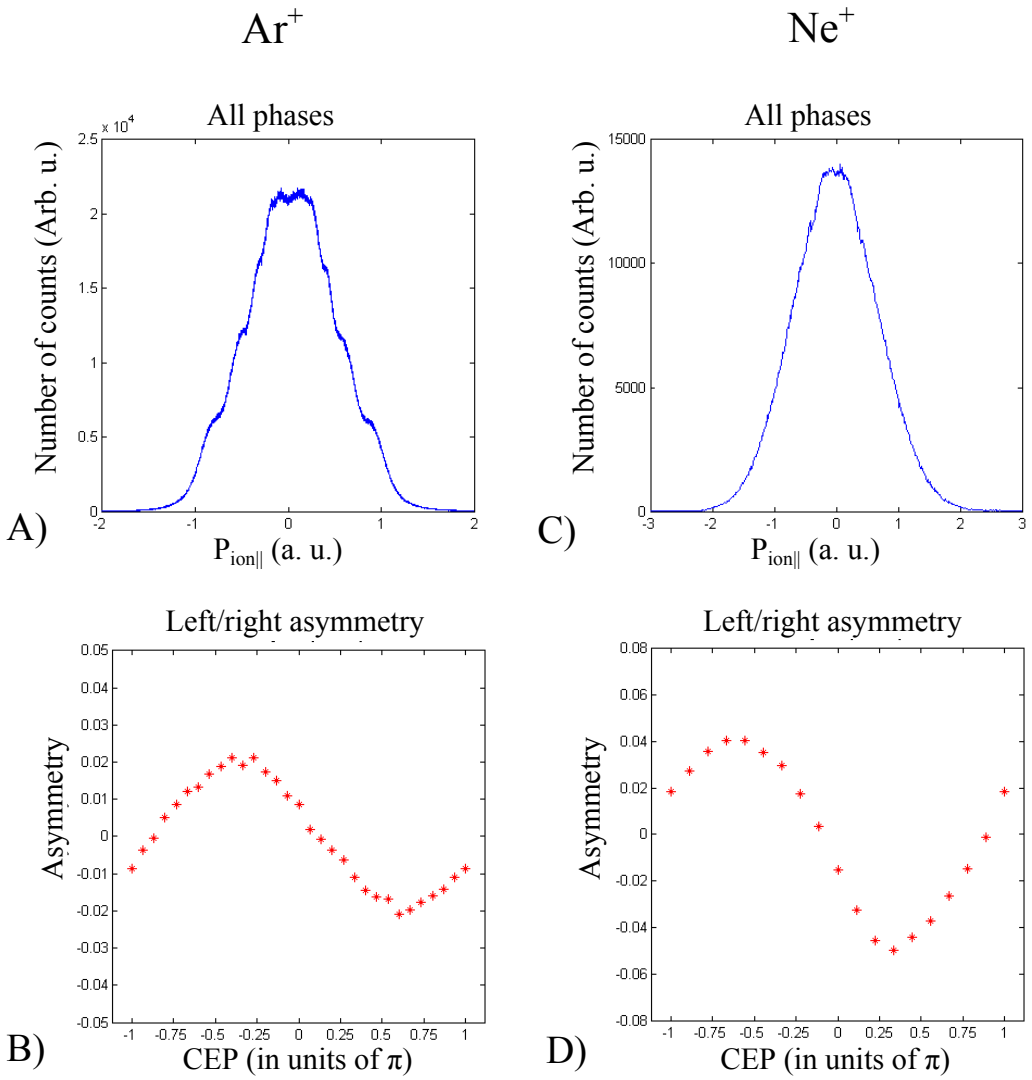

Figure 4.5: A) Ar^+ longitudinal momentum distribution without any phase selection. B) Representation of the asymmetry in Ar^+ as a function of CEP. C) Ne^+ longitudinal momentum distribution without any phase selection. D) Representation of the asymmetry in Ne^+ as a function of CEP.

This area has also a different CEP dependence with a tilted part. It stops respectively at 2.2 a.u and 3.3 a.u. for argon and neon. At larger momentum only noise is present.

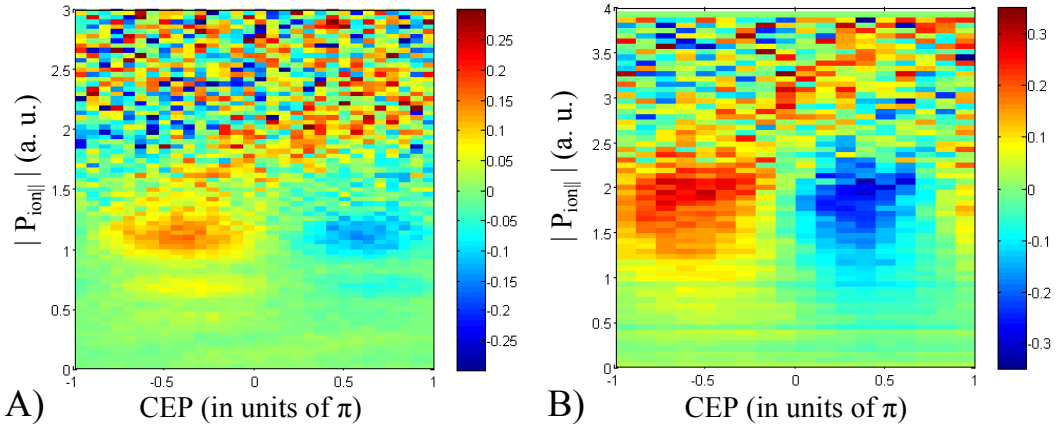

Figure 4.6: Asymmetry in the singly charged ion as a function of the CEP and the absolute value of the longitudinal momentum for A) argon B) neon.

It is necessary to mention that the asymmetry distributions depend strongly on the laser parameters. For instance, in the section 2.3 is reported how such a spectrogram (for the ionization of xenon) changes with the power of the laser beam. Another example is given in [APJ+09] where a change of the chirp of the laser (third order dispersion) proved to influence the pattern for all momenta. Several comparisons with different theoretical models have been made corresponding to the experimental observations [PLW+03, MPBB06, Hof09] but without extracting, as of the present status, sensible information on the characteristics of the laser pulse.

4.2 Electron correlation for argon double ionization

The occurrence of an asymmetry in the singly and doubly charged ions is of great importance to ensure the presence of ultra-short laser pulses in the ReMi. Nevertheless, this aspect has already been investigated experimentally. It has limitations concerning the extraction of dynamical information about the NSDI simply because three particles are involved whereas one is detected. In this section the electron correlation plots obtained for argon is reported. Due to the similarity with the experimental data present in [BKJ+12] we will restrict the interpretation to the elements developed in this article and the theoretical analysis made consecutively in [FdMFSN12]. Later, in chapter 5, a model to interpret the correlation plot for NSDI at lower intensity will be presented.

4.2.1 Experimental results

The correlation pattern obtained for argon is shown in figure 4.7. The graph integrated over all phases is displayed in the top-left corner. The correlation plot at a phase where no asymmetry is visible is displayed in the bottom-left, and in the right column, the data for the two phases with the maximum asymmetric distribution are shown (these three graphs are average over a phase window of 0.22π). For comparison of the distribution with selected phase, the color scale is similar. A slight asymmetry can be seen with the distribution moving along the $p_{e1||} = p_{e2||}$ diagonal. The population of the distribution is mainly located on the x and y-axis.

The structure is in striking contrast with the previous studies of NSDI of argon. A comparison is made in figure 4.8. Figure 4.8 A) is a reproduction of figure 4.7 A). The momentum scale has been extended to compare with other results. Figure 4.8 C) represents the correlation plot for NSDI of argon with long pulses (35 fs) at the intensity of $1.5 \cdot 10^{14}\,\mathrm{W/cm^2}$ similar to the intensity of the correlation plot obtained with ultra-short pulses (graph A). Graphs B) and D)

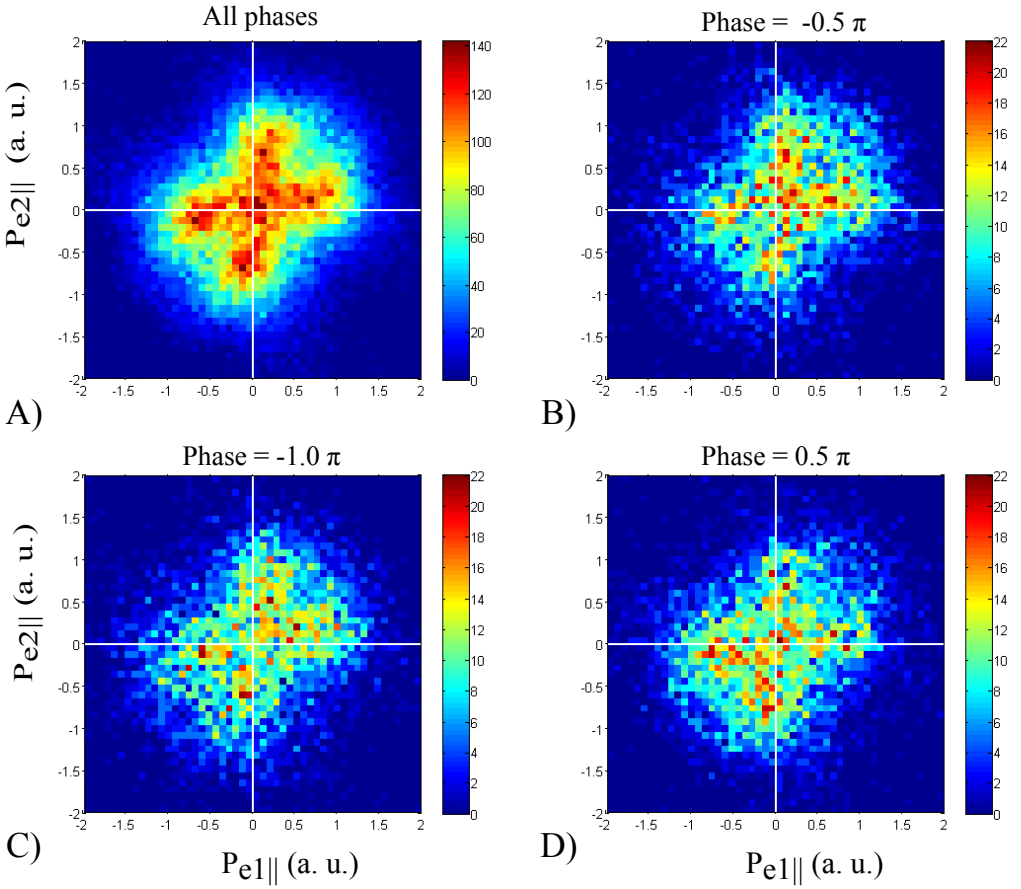

Figure 4.7: Correlation plot for argon with different CEP selections. A) No phase selection .B) CEP showing no asymmetry. C) and D) The two CEP values with maximum asymmetry.

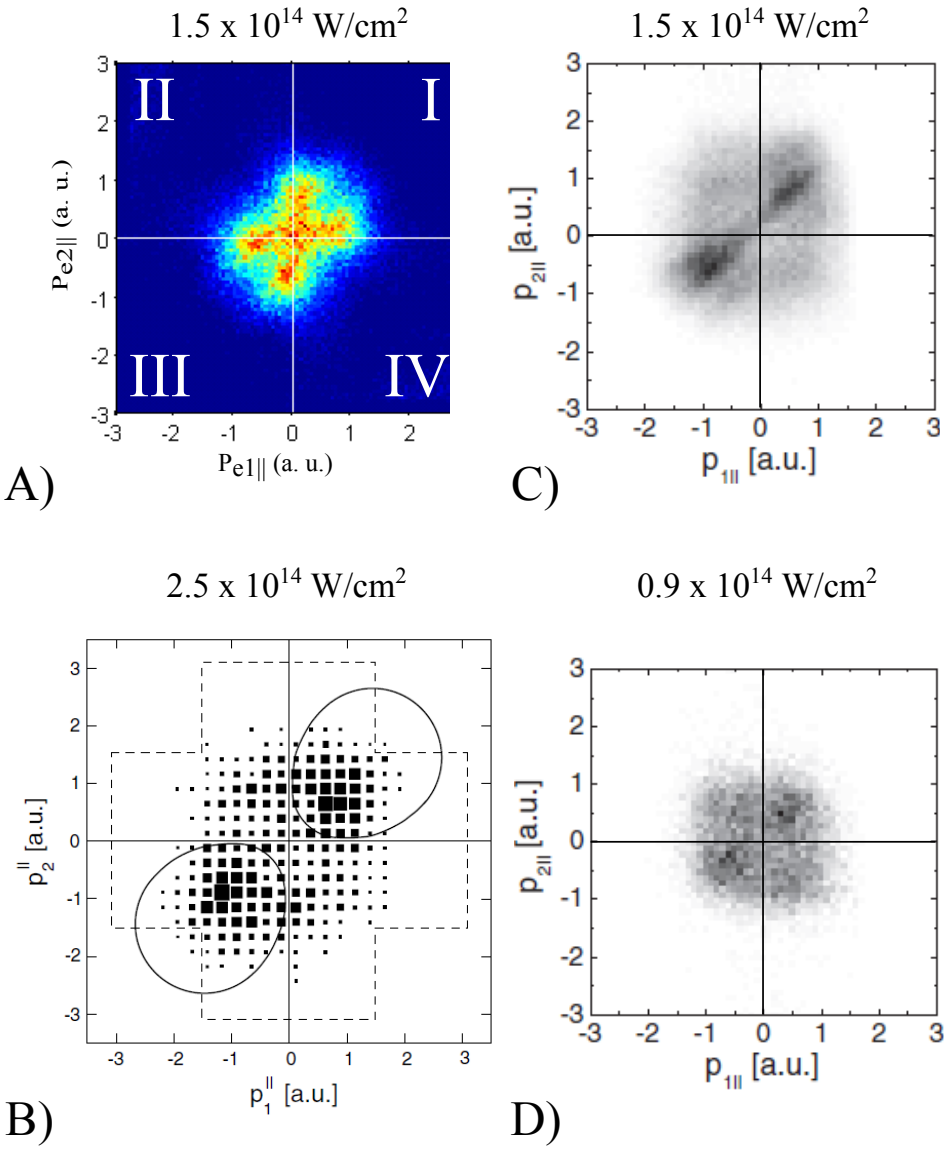

Figure 4.8: Correlation plot for NSDI of argon. A) Obtained with 6 fs laser pulses and an intensity of $1.5{\cdot}10^{14}$ W/cm^2, same as shown in figure 4.7A). The label of the four quadrants are indicated. B) Obtained with 25 fs laser pulses and an intensity of $2.5 \cdot 10^{14}$ W/cm^2 The delimited areas represent the kinematical constraints on the correlation plot from the (e,2e)-like process (solid thick line) and the RESI process (dashed line). C) Obtained with 35 fs laser pulses and an intensity of $1.5 \cdot 10^{14}$ W/cm^2. D) Obtained with 35 fs laser pulses and an intensity of $0.9 \cdot 10^{14}$ W/cm^2. Graph B) is taken from [FMF$^+$01] and graphs C) and D) are taken from [ELR$^+$03].

are also correlation plot of NSDI of argon with long pulses but with slightly different intensities respectively $0.9 \cdot 10^{14}\,\mathrm{W/cm^2}$ and $2.5 \cdot 10^{14}\,\mathrm{W/cm^2}$. A clear difference is obtained by reducing the pulse duration: although the structure for short pulses (graph A) is located mainly on the axes, the correlation plot for longer pulses (B,C and D) is located mainly on the diagonals ($p_{e1||} = p_{e2||}$ and $p_{e1||} = -p_{e2||}$) and is depleted in the center. For the graphs at long pulse duration, the population of the four different quadrants has been interpreted involving different NSDI mechanisms. The events close to the $p_{e1||} = p_{e2||}$ diagonal are due to (e,2e)-like ionization. The bound electron is ionized at the moment of impact. From recollision, both electrons acquire the same momentum from the laser field and therefore have a close momentum value. In contrast, it is assumed that the RESI mechanism do not favor any quadrant. The ion is excited upon recollision and the bound electron is ionized independently in the laser field. Depending on this second time of ionization (happening one, two, three, ... half-cycles after the recollision) the second electron is emitted in the same direction than the first electron or opposite to it and the corresponding event populates quadrants I and III or quadrants II and IV, respectively.

This argument is confirmed by the change in the relative population of the four quadrants with a change of intensity. When decreasing the intensity of the laser (from the correlation plot of panel B) to the one of panel D)) the quadrants II and IV are more populated (or alternatively, the quadrants I and III are less populated). Since a decrease of intensity induces a decrease of the recolliding energy of the electron and favors the excitation of the ion upon its direct ionization, quadrants II and IV are populated by mechanism requiring less energetic electron namely multiple recollisions and RESI. This infers that the events close to the $p_{e1||} = p_{e2||}$ diagonal are due to (e,2e). However another experimental argument has to be included: it concerns the energy the recolliding electron has. At an intensity of $1.5 \cdot 10^{14}\,\mathrm{W/cm^2}$ (graphs A and C), this maximum kinetic energy is 1.0 a.u. and is sufficient to ionize the argon ion on the impact ($\mathrm{I}_{p2}^{argon} = -1.0\,\mathrm{a.u.}$). However, for an intensity of $0.9 \cdot 10^{14}\,\mathrm{W/cm^2}$ (graph D), we are in the "below threshold" regime where the maximum returning energy is 0.6 a.u., too low to ionize the bound electron on the impact. In principle, no features observed on the correlation plot at this low intensity is originating from (e,2e)-like ionization.

On the theory side, calculations using semi-classical model for NSDI of argon [YL10, TZLY11] have shown that the events populating the $p_{e1||} = p_{e2||}$ diagonal are produced through (e,2e) mechanism, even in the below threshold regime. The explanation for the (e,2e) mechanism in the low intensity regime being that the Coulomb barrier for the bound electron is lowered by the laser field requiring less than 1.0 a.u. of energy for impact ionization.

This questioning of the mechanism involved for a given feature in the pattern is of importance. A mechanism such as (e,2e)-like ionization should not be affected by the pulse duration since its entire dynamics is confined on a single cycle. The dependence on the pulse duration therefore reveals information on the mechanism at both pulse durations. The features interpreted as originating from (e,2e) in NSDI of argon should be present with ultra-short pulses but in the present case, results differ strongly.

Although the results presented in figure 4.7 appear unexpected, they are confirmed by an experiment on NSDI of argon realized with a different laser system and spectrometer at a similar laser intensity of $1.5 \cdot 10^{14}\,\mathrm{W/cm^2}$. This experiment has been performed in the frame of a collaboration between our division and the people working under the supervision of Mathias Kling at the Max-Planck-Institut für Quantenoptik in Garching. The advantage was the possibility to use shorter pulses (less than 4 fs). The drawback was the momentum resolution of the spectrometer in Garching lower than for the Heidelberg ReMi. These results are published in [BKJ+12].

These Garching results are shown in figure 4.9 for all CEP (A) and selected phases (B). In that case the correlation pattern is referred to as a "cross-shaped" structure.

For both experimental results, the correlation plot integrated over all CEP are very similar (figures 4.7 A) and 4.9 A)) the distribution of figure 4.9 A) also forms two branches very close to the axis, perpendicular to each other. The widths of the two distributions are similar reflecting the similar intensity used. Due to the "near-single cycle" pulses used in the Garching experiment having a duration of 3.8 fs, the changes on the distribution with the CEP (figure 4.9 B)) are larger

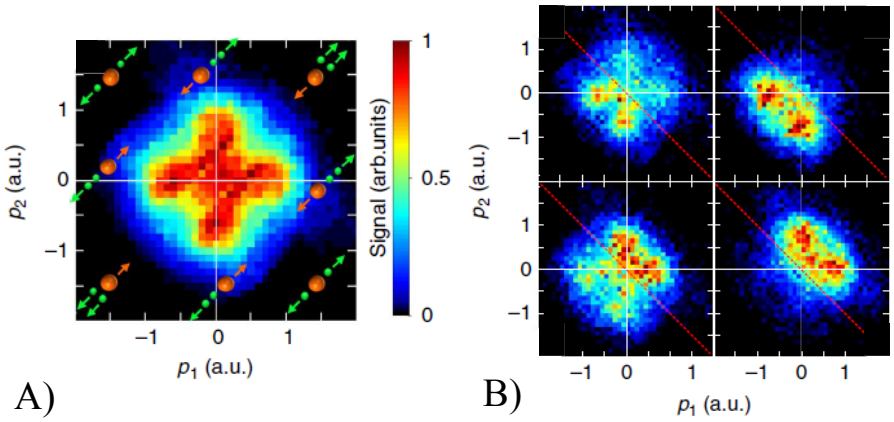

Figure 4.9: A) Correlation plot for argon NSDI with a 3.8 fs laser pulses and intensity of $1.5 \cdot 10^{14}$W/cm^2. B) Correlation plot for selected CEP (top left: -0.64 π; top right: -0.14 π; bottom left: 0.36 π; bottom right: 0.86 π). A red diagonal is added corresponding to zero Ar^{2+} longitudinal momentum. Pictures adapted from [BKJ+12].

than the changes observed in figure 4.7. The reported asymmetry in Ar^{2+} emission direction is 60 % for the garching experiment while 25 % for a duration of 6 fs.

In order to interpret the cross-shaped structures two approaches have been proposed and will be discussed in the following.

4.2.2 Comparison with semi-classical model

The first approach is the semi-classical model developed in [BKJ+12]. Along the laser field E(t) the ionization is described by the tunneling rate (ADK formula modified according to [TL05] to account for above the barrier ionization).
At the moment of tunneling, t_0, the electron has zero momentum and is positioned at $z_0 = z_t$, where z_t is the exit of the tunnel, fulfilling the condition $-I_p = -z_t E(t_0) + V_i(z_t)$. V_i is the Coulomb potential of the singly charged ion felt by the electron $\frac{-1}{|x_t|}$. The electron propagates classically in the electric field without considering the potential of the ion. Two calculations are performed after recollision depending on what happens during this recollision. For the (e,2e)-like process, a second electron is ionized only if the kinetic energy of the returning electron is higher than the second ionization potential of argon ($I_p = 27.5$ eV). At the moment of recollision, the momentum of the first electron after tunneling is calculated via energy conservation and the second electron has zero momentum. For the RESI case, the excited state which can be populated is the lowest excited state of Ar^+: $3s3p^6$ situated at 13.5 eV above the ground state. If the returning electron has an energy higher than this value, this states is populated. The probability of ionizing excited Ar^+ later in the electric field follows the same ionization rate than described for the first ionization and the ionized electron has the same characteristics (position and velocity) than described in the first ionization step. For the returning electron, its momentum value is decreased, in absolute value by the energy necessary to excite Ar^+. In both cases, a scattering angle β between the momentum vectors of the returning electron before and after collision is defined as fitting parameter. For example a large angle β means that a large part of the momentum present in the longitudinal direction of the recolliding electron will be transferred to its transverse momentum component after recollision.

The first information concerns the predominance of (e,2e) or RESI mechanism. Figure 4.10 represents correlation plot for the different mechanisms. The (e,2e) distribution (A) is wider than

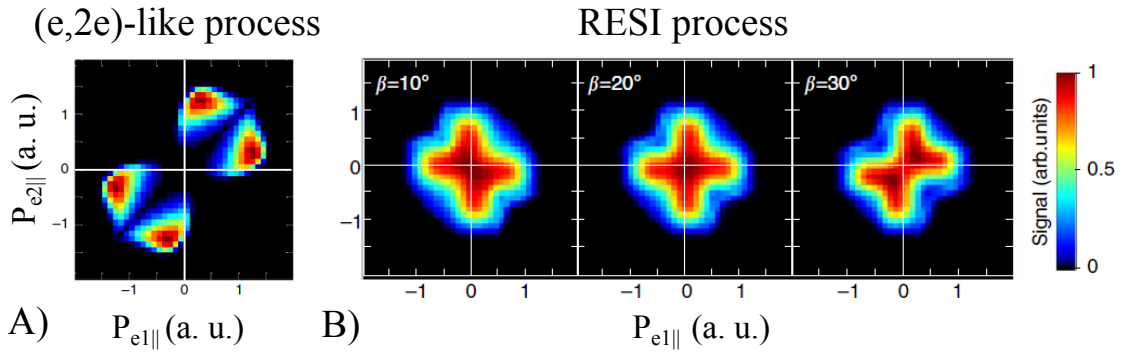

Figure 4.10: Theoretical correlation plots obtained considering different mechanisms. A) (e,2e)-like ionization. The β scattering parameter is equal to zero, the value best fitting to the experimental data. B) the RESI of the second electron for different β parameters is considered. Pictures taken from [BKJ+12].

the RESI one (B). This follows from the kinematical constraints addressed in section 1.2.2. In the model, the final momentum of the bound electron is equal to the vector potential A(t) at the moment of ionization. This vector potential A(t) is larger at the moment of recollision, close to E(t)=0, than close to a peak of the laser field, time where ionization happens in RESI mechanism. The shape obtained from the (e,2e) mechanism is quite different from the experimental data presented in figure 4.7 and 4.9. The pattern is not distributed in the center of the graph and the distribution is closer to the $p_{e1||} = p_{e2||}$ diagonal than in the experimental correlation plots.

In contrast, the RESI mechanism leads to theoretical distributions closer to the experimental ones. The correlation plots for this mechanism are shown in figure 4.10 B) for different β parameters. Independently of β, the events are close to the X and Y axis and are located at the center of the graph. The β parameter is a "transfer" of momentum from the longitudinal to the transverse component for the recolliding electron. Effectively, since only the longitudinal component is considered, this can be seen as a scaling parameter for the energy of the first electron (being multiplied by $\cos^2(\beta)$). The best fit to the experimental data is obtained with a value of $\beta = 20°$.

Although experimentally no distinction can be made between the two electrons (the reason of symmetrizing the correlation plots), it is found theoretically that the recolliding electron is the one with a momentum close to zero. The secondly ionized electron is the one which can obtain larger momentum. Its final momentum value is equal to $-A(t_2)$, with t_2 its ionization time. The position of the distribution on the axes serves as a cursor to determine the most probable time t_2 of ionization. This time is found to be 210 attoseconds before the maximum of the peak associated with an early depletion of the excited state. It must be pointed out that choosing the angle β seems arbitrary. Nonetheless, defining β as a parameter helps to point out that the exchange of the recolliding energy is more diverse than simply exciting the bound electron to a given state. This study emphasizes the role of the tunneling of the second electron.

For consistency, it has to be mentioned that the study presented in [FdMFSN12] is also based on the experimental observation of the cross-shaped structure but with a slightly different conclusion.

4.2.3 Comparison with quantum mechanical model

The quantum mechanical model applied to RESI is found in [FdMFSN12] (cf. section 1.2, equation 1.12). For each final momentum value (p_1, p_2) the transition amplitude $M(\mathbf{p}_1, \mathbf{p}_2)$ to this electronic configuration is calculated using the strong field approximation. The transition amplitude reads:

$$M(\mathbf{p}_1, \mathbf{p}_2) = \int_{-\infty}^{\infty} dt \int_{-\infty}^{t} dt' \int_{-\infty}^{t'} dt'' \int d^3k \times V_{\mathbf{p}_2 e} V_{\mathbf{p}_1 e, kg} V_{kg} \exp(iS(\mathbf{p}_1, \mathbf{p}_2, \mathbf{k}, t, t', t'')) \quad (4.2)$$

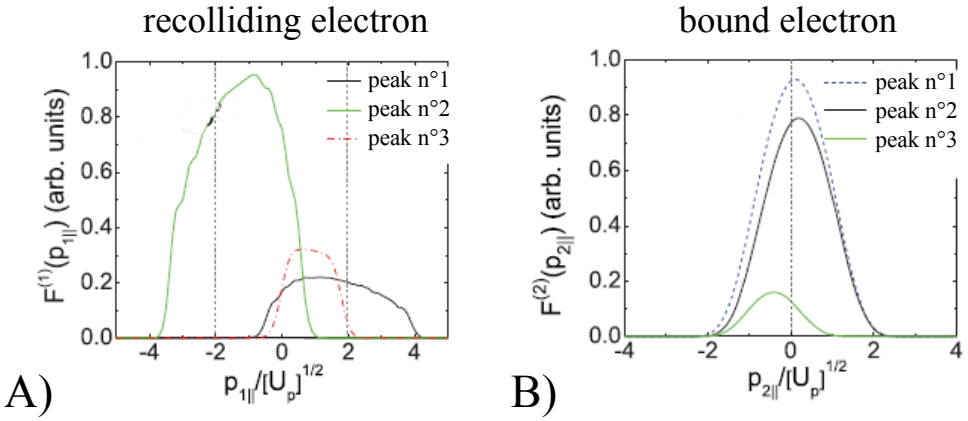

Figure 4.11: Theoretical momentum distributions for (A) the first electron and (B) the second electron. Different ionization times of the first electron are considered (ionized in the peak n°1, 2 or 3). Pictures taken from [FdMFSN12].

(equation 1.12 where the expressions of the time-evolution operators are implemented)
$S(\mathbf{p}_1, \mathbf{p}_2, \mathbf{k}, t, t', t'')$ gives the semi-classical action of the system and V_{kg}, $V_{\mathbf{p}_1 e,kg}$ and $V_{\mathbf{p}_2 e}$ are the form factors of the ionization of the first electron, recollision of the second electron with excitation of the second and tunnel ionization of the second electron, respectively.

The analysis focuses on the recollision trajectories: which trajectories contribute predominantly at a given CEP value and to which momentum distribution does it lead? The momentum distributions of each electron (recolliding and bound) are investigated. Figure 4.11 shows for a given CEP value the momentum distributions of the returning electron A) and the second ionized one B). For each graph the distribution is plotted for three different first times of ionization, when this ionization happens in the laser peak n°1, 2 or 3. These three laser peaks are the ones contributing the more to the total yield at this CEP value. The intensity of the laser is $3 \cdot 10^{14}\,\mathrm{W/cm^2}$.

For each electron, the difference between the distribution from different ionization times can be explained by the asymmetry of the electric field. The difference in distribution amplitude comes from the different amplitudes of the electric field peaks. Also, depending on the moment of ionization the electron acquires positive or negative momentum and the distribution is more localized on the left or the right. What is more important is the difference between the distributions shape of the two electrons. For the bound electron all distributions are centered close to zero and do not spread more than $2\,\mathrm{U}_p^{1/2}$. For the distributions of the recolliding electrons the maximum is further away from zero and the distributions can extends up to $4\,\mathrm{U}_p^{1/2}$. The fact that the recolliding electron is the one with large final momentum value (and therefore the second electron has always small values) is present for all CEPs (cf figures 3 and 4 in [FdMFSN12]) and is in contradiction with the studies of [BKJ+12].

The reasons for the second electron being the one with small momentum values follow the kinematical constraints. The maximum probability for tunnel ionization of the second electron is at a maximum of the electric field where the vector potential value is close to zero. Concerning the other electron just after recollision, its energy E_{exc} is defined by $E_{\mathrm{exc}} = E_{\mathrm{rec}} - E_{\mathrm{excit2}}$, where E_{rec} is it returning energy and E_{excit2} is the energy needed to excite the bound electron. For one given excitation energy (one transition considered) the final momentum of the recolliding electron is in the interval $[(-A(t_{\mathrm{rec}}) - \sqrt{(2E_{\mathrm{exc}})})\ ,\ (-A(t_{\mathrm{rec}}) + \sqrt{2E_{\mathrm{exc}}})]$. $-A(t_{\mathrm{rec}})$ is the momentum the electron acquires from the laser after the moment of recollision (equal to $2\,\mathrm{U}_p^{1/2}$ for a monochromatic field where the recollision is at the zero crossing). In the case of ultra-short laser pulses, this value depends on the given electric field and trajectories [SFdMFS12]. Overlapping contributions from the different E_{excit2} lead to the maximum value for $p_{1||}$ centered at $-A(t_{\mathrm{rec}})$.

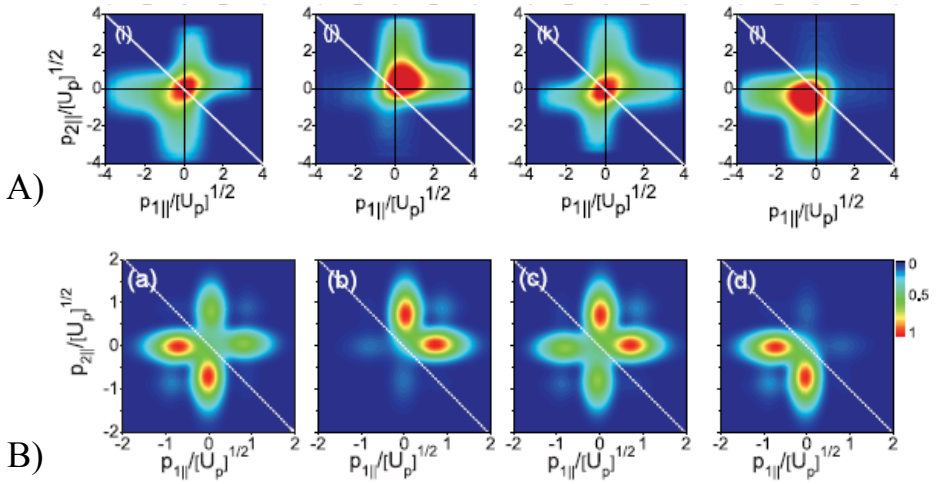

Figure 4.12: Theoretical correlation plots obtained for different CEPs for an intensity of A) $3 \cdot 10^{14}\,\mathrm{W/cm^2}$ and B) $1.5 \cdot 10^{14}\,\mathrm{W/cm^2}$. CEP from left to right: -0.64, -0.14, 0.36 and $0.86\,\pi$. Note the different momentum scales. Picture taken from [FdMFSN12].

The correlation plots calculated for different CEP for an intensity of $3 \cdot 10^{14}\,\mathrm{W/cm^2}$ is represented in figure 4.12 A). For a given ionization time of the first electron only the events where the bound electron is ionized in the peak one cycle later are taken. At this intensity (A) the pattern is located in the center and does not "extend" along the $p_{n||}$ axes. When decreasing the intensity to $1.5 \cdot 10^{14}\,\mathrm{W/cm^2}$ (figure 4.12 B)), the pattern resembles strongly the observed experimental correlation distributions. The only discrepancy is the distribution depleted in the center. The change of shape is due to E_{exc} decreasing in value and thus decreasing the range of the interval $[(-A(t_{\mathrm{rec}}) - \sqrt{(2E_{\mathrm{exc}})}) \quad (-A(t_{\mathrm{rec}}) + \sqrt{2E_{\mathrm{exc}}})]$ for the distribution of $p_{1||}$. The two maxima $\pm(-A(t_{\mathrm{rec}})$ can be differentiated and the center of the graph is depleted.

A limitation pointed out by the authors of [FdMFSN12] are the excited states included for the second electron. The transitions are $3p \rightarrow 4s$ and $3p \rightarrow 4s$ (in the semi-classical model $3s \rightarrow 3p$). Introducing higher energy state as proposed by the authors is likely to change the momentum distribution around the maxima at $\pm(-A(t_{\mathrm{rec}})$ and therefore the overall 2D distribution. From this study a different conclusion is drawn on the "decisive observable" in the model since the momentum distribution of the recolliding electron is the one effectively affected by CEP.

The experimental data for NSDI of argon at an intensity of $1.5 \cdot 10^{14}\,\mathrm{W/cm^2}$ indicates the involvement of the RESI mechanism. If an ambiguity remains in the interpretation of the process (which states involved, which electron has a small momentum value) the structures observed for longer pulses durations on the diagonal $p_{1||} = p_{2||}$ can be ruled out. This different observations most likely find their origin in the suppression of the multiple recollisions with ultra-short laser pulses. This relates the structure on the diagonal observed for argon with multiple recollisions and is in contradiction with theoretical predictions [YLL08, YL10] relating them to single recollisions.

In order to investigate the influence of these multiple recollisions we look at the neon correlation plot. In neon, the transition through an excited state after recollision has been found negligible [LYL$^+$10]. This has been deduced partly from the high energy of the first excited levels and partly from the low cross-section for excitation in comparison to ionization (figure 1.8). Therefore the NSDI of neon was identified as emanating from single recollision (without RESI or multiple recollisions). This target offers a test to observe if the change in electron correlation for NSDI of argon is reproducible for neon and intrinsic to the use of ultra-short laser pulses. Or if this change is specific for argon, involving the origin of the structure on the diagonal in argon for

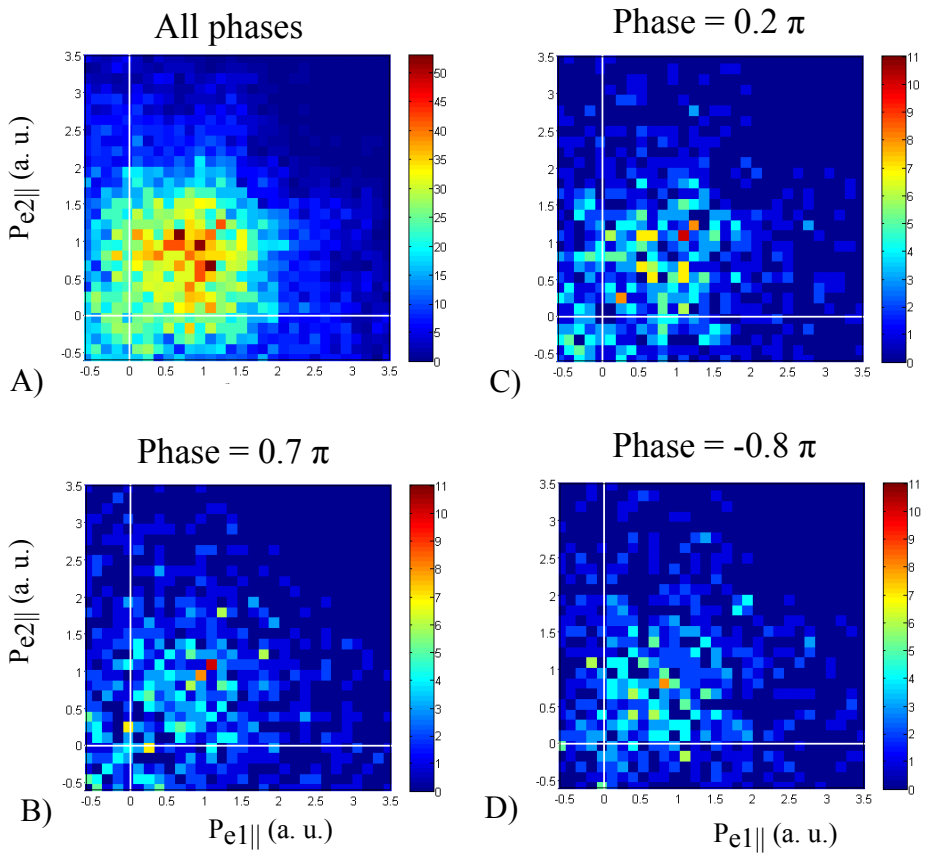

Figure 4.13: Correlation plot for Neon with different CEP characteristics. A) No phase selection is applied. B) Phase where no asymmetry is present. C) and D) the two CEP values with maximum asymmetry, the more and less counts in quadrant I respectively.

longer pulse durations to another mechanism than the (e,2e)-like process. The intensity used for the ionization of neon is $5.3 \cdot 10^{14}\,\mathrm{W/cm^2}$. The ponderomotive energy is 1.05 a.u.=0.70 I_{p2}^{neon}, with I_{p2}^{neon} the second ionization potential of neon. For NSDI of argon the ponderomotive energy of the $1.5 \cdot 10^{14}\,\mathrm{W/cm^2}$ intense laser was equal to 0.3 I_{p2}^{argon}, the two realizations are not completely comparable.

4.3 Electron correlation for neon double ionization

4.3.1 Experimental results

In this section the measured correlation plots as a function of the CEP for neon NSDI are presented. Prior to the correlation graphs, a comment has to be made on the detection of electrons for that experiment. Due to technical issues, not all the events are viable. Only electrons with a momentum superior to -0.6 a.u are taken for the investigation of correlations.

The correlation plots for neon are shown in figure 4.13. Panel A) represents the distribution integrated over all phases, panel B) where no asymmetry is present and panel C) and D) with maximum asymmetry value. Due to the low number of events, it is rather unlikely to extract some information for single phases. However the phase integrated graph can be interpreted in comparison with previous results on argon and results on neon at longer pulses duration.

The distribution is considerably different from what has been observed for NSDI of argon with ultra-short laser pulses. The maximum of the distribution is close to the $p_{e1||} = p_{e2||}$ diagonal and few events are close to (0,0), (but this can already be expected from the Ne^{2+} longitudinal distribution 4.3 showing a pronounced valley at zero). These would be in disfavor of having the RESI mechanism as an intermediate state at the recollision. In fact, the distribution resembles the neon correlation plot obtained at longer pulses experimentally ([MUF$^+$03, WZS$^+$04, LYL$^+$10]) but also from calculations [FdMFSLB04, LFdMF04] (cf. figure 1.6). Already pointed out was the very low probability for neon ions to pass through an intermediate excited state (cf section 1.2.1) and therefore the strong influence of the (e,2e)-mechanism at longer pulse durations. In the assumption that the strong resemblance originates from the same mechanism, this is a confirmation of the impact direct ionization with ultra-short laser pulses. The pattern outlines that the argon correlation plot at an intensity of $1.5 \cdot 10^{14}\,\mathrm{W/cm^2}$ is not issued from (e,2e)-like ionization and that a mechanism of multiple recollisions plays an important role for argon NSDI at longer pulse durations.

Chapter 5

Double ionization of argon at below threshold intensity

In this chapter the results for NSDI of argon are presented but for a substantially lower intensity than the results discussed in chapter 4. At this intensity ($0.9 \cdot 10^{14}$ W.cm^2) the electron recolliding energy has a maximum value of 0.63 a.u. This is to be compared with the 1.01 a.u. energy of the bound electron. A semi-classical model is developed in order to reproduce and interpret the experimental results. The preferential channel for NSDI is identified as passing through the formation of a doubly excited state. We look at properties of this doubly excited atom related to the electron momentum distribution and show that a close relation between the two electrons momentum difference and the difference in ionization times can be extracted. We examine this relation through a model representing the classical evolution of a doubly excited state in a laser field. In the first part, the experimental results for NSDI below threshold intensity are presented. In the second part, the theoretical model is developed and the physical information extracted from it is discussed, especially the pathway through a doubly excited state.

5.1 CE-phase effects at low intensity

5.1.1 Asymmetry in the ion longitudinal momentum

In this section the experimental results for NSDI of Argon at $0.9 \cdot 10^{14}$ W/cm^2 are presented. The CE-phase calibration procedure is the same than introduced in section 2.3.4 in order to have a homogeneous phase distribution and to compensate for drifts of the phase over the measurement duration. Figure 5.1 shows for Ar^+ and Ar^{2+} the longitudinal momentum plot of the ion (first row), the asymmetry as a function of the longitudinal momentum (second row) and the integrated asymmetry over the full momentum range (third row).

The first observation which can be made concerns the width of the momentum distributions in panels A) and D) in comparison to argon NSDI results presented in chapter 4. This change is due to a different intensity of the laser, $0.9 \cdot 10^{14}$ W/cm^2 in the present case against $1.5 \cdot 10^{14}$ W/cm^2 for the results of chapter 4. With a less intense electric field, the momentum the particles acquire is lower and so is the distribution width. The full width at half maximum was 1.2 and 2.9 a.u. for Ar^+ and Ar^{2+} respectively at higher intensity while for this intensity the values are 1.0 and 2.7 a.u.

The shape of the Ar^{2+} distribution is also changed. It no longer resembles a double peak structure but is best described by a plateau from -1.0 to 1.0 a.u. Two interpretations can be made to explain this change. The first one concerns the distance between the two peaks/humps of the distribution. The position of the peaks varies with the recollision energy of the electrons (cf section 1.2.1). For a lower returning energy, the distance decreases until the two peaks form effectively a plateau. The second interpretation is that a different ionization channel is present leading to a

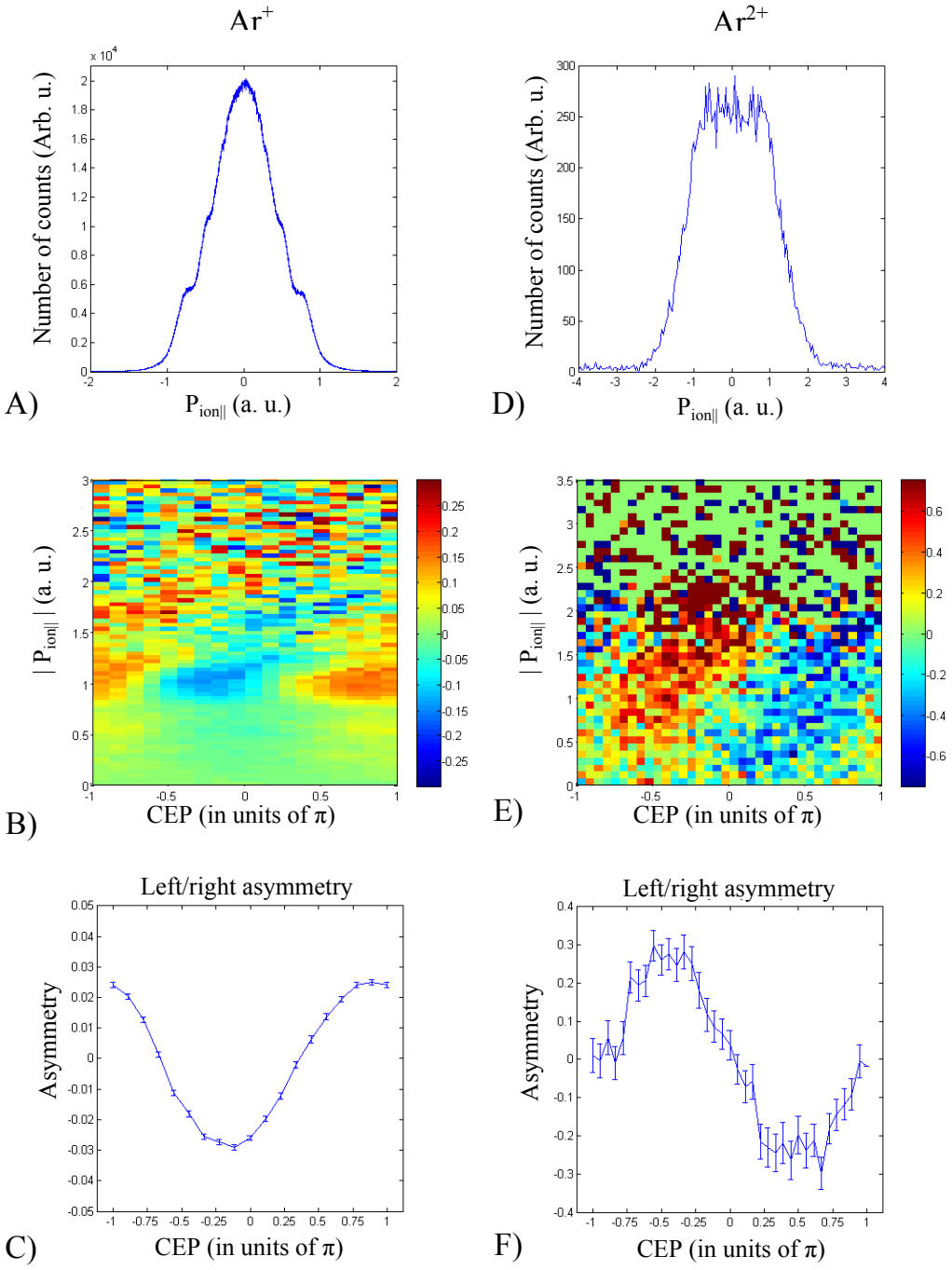

Figure 5.1: A) Longitudinal momentum of Ar^+. B) Asymmetry of Ar^+ as a function of the CEP and the absolute value of the longitudinal momentum. C) Asymmetry of Ar^+ as a function of the CEP integrated over all longitudinal momentum values. D) Longitudinal momentum of Ar^{2+}. E) Asymmetry of Ar^{2+} as a function of the CEP and the absolute value of the longitudinal momentum. F) Asymmetry of Ar^{2+} as a function of the CEP integrated over all longitudinal momentum values.

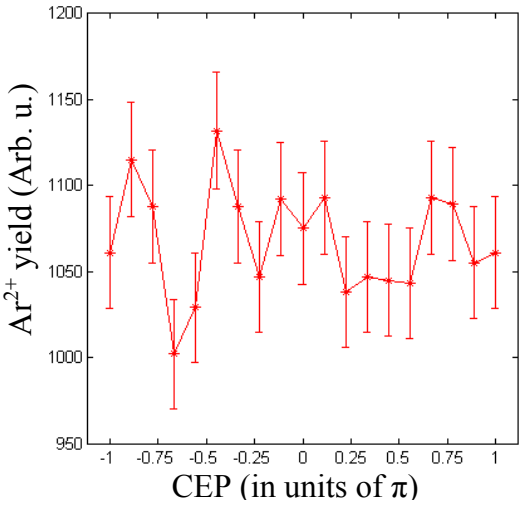

Figure 5.2: Doubly charged ion yield as a function of the CEP.

different ion momentum distribution. For example, at longer pulse durations a peak in the middle starts to form below $4.0 \cdot 10^{14}$ W/cm^2 ([REZ$^+$08]) until becoming the most important features for lower intensities [ELR$^+$03, LTR$^+$08, LYL$^+$10]. It was identified as electron pairs being emitted back to back (called anti-correlated) [LYL$^+$10]. The resulting doubly charged ion momentum has a small component close to zero. However, this specific mechanism whose origin has been identified in the multiple recollision mechanism ([LTR$^+$08, LYL$^+$10]) can be ruled out in the case of ultra-short laser pulses. In [RZF$^+$04] the utilization of ultra-short laser pulses made the middle dip more pronounced, advocating for the disappearance of this ionization channel. The results shown in the previous chapter, with a pronounced dip in the middle, confirmed the disappearance of this channel. For the present intensity, where a plateau is observed, this channel seems not to contribute using ultra-short laser pulses. Comparing to results [ELR$^+$03, REZ$^+$08] using the same intensity and a longer pulse duration, the middle peak is more pronounced. Nonetheless, it does not rule out the presence of another channel producing ions with small longitudinal momenta.

Other panels corresponds to the asymmetry for the ions looking at the dependence on the longitudinal momentum (B and E) or integrated over all counts (D,F). The patterns for both ions are very similar for the two intensities except for two differences: the momentum range over which the distributions extend, related to the intensity, and the CEP value at maximum asymmetries, not defined absolutely. The maximum asymmetry value is also larger in the lower intensity experiment than previously (for Ar^{2+}, the maximum of the integrated asymmetry is equal to 0.3 against 0.25 at higher intensity). This is probably not related to any physical reason but simply dependent on the characteristics of the laser used on the specific experiment.

Finally, as well as for the experimental investigation of chapter 4, the yield of the Ar^{2+} as a function of the CEP is examined and shown in figure 5.2. Similar to the higher intensity results, no clear CEP dependence is seen. We invoke the same explanation than in section 4.1, namely pulse durations that are still too long to observe this effect.

5.2 Electron correlation

5.2.1 Experimental results

The correlation graphs obtained for this intensity are displayed in figure 5.3. The result without CEP selection is shown on the top-left panel. The other panels present a phase selection with the value of the selected CEP indicated above each graph.

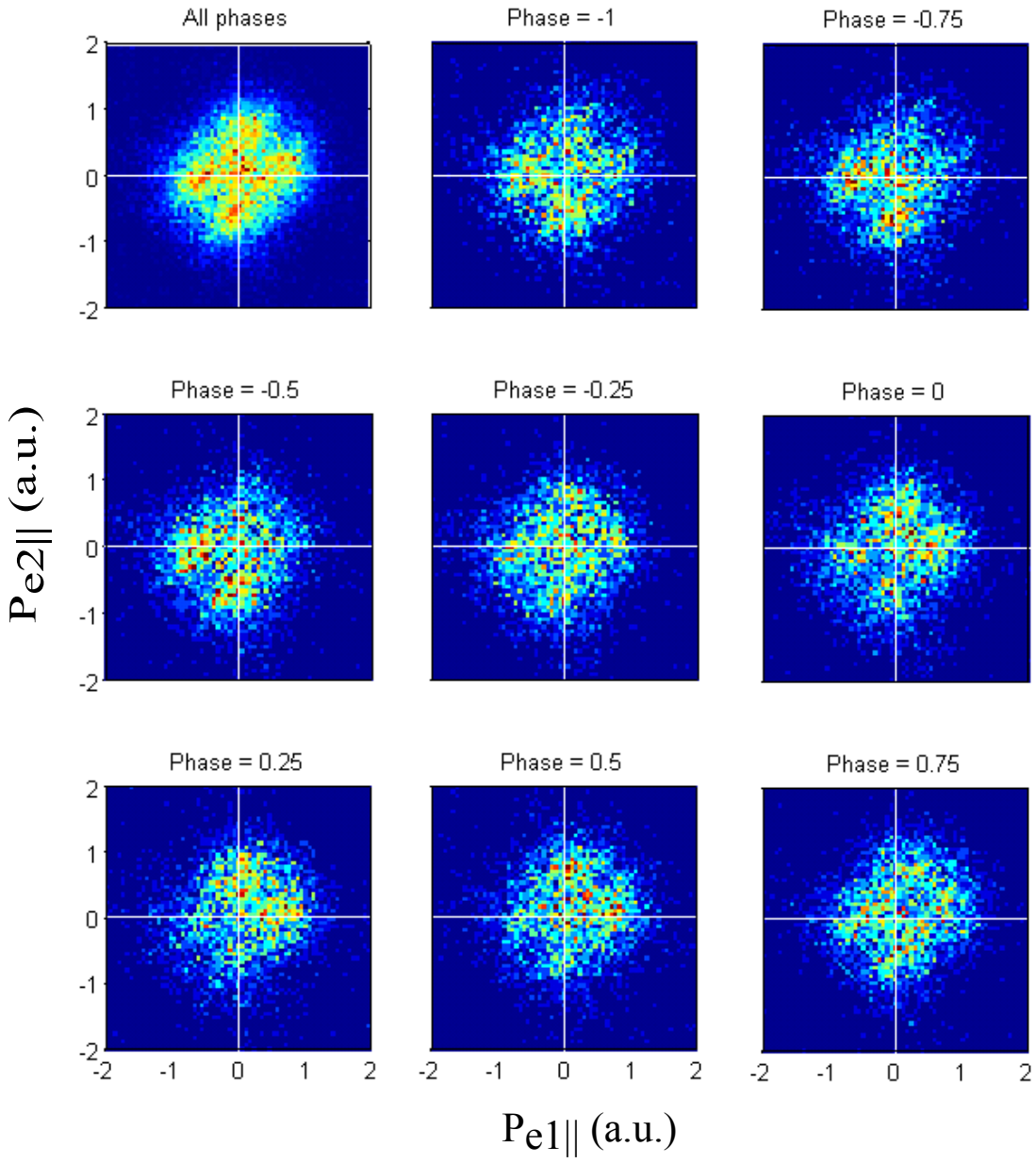

Figure 5.3: Correlation plot for Argon with different CEP characteristics. Top left panel: all phases are integrated. Phase selections are indicated for other panels with the selected phase given in value of π. The integration window around this central displayed value is $\pm 0.25\,\pi$. The color scale are not shown for visible purpose. In panel with all phases the maximum number of counts per bin goes to 40, in all other panels the maximum of the color scale is fixed to 11 counts.

From the panels at selected CEP in figure 5.3, we can observe the influence of the CEP on the distribution. Spanning the phase from -1.0 π to 0.75 π, we can observe that the center of gravity is shifting, along the diagonal $p_{e1||} = p_{e2||}$ from one side to the other. The maximum displacement is at the value of -0.5 π and 0.5 π, corresponding to the maximum of asymmetry for the ion longitudinal momentum. At this point, a displacement of the distribution along the $p_{e1||} = p_{e2||}$ diagonal as a function of the CEP is naturally expected because this diagonal represents the axis of projection of the distribution if we want to look at the sum of the two electrons ($p_{e1||} + p_{e2||} = -p_{\text{ion}||}$). Therefore variations along this axis are the same than for $-p_{\text{ion}||}$. No additional variation is observed with the CEP. As mentioned in chapter 1, the different ionization channels (e.g. RESI and (e,2e)-like ionization) have different CEP dependences. Observing the modulation of the pattern with the CEP can help to affect in the pattern the different structures related to the different ionization channels. This is not possible in the present case. It can be due to the lack of events recorded in order to observe any clear modulation. In the possibility that different channels exist, they might not show CEP-features distinct enough to appear on the correlation graphs.

We compare the correlation graphs at different intensities and pulse durations. Figure 5.4 shows the correlation plot for NSDI of argon with different intensities and pulse durations. Graphs A) and C) are for the same laser intensity ($0.9 \cdot 10^{14}$ W/cm^2) but different pulse durations, 6 fs and 25 fs, repectively. Graphs A, C and D) are obtained with ultra-short laser pulses but different laser intensity (indicated above each graph).

The comparison for the correlation plots at the same intensity but different pulse duration (graphs A) and C)) yields the same observation than results at higher intensity presented in chapter 4. We attribute it to the multiple recollisions present at long pulse durations.

For ultra-short laser pulses, the correlation plot at low intensity (graph A) presents some similarity with the ones at higher intensity (graphs B) and D)) such as an important distribution of points at the center. Nonetheless, the distribution is less broad than for higher intensities, as already suspected from Ar^{2+} longitudinal distributions. Furthermore, the shape differs. At low intensity, besides the population around (0,0), the distribution forms two branches, parallel to the $p_{e1||} = p_{e2||}$ diagonal. This structure is significantly different from the cross-shaped structure (graph D) and differs from the one presented also for 6 fs puses (graph B), more located on the axis.

In order to gain deeper insight on the experimental correlation plots at low intensity, we developed a semi-classical model which description follows.

5.3 The full 3D semi-classical model

The different steps considered are very similar to the semi-classical approach used in [YCL08, YLL08, XYL10]. The relevance of this latter approach was confirmed by the reproduction of the finger-like structure observed for NSDI of helium (cf chapter 1).

5.3.1 Description of the model

The theoretical model is detailed in this part. It is a Monte-Carlo simulation where the parameters randomly chosen are the CEP, the ionization time of the first electron in the laser electric field and its initial conditions.

The temporal evolution of the electric laser field is described by the formula:

$$F(t) = \begin{cases} F_0 \cos^2(\pi t/T_p)\cos(\omega t + \varphi_{CEP}), & \text{for t} \in [-T_p/2 \;\; T_p/2] \\ 0, & \text{else} \end{cases} \tag{5.1}$$

The first function ($F_0 \cos^2(\pi t/T_p)$) describes the envelope of the pulses, centered at t=0, where T_p is the length of the pulses and $\cos(\omega t + \varphi_{CEP})$ is the oscillation of the carrier wave being chosen with $\omega = 0.057$ a.u. (800 nm).

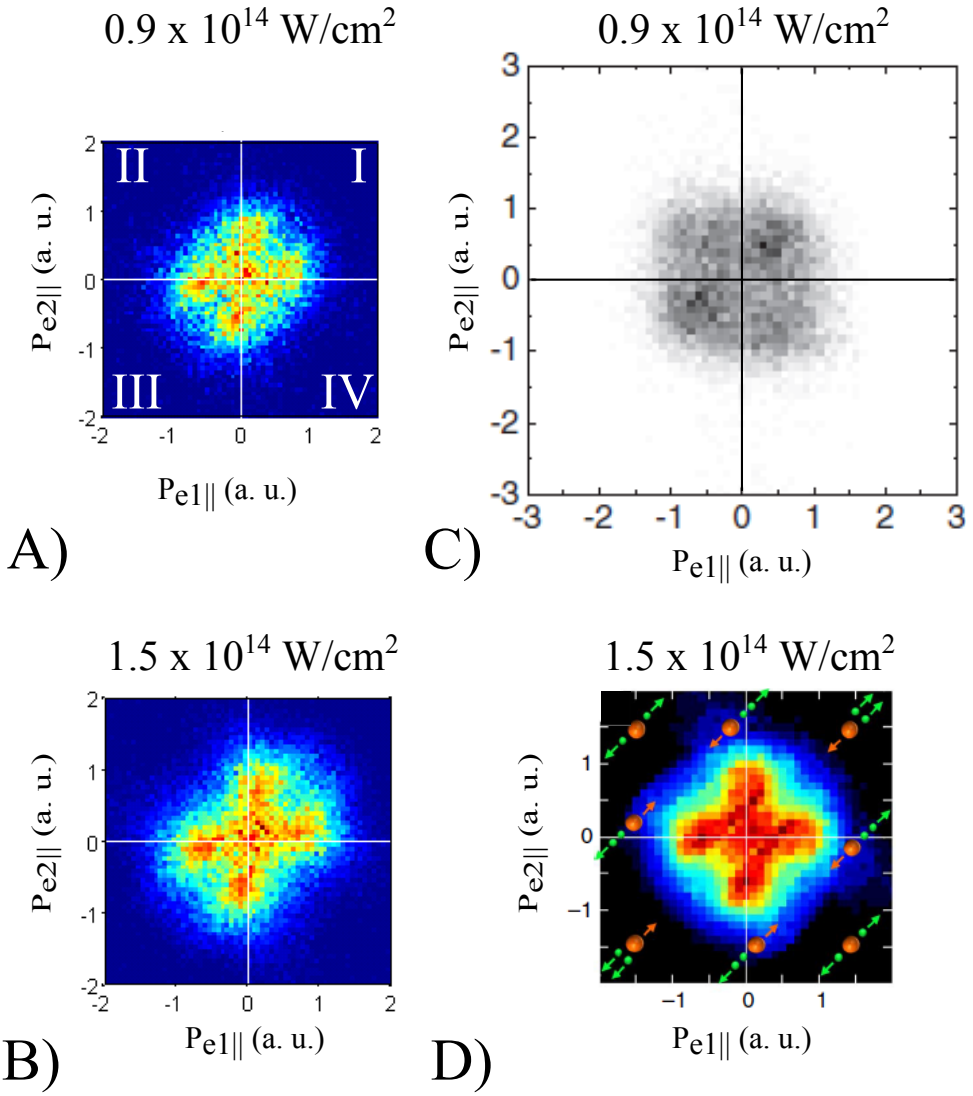

Figure 5.4: Correlation plot for NSDI of argon. A) Obtained with 6 fs laser pulses and an intensity of $0.9 \cdot 10^{14}$ W/cm^2, same as shown in figure 5.3 A). The label of the four quadrants are indicated. B) Obtained with 6 fs laser pulses and an intensity of $1.5 \cdot 10^{14}$ W/cm^2 same as shown in figure 4.7A) in chapter 4. C) Obtained with 35 fs laser pulses and an intensity of $0.9 \cdot 10^{14}$ W/cm^2. D) Obtained with 3.8 fs laser pulses and an intensity of $1.5 \cdot 10^{14}$ W/cm^2. Graph C) is taken from [ELR$^+$03] and graph D) is taken from [BKJ$^+$12].

The first electron tunnels out at a time t_0, the transition rate follows the static tunneling formula:

$$\omega(t_0) \propto \exp(-\frac{2}{3}\frac{(2I_p)^{3/2}}{|F(t_0)|}) \tag{5.2}$$

At time t_0 the tunneling electron is placed on the outer edge of the Coulomb barrier. Like in section 4.2.2, the coordinates of the position fulfilling the condition are (with a laser polarized in the z-direction):

$$\begin{cases} -I_p = -z_t E(t_0) + V_i(z_t) \\ x_t = 0 \\ y_t = 0 \end{cases}$$

The momentum of this particle is defined such that the longitudinal velocity is equal to zero at t_0 and the transverse velocity is randomly chosen with the probability distribution being a Gaussian centered at zero and having a standard deviation of:

$$\sigma_\perp = \sqrt{\frac{F(t_0)}{2\sqrt{2I_p}}}$$

The inner electron is placed on an elliptic orbit in the Coulomb potential of the doubly charged ion. The micro-canonical distribution is taken as in [LP79] with the energy of the bound electron being equal to the Ar^+ ionization potential (27.2 eV =1.01 a.u.). The system evolves in three dimensions considering classical Newton equations. For each electron, in atomic units, this reads:

$$\frac{d^2 r_i}{dt^2} = -E_{\text{field}}(t) - \nabla(V_i(\vec{r_i}) + V_{12}(r_i)) \tag{5.3}$$

Because of the full classical evolution, an electron being at the energy level E_{bound} can only be ionized when the Coulomb barrier is completely suppressed by the laser field (over the barrier ionization, equation (1.6)). The electron can thus escape the ionic core above the saddle formed.

Using a three dimensional model has proven to bring many advantages in order to extract information about energy of the electrons and the different times involved in the process. Nonetheless, two comments have to be made to interpret this information. The total energy of each of the two electrons is defined through the formula:

$$E_{ele_n} = \frac{v_n^2}{2} + \frac{2}{|r_n|} \quad . \tag{5.4}$$

Where $\frac{v_n^2}{2}$ is the kinetic energy ($m_e = 1$) and $\frac{2}{|r_n|}$ the potential energy in the ionic coulomb field. This definition is the same in comparison to the definition used by other groups developing semi-classical simulations (Liu and coworkers [YCL08, YLL08, XYL10, YL10], Uzer and coworkers [MCU09, MCU10b, MCU10a, MKCU12]). To be noted that the energy related to the laser field is not included. This definition implies negative energies of the electron right after tunneling (even though it is considered as "free") but does not change its energy at recollision where the electric field is close to a zero-crossing.

Using this energy definition, we define the different times similarly to the definition used by Liu and coworkers and Uzer and coworkers. The time of tunneling is straightforward because it represents the starting point of the calculations. The other times of ionization are defined as the time when the energy of the electron becomes positive.

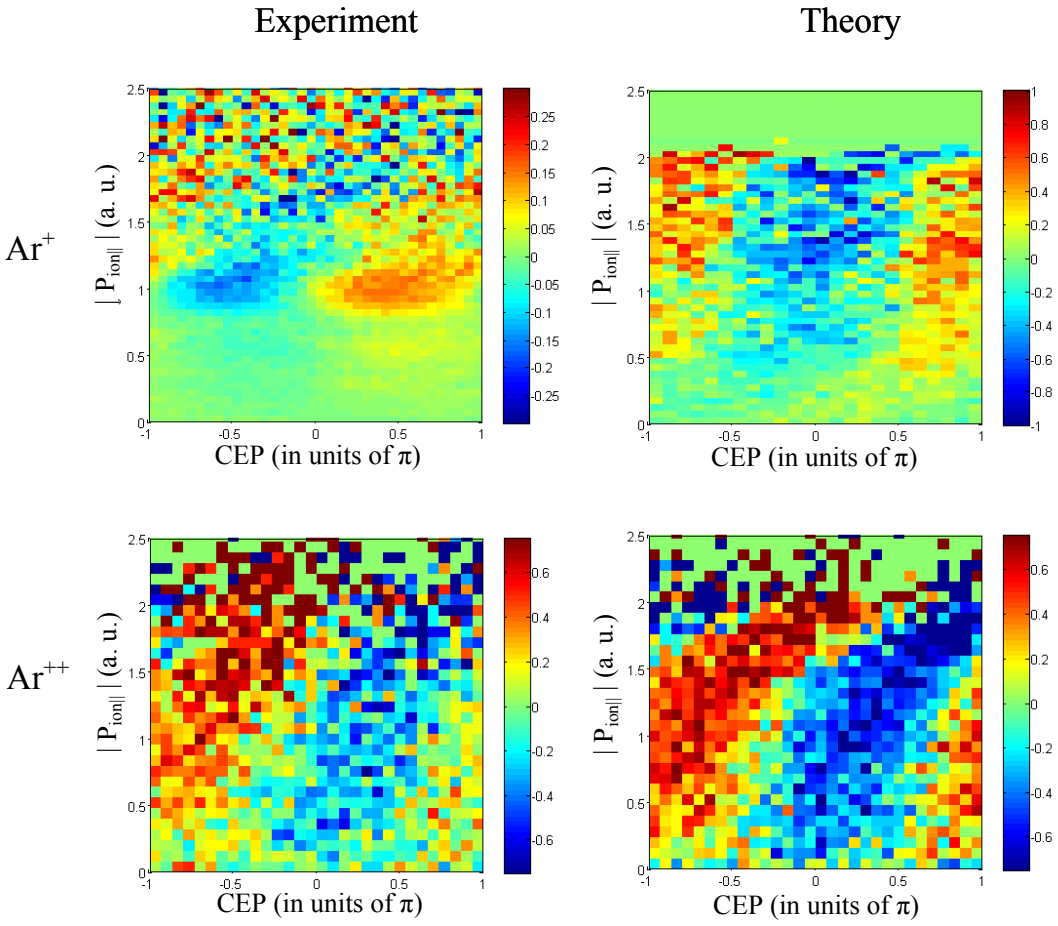

Figure 5.5: Comparison between experiment and theory of the asymmetry distributions as a function of the CEP and the longitudinal momentum for different ions. As labeled the left column corresponds to experimental data with the CEP shifted by -.28 π in comparison to the data presented in 5.1, in the right column are the theoretical distributions. The top row represents the distributions for Ar^+ and the bottom row the distributions for Ar^{2+}.

5.3.2 Comparison with experiment

Ion distributions

Utilizing the model defined, we represent the results for an intensity of $0.9 \cdot 10^{14}\,\mathrm{W/cm^2}$ and a total pulse length T_p of 11 fs (four optical cycles). We first consider the asymmetry as a function of the momentum for the singly and doubly charged ions. The results are represented in figure 5.5. The experimental plots are the same than presented in figure 5.1 but the CEP is shifted by -0.28 π such that the asymmetry of the doubly charged ion corresponds to the theoretical asymmetry. As already mentioned, the experimental CEP value is determined relatively.

We can see that the distribution for the doubly charged ion is well reproduced by our model calculation: the shape of the distributions are very similar with a slight tilt of the asymmetry at low momentum values. The pattern stops close to 2.0 a.u., only noise is visible for higher values. For both experiment and model, the asymmetry axis is the same [-0.7 , 0.7]. The theoretical asymmetry is nonetheless slightly larger than the experimental one. This can be attributed to different effects.

Amongst them, the focal averaging where experimentally different intensities contribute, the Gouy phase (cf section 3.1.2), noise in the experimental distribution which attenuates the CEP effects or simply the laser duration slightly shorter theoretically than in the experiment. The singly charged theoretical distribution deviates from the experimental distribution, especially concerning the value of the asymmetry, the color scale has been adjusted in each case. It should be pointed that it is equal to [-0.25 0.25] for the experiment and [-1.0 1.0] for the theory. The shape also differs quite substantially. Nonetheless the agreement between the Ar^{2+} distributions is very encouraging to investigate the correlation plots.

Electron correlation with the model

The calculated correlation graphs shown in figure 5.6 have the same CEP-selection as in figure 5.3. In the top-left panel, no phase selection is applied and other panels have a phase selection of the CEP indicated above each graph. Comparing the two panels (experimentally and theoretically) for integrated phases, a good agreement can be found. The two branches parallel to the $p_{e1||} = p_{e2||}$ diagonal are remarkably well reproduced. A discrepancy is nonetheless present concerning the center of the distribution (point (0,0)) which exhibits a minimum in the theoretical model. We attribute it to the focal averaging which introduces ionization events at lower laser intensities than the one considered here. As was shown in [YL10] utilizing the same model, for a decreased intensity, the distribution is much closer to the center. The tunneling ionization of the second electron after recollision might also contribute. It happens preferentially at a maximum of the peak where the vector potential is zero. Since the electron has initially zero longitudinal velocity, it finishes its interaction with a small final momentum. Nonetheless simulations [pri] indicated that tunneling ionization is observed for 7% of all NSDI events, at this intensity. The shift with the CEP is similar to the experiment where a variation along the $p_{e1||} = p_{e2||}$ diagonal can be observed.

Considering this model as a good representation of the experimentally obtained correlation plots, we use it to extract information about the ionization mechanism. Particularly, we look at the electron energy as a function of time to observe the state after recollision.

5.3.3 Analysis of electrons trajectories

Figure 5.7 represents the energy of the electrons as a function of time, for two representative events. The first trajectory curves are in solid lines, in blue the energy of the recolliding electron and in green the energy of the bound one. The second trajectory curves are in dashed lines with the same color code. To understand the time axis, the electric field of the pulse is represented in red, where the CEP is equal to $\pi/2$. The recollision can be spotted as the moment where the energy of the first electron decreases sharply and the energy of the second increases. The definition for the time of recollision is the minimum of the first electron energy. For the presented trajectories one can notice that the second electron is not directly ionized, only excited. This is in accordance with the RESI mechanism already pointed out in chapter 4 for a larger intensity. By decreasing the intensity, this process is emphasized. The first electron does not possess enough energy at the recollision to ionize the bound one directly at the impact.

However, in contrast to results presented at higher intensity, after the recollision the returning electron is bound again. Its energy is negative after recollision, even for more than an optical cycle as shown by the blue dashed line. This is the formation of a doubly excited state. Such a state although usually shadowed by RESI or (e,2e)-like processes has already been implied for participating in NSDI in several works ([SE01, ELR$^+$03, HSSP08, CLL10, LL10]. The formation of a doubly excited compound happens in 97% of all events.

From figure 5.7, we can identify the different ionization times, the crossings of the blue and green curves with the zero energy line. In case there is more than one crossing (e.g. solid green curve) we take the first zero-crossing as the time of ionization. In order to relate both ionization times, we examine their time difference predicted by the classical model.

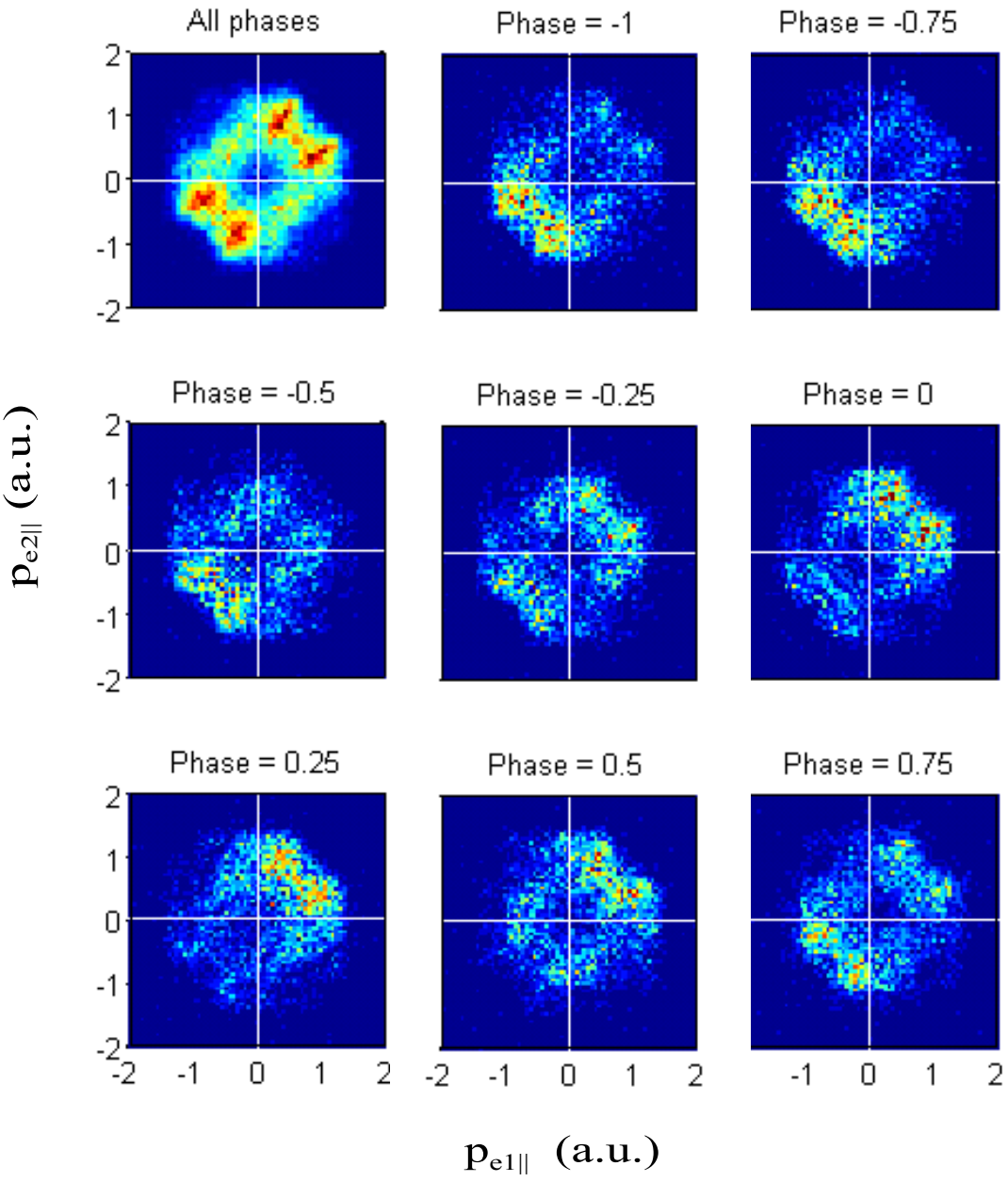

Figure 5.6: Same as figure 5.3 but for the results from the semi-classical model.

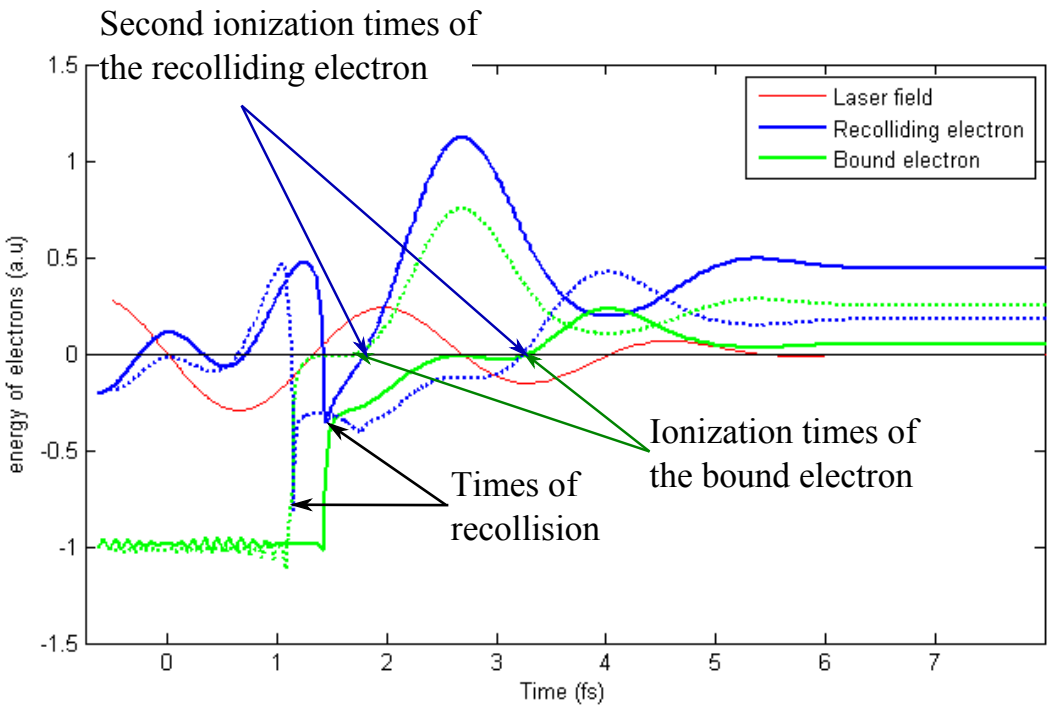

Figure 5.7: Electrons energy as a function of the times in the laser field for two different events (solid and dashed curves). The blue curve represents the energy of the recolliding electron and the green one the energy of the bound electron. In red is represented the laser electric field for the first event to guide the interpretation of the times involved.

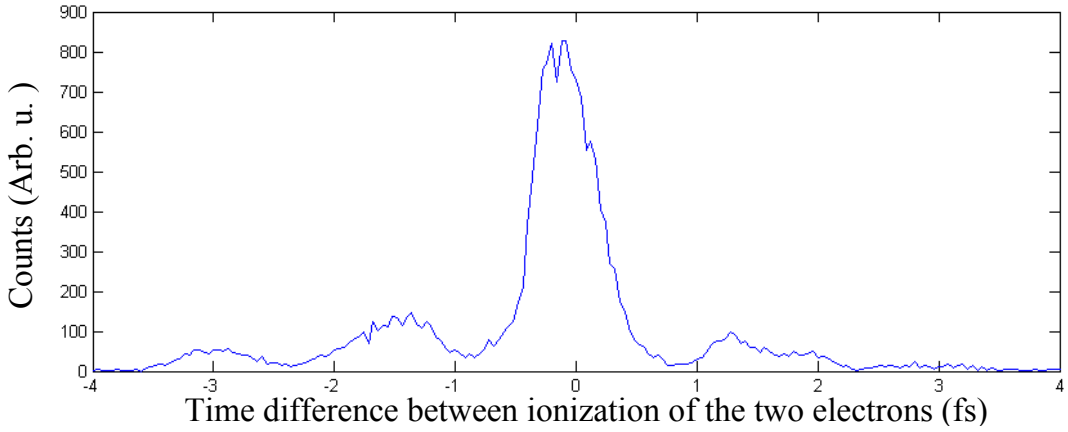

Figure 5.8: Time difference ΔT between the second ionization of the recolliding electron and the ionization of the bound one in femtoseconds.

This is shown in graph 5.8 with the distribution of this difference in ionization times in femtoseconds. Positive ionization time differences mean that the recolliding electron is ionized first, negative time differences that the second electron is ionized first. The middle peak represents events where the two electrons are emitted during the same laser cycle, the secondary peaks centered around ± 1.35 fs represent events where the electrons are ionized with a time difference of one half-cycles. The peaks at even higher time differences represent events where the two ionization times are separated by one or more optical cycles (2.75 fs). The counts in the middle peak represent (69%) of all events.

This confinement of the counts in the middle peak is due to the short pulse duration. The electric field of the laser (red curve in figure 5.7) contains only few half-cycles where the probability of ionizing the electrons is non-negligible (the probability varies quadratically with the electric field maximum, cf equation (1.6)). If the ionization is limited to fewer cycles, the probability of ionizing two electrons in the same one increases.

The distribution shows an apparent symmetry. An intuitive picture is that the two electrons, having different dynamics before recollision, would still exhibit different characteristics (bound energies) after recollision and therefore are not equal in regards of which is the first to be ionized. The symmetry indicates a loss of memory of the dynamics before the recollision. This is in agreement with the results presented in [YL10] where the maximum of the distribution of energy difference between the two electrons (after recollision when considering trajectories with maximum recolliding energy) is found for two electrons having the same energy. This feature can be explained by the fact that the configuration where both electrons share equal energy is the most favorable at these intensities whereas if one electron " keeps " all the energy the other has fewer chance to be ionized.

We investigate the influence of the difference in ionization time on the momentum of the electron. We make a selection on the value of ΔT and represent the correlation plot for the events fulfilling the selection. The selection is made between the events belonging to the secondary peaks ($|\Delta T| \in [0.85 \;\; 2.3]$ fs) and the events in the first peak, divided into three parts: $|\Delta T| \in [0.05 \;\; 0.15]$ fs , $|\Delta T| \in [0.20 \;\; 0.30]$ fs and the events fulfilling $|\Delta T| \in [0.35 \;\; 0.45]$ fs. For these four intervals the corresponding correlation plot is shown in figure 5.9. The most straightforward interpretation concerns the plot top-left corresponding to the events where electrons are ionized with a half-cycle differences. The vector potential of the laser changes of sign between two half-cycles. Therefore the final momentum of the electrons, largely influenced by the vector potential value at the moment of ionization (cf equation 1.14) likely changes sign. The two electrons populates preferentially quadrants II and IV with emission in opposite direction. For the graphs (B-D), a clear evolution can be seen when reducing the time delay between ionizations. The branches of the distribution parallel to the $p_{e1||} = p_{e2||}$ diagonal are closer to each other

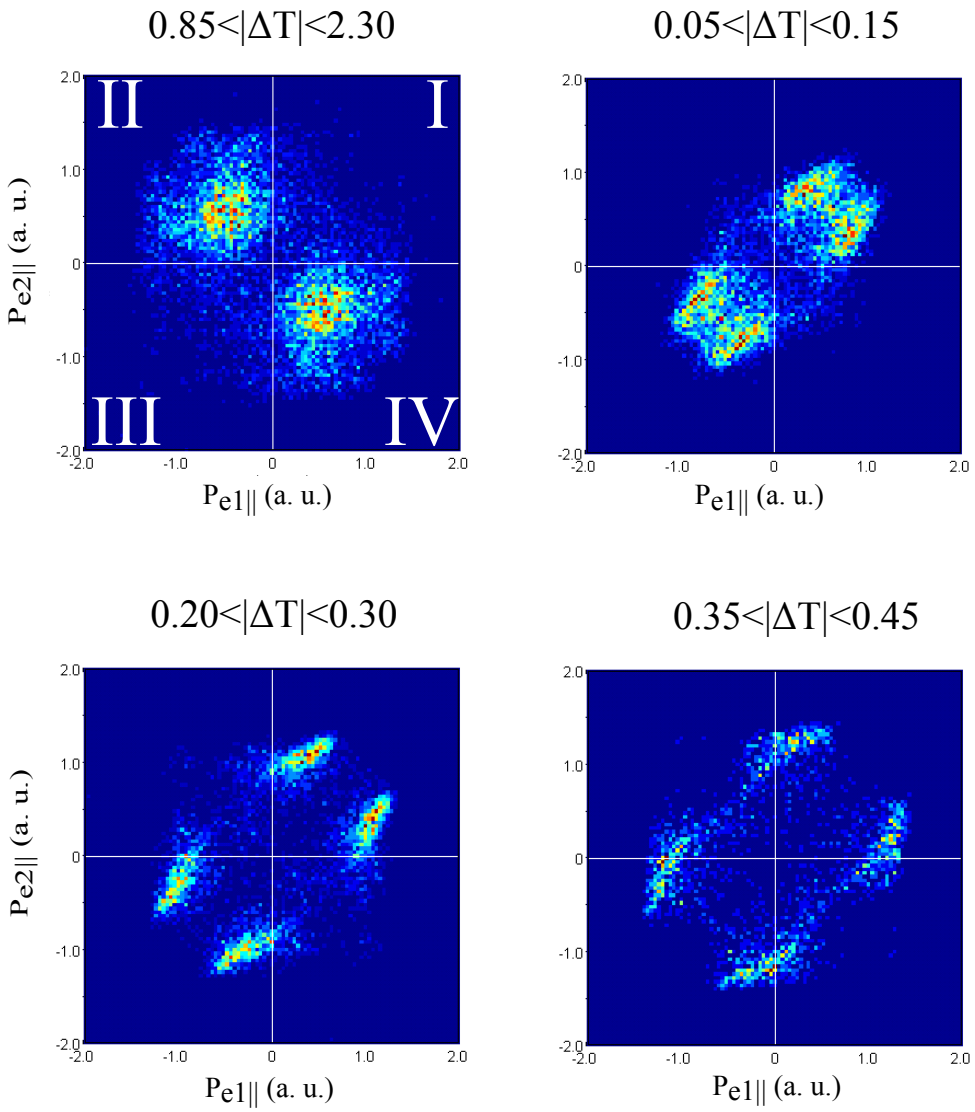

Figure 5.9: Correlation plots for different ionization time difference (ΔT in femtoseconds). The different values for the cut are indicated above each graph.

with decreasing $|\Delta T|$. Physically this distance between the two branches represents the difference between the longitudinal momentum of the two electrons. The diagonal $p_{e1||} = -p_{e2||}$ is the axis of projection of the distribution when considering this difference $\Delta P = p_{||e1} - p_{||e2}$. For instance, a point with $p_{||e1} = p_{||e2}$ would sit on the $p_{e1||} = p_{e2||}$ diagonal and the projection of this point on the $p_{e1||} = -p_{e2||}$ diagonal would be at zero. The localization of the distribution on branches first indicates that a given electron longitudinal momentum difference ΔP is favored for a given ΔT and second that ΔP evolves with it.

A first argument can be derived to interpret this feature considering the vector potential of the laser ($E(t) = -\frac{dA(t)}{dt}$) and the fact that the final momentum of an electron depends mainly on this value at the moment of ionization (cf. section 1.2.2).

Assuming that one of the two electron has a ionization time at the maximum of the electric field, where the vector potential is zero, its final momentum is close to zero. The more delayed the other electron ionization will be, so larger its vector potential value and the larger the difference in momentum value.

Such an argument relating, through the vector potential of the laser, the difference in ionization time to the difference of momentum has its limits. If in theory the probability of ionization is maximum at a peak of the electric field, there could be a depletion effect. When the probability of ionization for an electron is high, the electrons are ionized before the peak maximum altering the distribution of ionization times over the peak. Furthermore, in contrast to the definition of tunnel ionization, the initial longitudinal velocity of the electron is not zero. This reduces the influence of the vector potential on the final momentum value of the electrons.

In the following we study the creation of a doubly excited state during the recollision process. We realize a theoretical investigation where we implement such a state in the laser field at the moment of recollision and study its evolution. We are especially concerned by the correlation plot obtained with such a state to see whether such a transition state is plausible. We study also the correlation between ΔT, the difference in ionization time, and ΔP the difference between the longitudinal momentum of the two emitted electrons.

5.4 Model calculation with intermediate doubly excited state

5.4.1 Description of the model

The doubly excited model developed is similar to the full semi-classical simulation. Until the recollision, the system evolves as described previously, with the first electron tunneling, evolving classically in the laser field and the second electron being bound. If a recollision is detected (decrease of the energy of the first electron below zero), the system is replaced by a doubly excited state.

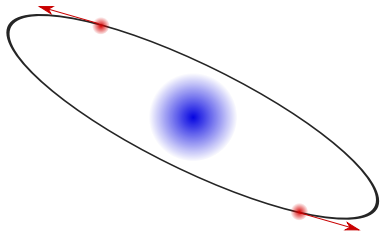

Figure 5.10: Representation of the initial doubly excite state initial conditions as computed in the simulation, in red the two electrons and in blue the ion.

An infinite numbers of classical doubly excited states exist, but we restricted our distribution to states which are stable without electric field. Although in practice the system would not restrict itself only to stable states after recollision, having such a configuration allows to test the simple, classical constraints imposed on a doubly exited state by the electric field.

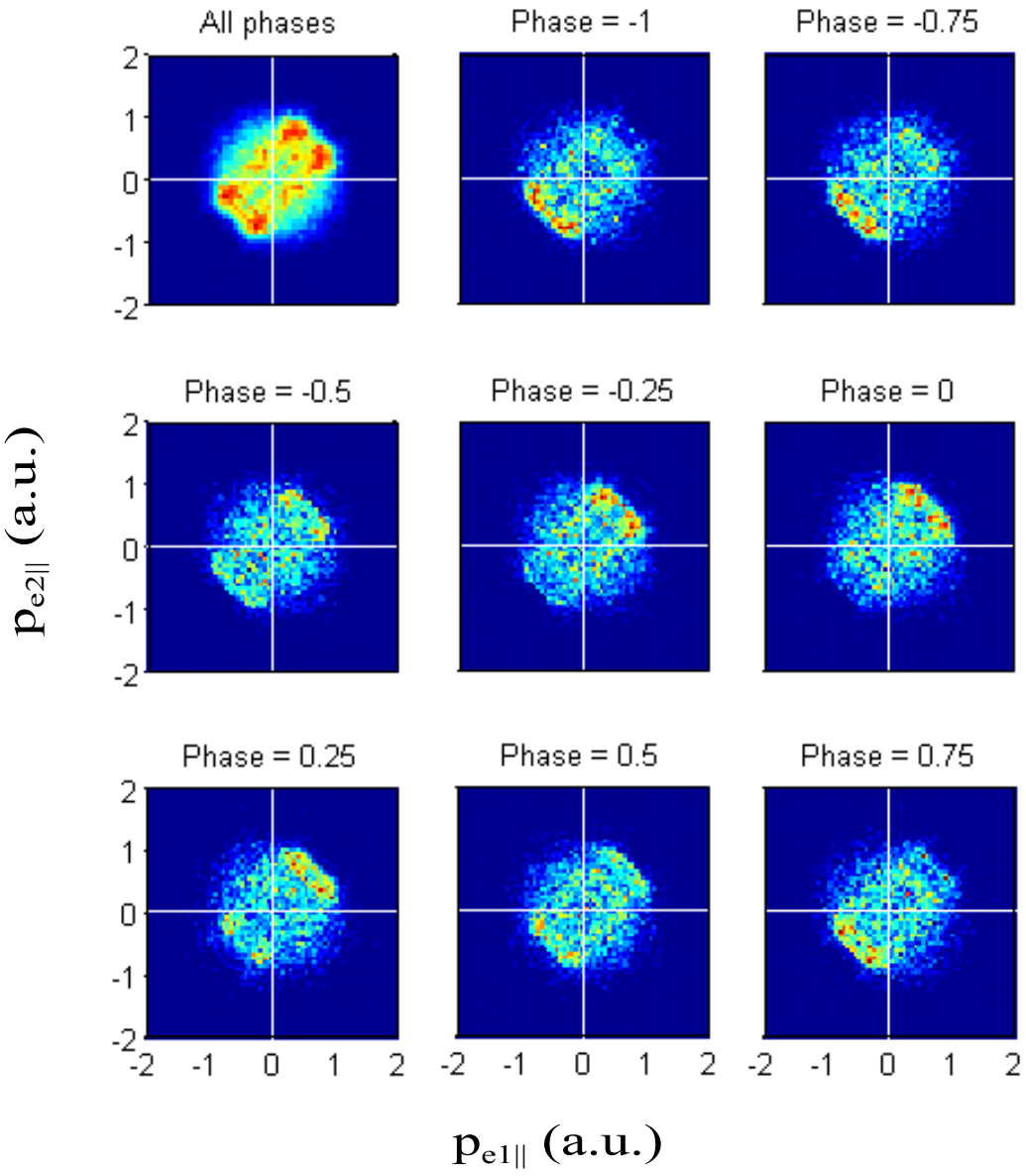

Figure 5.11: Same as figure 5.3 for the results from the doubly excited compound model.

Theoretically, such a non-auto-ionizing doubly excited compound (DEC) is modeled by placing the two electrons diametrically opposite to each other on the same orbital and with the same angular momentum. Its representation is shown in figure 5.10. The total sum energy of the two bound electrons is taken as -0.3 a.u. This is equal to the energy of the system after recollision for the most energetic trajectories: $I_{p2} + 3.17\,U_p = -1.01 + 0.7 = -0.3$ a.u. The orbit of the electron is chosen in the same manner than the distribution of the bound electron in the full semi-classical simulation.

5.4.2 Comparison with experiment

Figure 5.11 shows the correlation plot obtained for the doubly excited compound simulation. Like for figure 5.3 and 5.6, in the top-left panel the correlation plot for all CE-phases is shown and for other panels, a phase is selected as indicated above each graph.

The graph for all phases resembles the correlation plot obtained experimentally. Compared to the full semi-classical calculation, the results yield a distribution more populated close to zero and in quadrants II and IV. This makes it more similar to the experimental data than the other theoretical results. We investigate the evolution with the CEP as with previous presented correlation plot, the graphs are shown for different phases. Although we implement the doubly excited state during the pulse, the CEP has still some importance. It influences the time of recollision (and the time of formation of the DEC) due to the electron propagation in the electric field (before recollision). After formation of the DEC, the CEP influences the maxima of the electric field and the streaking of the electron by the field after ionization. Although the evolution of the correlation plot is similar to both experimental and semi-classical simulation correlation plots, with an evolution along the $p_{e1||} = p_{e2||}$ diagonal, the maximum of asymmetry in the distribution differs slightly from the full semi-classical simulation. In the DEC simulation, maximum asymmetry is obtained for -0.87 and $0.13\,\pi$. For the full semi-classical simulation, they are located at -0.73 and $0.27\,\pi$, showing that the memory of the recollision process is not completely lost in the formation of a DEC. Nonetheless, such a DEC reproduces the features observed experimentally and provide a simple system to observe the ionization dynamics of two excited electrons in an ultra-short laser field.

5.4.3 Extraction of ionization times

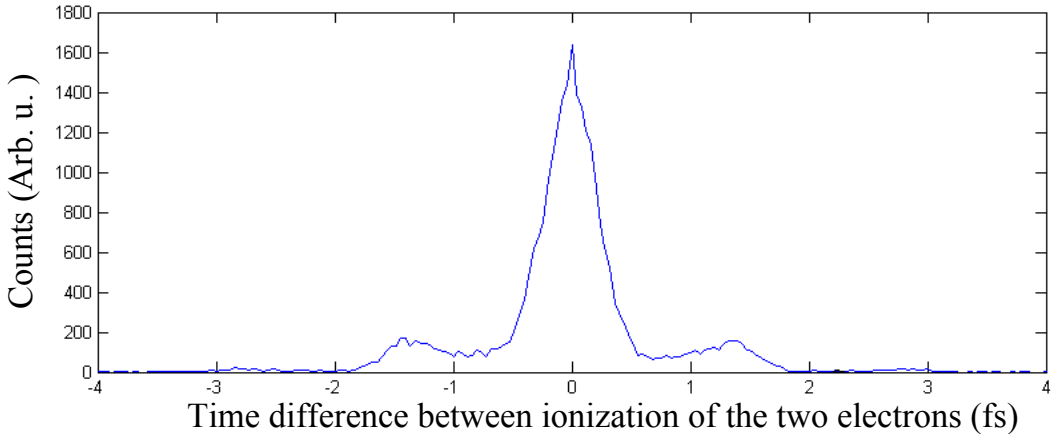

Figure 5.12: Time difference ΔT between ionization of the recolliding electron and the bound one in femtoseconds.

The dynamic is studied as previously by looking at the influence of ΔT, the difference between ionization times, over the correlation plots. Figure 5.12 shows the distribution for ΔT, which is

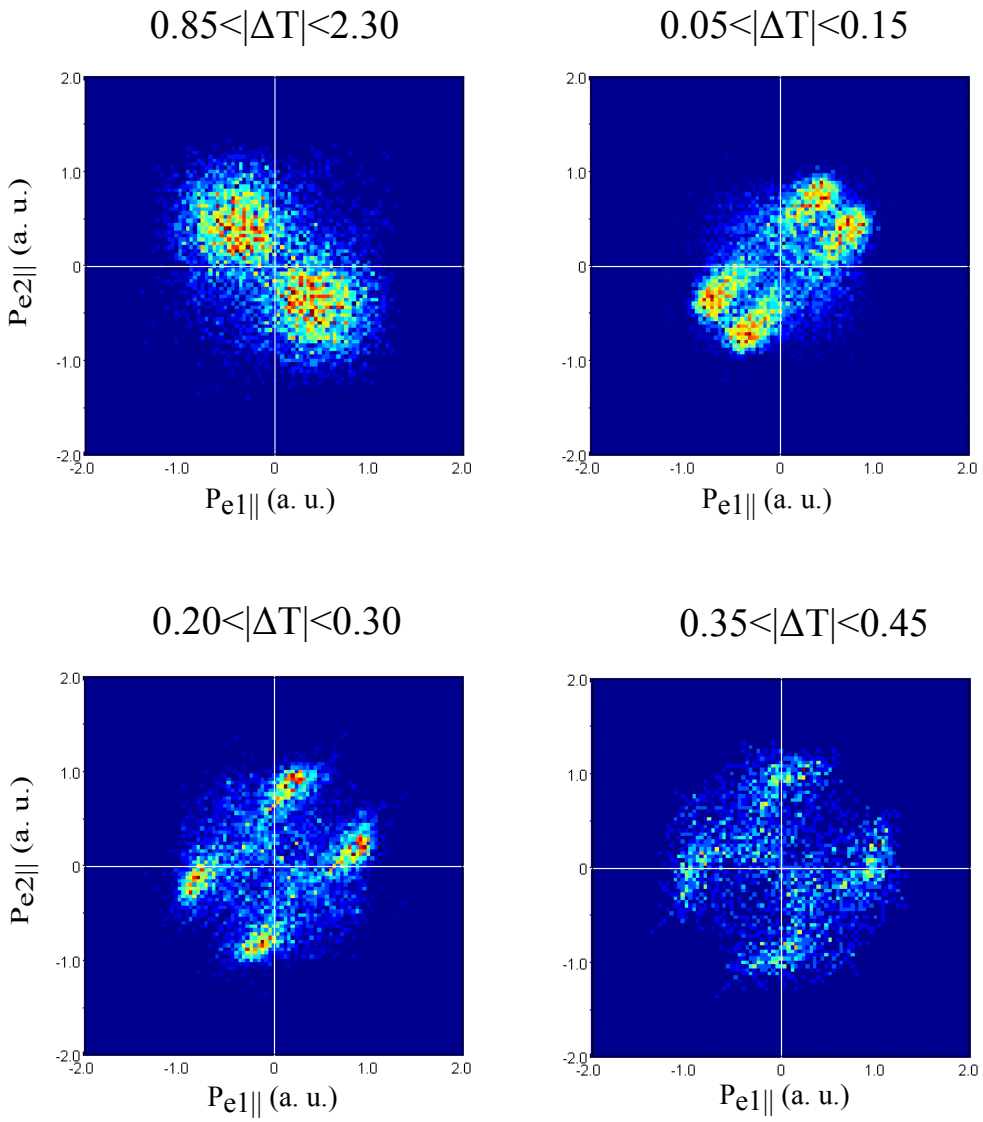

Figure 5.13: Same as figure 5.9 for the results from the doubly excited compound model.

similar to figure 5.8. Most of the counts are located in the middle peak (80 % of all counts) again due to the short duration of the pulse.

In contrast to figure 5.8, the distribution is completely symmetrical. Due to the fact that the two electrons are set with equal condition on the orbit (only their position differs), no preference is expected for any of the two electrons.

Again we look at the influence of ΔT on the momentum acquired by the two electrons. We make selection on ΔT and observe the correlation plot of the events fulfilling the time condition, the results are displayed in figure 5.13, the same time selection has been applied than in figure 5.9. The same trend can be seen than in figure 5.9, with anti-correlated electron for the events corresponding to a half-cycle difference in ΔT, the origin of this is the same than discussed before, with electrons ionized for different sign of the electric field and therefore emitted in opposite directions. More importantly is the reproduction of the observed trend that when ΔT decreases the distance between the two branches increases. The overall shapes of the selected correlation plot differ from the one observed in figure 5.9. But from the beginning, without any selection on time, the correlation plot differs already slightly between the two simulations.

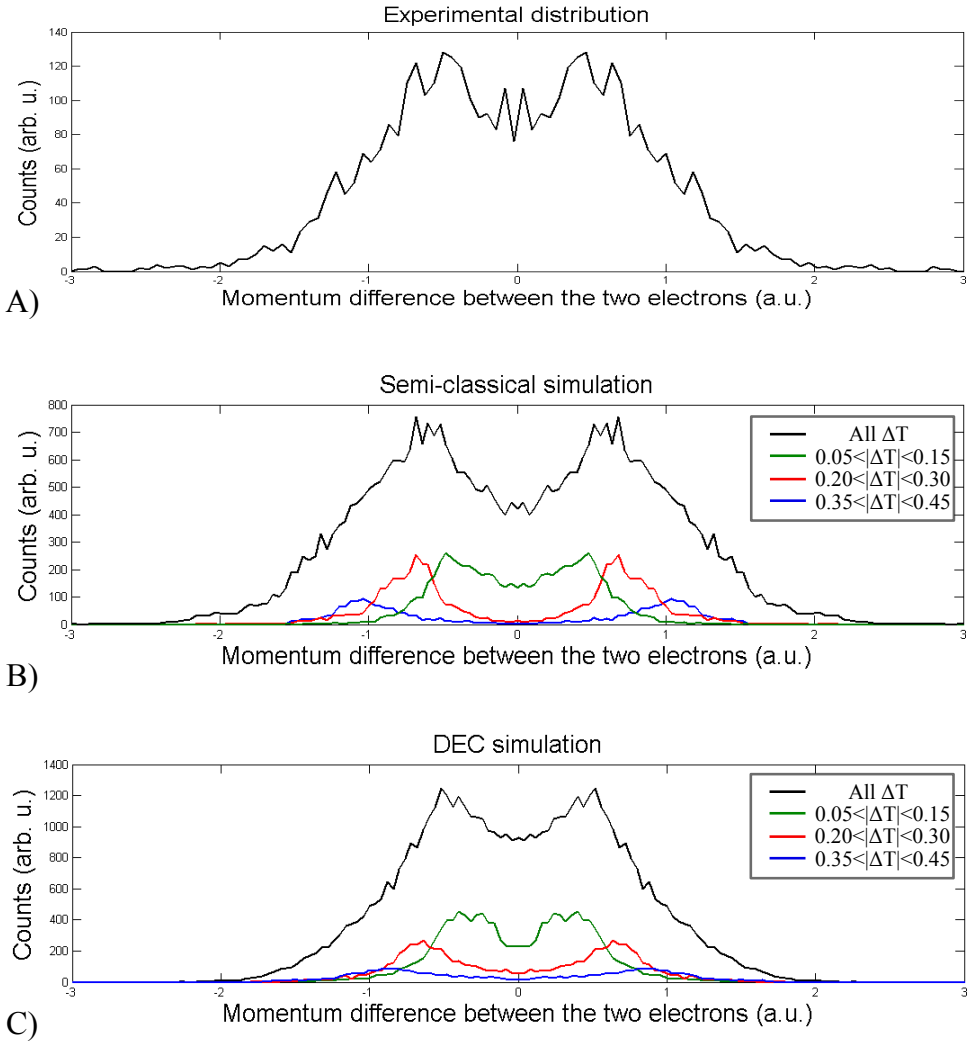

Figure 5.14: ΔP distribution for different systems and different conditions. A) The experimental distribution B) the semi-classical distribution and C) the DEC simulation. For the theory graphs a distinction can also be made on the different ΔT, the values used are the ones also selected in graphs 5.9 and 5.13.

This distance between the two branches can be quantitatively measured through the difference between the longitudinal momentum of the two electrons ΔP. This different distributions ΔP are presented in figure 5.14. Graph A) represents the experimental distribution. Graph B) represents the full semi-classical distributions, the black curve corresponds to the distribution when all events are taken. The color curves (green, red and blue) correspond to the distribution when a time selection is made on the events ($0.05 \leq \Delta T \leq 0.15$, $0.20 \leq \Delta T \leq 0.30$ and $0.35 \leq \Delta T \leq 0.45$, respectively). These selections are the same than used in figure 5.9 and 5.13. The graph C) is similar to graph B) but for the DEC simulation. These two last graphs help to see qualitatively the evolution of ΔP as a function of ΔT. For both simulations one can notice the peaks having their center shifted to larger value when increasing the time difference between ionization of the two electrons.

For each value ΔT one can associate a value ΔP in order to reconstruct the function $\Delta T = f(\Delta P)$. To measure the peaks of a given ΔP distribution (see figure 5.14), we fit it by the function:

$$f(x) = a\left[\exp\left(\frac{-(x-b)^2}{2\sigma^2}\right) + \exp\left(\frac{-(x+b)^2}{2\sigma^2}\right)\right] \tag{5.5}$$

This represents the addition of two identical Gaussian centered at b and $-b$. The fitting parameter are a, b and σ where a is the amplitude/maximum of the function, b indicates for which value the maximum is obtained (since both solution b and $-b$ are possible, we choose the positive value) and σ is the standard deviation of the Gaussians. The parameter b is therefore, for a given ΔT, equal to $\Delta P/2$. From these fits can be extracted the function $\Delta P = f(\Delta T)$. Since the experimental observable is ΔP (cf graph 5.14 A)) we represent the inverse function $\Delta T = f^{-1}(\Delta P)$ in order to relate our measured value with a theoretical ΔT. These functions are presented in figure 5.15 (see caption for the color code).

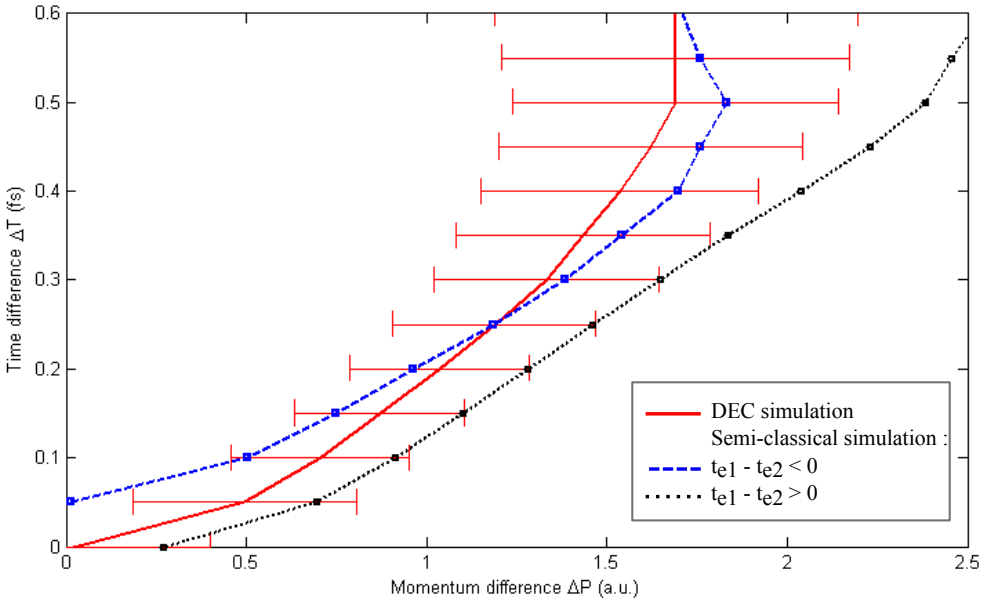

Figure 5.15: ΔT as a function of ΔP for the different simulations, in red solid line for the case of the DEC simulation, in black dotted line, for the semi-classical simulation when the bound electron is ionized before the recolliding electron, in blue dashed line also the semi-classical simulation when the recolliding electron is ionized first. The error bars are the standard deviation parameter σ of the fitting Gaussians. For visual convenience is only represented the error bar for the DEC curve, nonetheless the error bars for the semi-classical curves are of the same magnitude.

The functions differ from each other for $\Delta P \leq 1.3$ a.u. but a good agreement can be found for lower ΔP between the curve from DEC and both curves issued from the semi-classical model. This

accredits the formation of a doubly excited compound at the recollision. This also suggests that although the implementation of a doubly excited state relies on the development of a rather simple model, where the evolution in the laser field is considered fully classically, a robust correlation can be found between the difference in ionization times and the electron momenta. We use this correlation to relate the measured observable with electron dynamics. Measuring the experimental value, we obtain $\Delta P = 1.14 \pm 0.47$ a.u. Looking at the correspondence between ΔP and ΔT from the DEC model, the most likely delay between the ionization of the two electrons is 200 ± 100 attoseconds. This value is model dependent. Taking the full semi-classical models yields 200 ± 100 or 125 ± 100 as depending on which electron is ionized first.

Chapter 6

Measurements with two-color laser pulses

In this chapter experimental results for Non-Sequential Double Ionization of argon with two-color laser pulses are presented. A doubled frequency component (blue) is generated from the fundamental laser beam (red) and superimposed on it. Such experiments have shown the possibility to create an asymmetric electric field. Its shape can be controlled with sub-femtosecond precision depending on the relative amplitude and phase between the blue and red field. The influence of this asymmetric field on the emission direction and energy of singly charged atoms has already been demonstrated and analyzed, this is addressed in the first section as a confirmation of the two-color scheme. In the second part results about the control of the trajectories in the case of NSDI are presented.

6.1 Single ionization

6.1.1 Phase effects

In section 2.4 the possibility to create and superimpose the second harmonic component over the fundamental was shown. In this section the application of a two-color experiment to the single ionization of argon atoms is treated and it is verified that:

- an influence of the phase shift between the red field and the blue field over the trajectories of electrons is possible.
- the phase shift is controllable on the sub-cycle scale.

The intensities used in this chapter are estimated to be $2.6 \cdot 10^{14}\,\mathrm{W/cm^2}$ for the red field and $0.20 \cdot 10^{14}\,\mathrm{W/cm^2}$ for the blue field. The ratio between the amplitude of the electric field is therefore 0.28.

Mach-Zehnder interferometer delay

As mentioned in Chapter 3, the phase shift between the red and the blue component is introduced by applying a delay on one arm of the Mach-Zehnder interferometer (MZ), where the red component propagates. The delay precision is 12 nm [Erg06] corresponding to 80 as and it is to be compared with the 1.35 fs duration of the blue optical cycle. This correspond to a precision of $0.11\,\pi$ for the blue phase.

The MZ is aligned such that the best temporal overlap between the two components is achieved. From that position, the arm length of the MZ is varied over a distance of 40 nm leading to a time delay between 0 and 4.5 fs. 4.5 fs corresponds to 3.33 blue optical cycles.

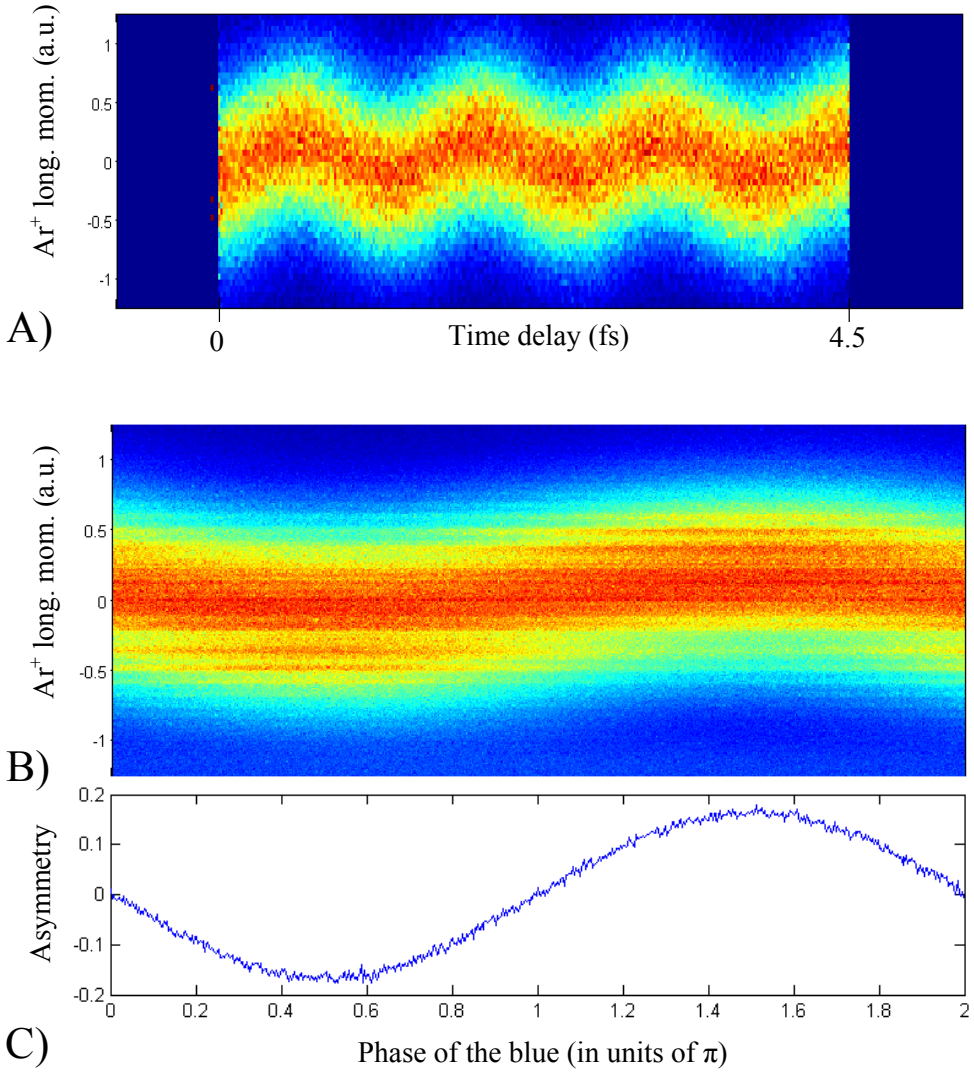

Figure 6.1: A) Longitudinal momentum of Ar^+ as a function of the MZ delay ranging from 0 to 4.5 fs, therefore being slightly larger than three optical cycles of the blue field. This measurement allows to compensate for the drift of the phase over time. By adding the data of the different optical cycles and adding the data over time, the longitudinal momentum of Ar^+ as a function of the phase (or equivalently, time delay) is given in B). C)Quantitative description of the asymmetry of panel C).

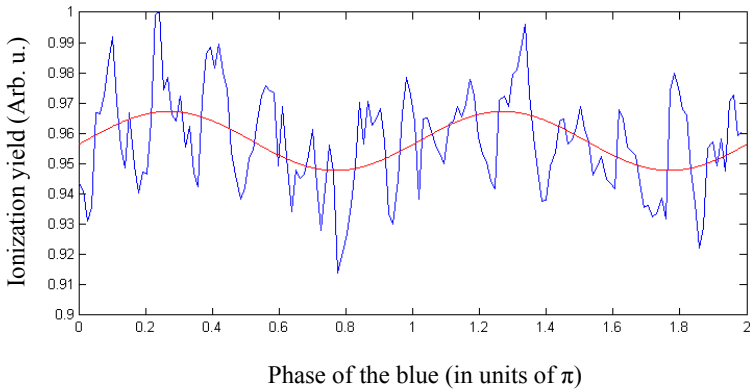

Figure 6.2: Ionization yield of Ar^+ as a function of the phase of the blue. Blue curve: experimental yield; red curve: sine fit to the experiment.

This span over few blue optical cycles allows to observe the entire range of the blue phase. In order to inspect the influence of the blue phase on the ionization of argon, we investigate the longitudinal momentum of the singly charged ion, as done in [XRK$^+$12]. In figure 6.1 B) the longitudinal momentum distribution as a function of the MZ delay is shown. A clear dependence of the ion momentum on the delay is seen. This dependence is following the phase of the blue field. The pattern observed is regular over the different blue optical cycles. This excludes the presence of fields other than the two components which would affect the periodicity observed in longitudinal momentum. As in the case of ultra-short laser pulses, the asymmetry observed for the singly charged ion is used to calibrate the phase drift over time. Due to the large distance (7 meters) between the MZ and the reaction microscope, small changes in the propagation properties, induce large changes of the phase. For instance, a change of one degree in air temperature from 20 to 21 degrees Celsius would lead to a delay of the red component by -22.12 fs and of the blue component by -22.68 fs, introducing a phase shift of $0.82\,\pi$. In the present case, "packets" of one hour measurements are analyzed and the phase is corrected for drift. The final longitudinal momentum graph is represented in panel C). The influence of the blue field on the longitudinal momentum is clearly visible. Also visible are structures/stripes for certain longitudinal momenta extending over a large phase range. This structure has been reported in [XRK$^+$12] as intra-cycle interferences. They emanate from interferences of the electronic wave packet ionized at different times within a single period of the laser pulses. Their presence has been reported experimentally for near-single laser pulses [Gop10] or two-color fields [XRK$^+$12]. The interpretation of this structures and their occurrence is not the subject of the present work. However, one should be concerned that such structure might change the correlation plot and introduce additional features.

One aim of the measurements on single ionization is to be able to relate the absolute phase shift between the blue and the red to the asymmetry observed in figure 6.1 C).

As mentioned in section 1.3.2 two effects contribute to the observed longitudinal momentum distribution and have to be considered:

- The ionization probability of an electron which depends on the electric field
- The momentum the free electron acquires from the laser field which depends on the vector potential

The determination of the absolute phase from the measured asymmetry is made complicated by this two contributions. We estimate this absolute phase shift between red and blue by looking at the ionization yield as a function of the phase. This is shown in figure 6.2. The counts for one phase are integrated over all momentum. The period of the variation is π because the yield is sensitive to the amplitude of the electric field in absolute value. A modulation of the yield of

few per cent is present. Following the ADK rate the theoretical maximum in ionization yield is located at phases 0 and π. The maxima of the ionization yield are placed at 0.24 and $1.24\,\pi$. The fact that they are not at the same phase value than the maxima of the asymmetry placed at 0.52 and $1.52\,\pi$ confirms that the asymmetry observed is not only influenced by the ionization yield. Both contributions from the electric and vector potential fields influence the number of particles having a given momentum.

This shows that ionization can be influenced by the superposition of the two fields. This investigation is applied to the trajectories leading to recollision and observation of rescattering electrons.

6.1.2 Electron emission asymmetries

The rescattered electrons are the electrons which, at the moment of recollision, back-scatter on the ion and are further accelerated by the field. In a single color field these trajectories lead to an energy reaching ten times the ponderomotive energy. This allows to differentiate them from the direct electron through their final energy. When the field is asymmetric, the different trajectories leading to rescattering result in a phase dependence that is different than for the direct electrons. This was shown already in the case of ultra-short laser pulses (cf. [PLW$^+$03] and picture 4.4 in Chapter 4) and demonstrated for a two-color field in [RCD$^+$11] for xenon atoms. Because the trajectories of rescattered electrons are similar to the trajectory of the electron inducing NSDI, it is of importance to investigate whether their motion can be controlled on a sub-cycle time scale.

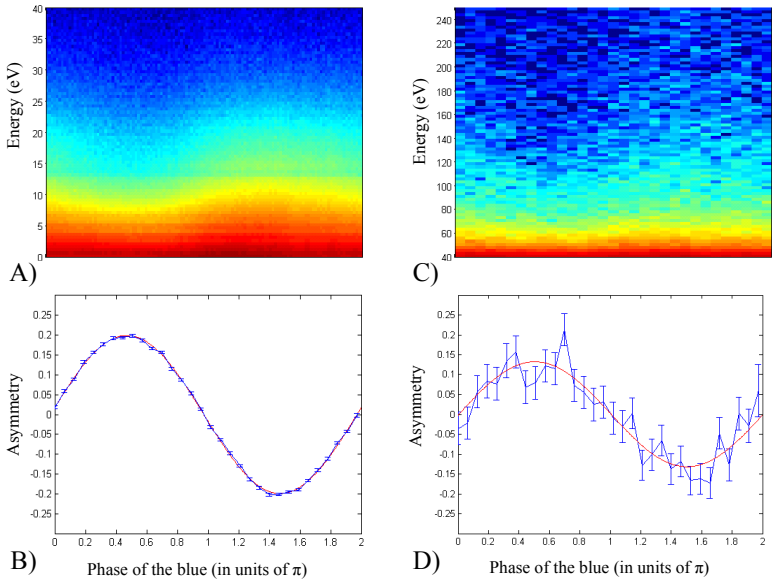

Figure 6.3: A,C) Energy distributions of the photo-electron from single ionization of argon as a function of the phase of the blue. The count scales are logarithmic. A) Energy scale between 0 and 40 eV. C) Energy scale between 40 and 250 eV. B,D) Asymmetry of the two energy regions as a function of the phase of the blue. B) Region between 0 and 40 eV. D) Region between 40 and 250 eV. The red solid lines are sine fit of the blue experimental curves.

In figure 6.3 the electron energy distribution (A,C) for single ionization of argon as a function of the phase is shown. Only one direction of electron emission (photo-electrons with negative momentum i.e. towards the ion detectors) is considered. Panel A) covers the energy range from 0 to 40 eV (1.5 a.u.). This last energy value is equal to the maximum energy that direct electrons can reach in the two-color field, 2.6 times the ponderomotive energy of the red field (equal to 15.0 eV).

Panel A) is simply a representation in energy of the asymmetry present in figure 6.1 B-C). The asymmetry of the electron in this energy range is shown below in panel B). Since the direct photo-electrons represents 99.3 % of the total amount of electrons, this asymmetry dependency is strictly the same than presented in figure 6.1 C) being the asymmetry for all energies. The sign of the function has changed because now the electrons are considered instead of the ions. In panel C), another energy range is taken into account, from 40 to 250 eV. This represents the energy range of the rescattering electron. From 40 eV a qualitative dependence and asymmetry of the distribution on the phase is present. For every energy value the distribution peaks around the value of $1.5\,\pi$. This is confirmed in graph D) which shows the asymmetry function of the photo-electrons in this energy range. The asymmetry has a very similar dependence on the phase than for less energetic electrons. The asymmetry distribution is maximum at 0.50 and $1.50\,\pi$ for higher energy electron, while at 0.45 and $1.45\,\pi$ in panel B) for lower energetic electrons. The asymmetry for the high energy region is lower than for the direct electrons showing a maximum value of 0.14. This is similar to results with ultra-short laser pulses where the value of asymmetry was comparable for both sort of electrons.

One remark is that due to the target dependence of the yield of the rescattered electron (cf. study of [PNX+94, RUB+08]) the structure in panel C) is not as clear as in [RCD+11] where ionization of xenon atoms is reported. Nonetheless, the momentum/energy distribution as a function of the phase demonstrates the possibility to control the trajectories of ionized electrons on a sub-cycle scale. By looking at the rescattering electrons we have demonstrated the applicability of this control scheme for NSDI, as described in the next part.

6.2 Double ionization

6.2.1 Ion momentum distributions

The dependence of the NSDI process on the asymmetric field is first investigated on the Ar^{2+} longitudinal momentum distribution. In figure 6.4 A) the ion longitudinal momentum distribution for all phases is shown. The double peak structure is not clearly visible instead a plateau ranging from -1.4 to +1.4 a.u. is present. This confirms that we are in the NSDI regime as expected from the intensity utilized (red: $2.6 \cdot 10^{14}\,\mathrm{W/cm^2}$, blue$0.20 \cdot 10^{14}\,\mathrm{W/cm^2}$). This is in accordance with the results presented in [dJFZ+04] and shown in figure 1.9. In the case of the ionization of argon by 800 nm laser pulses at an intensity of approximately $2.5 \cdot 10^{14}\,\mathrm{W/cm^2}$ the distribution presents a structure close to a plateau. This plateau transforms into a dip when using ultra-short laser pulses arguing for its origin in multiple recollisions. These multiple recollisions are not excluded in the present case since the duration of both pulses is also few tens of femtoseconds.

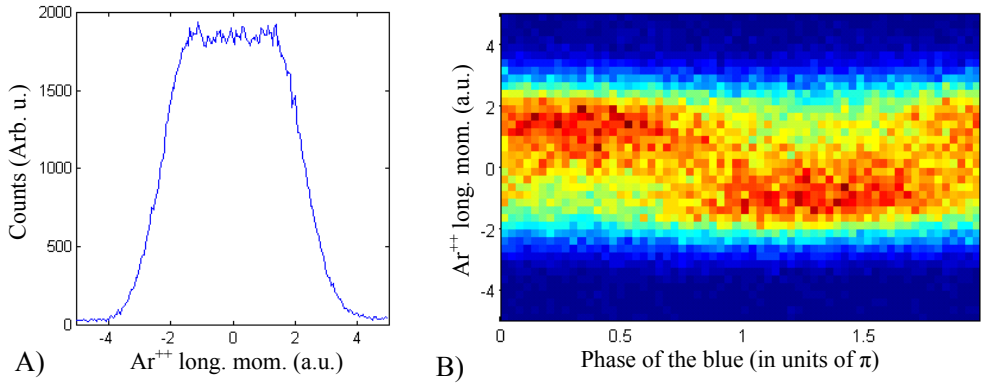

Figure 6.4: A) Longitudinal momentum distribution of Ar^{2+} for all phases. B) Longitudinal momentum distribution as a function of the phase of the blue field.

The evolution of this plateau structure as a function of the phase of the blue field is presented in panel B). Similarly to single ionization the distribution is influenced by the specific shape of the laser electric field for a given phase. The asymmetry of the distribution is shown in figure 6.5. The maximum value is comparable to the asymmetry value of Ar^+.

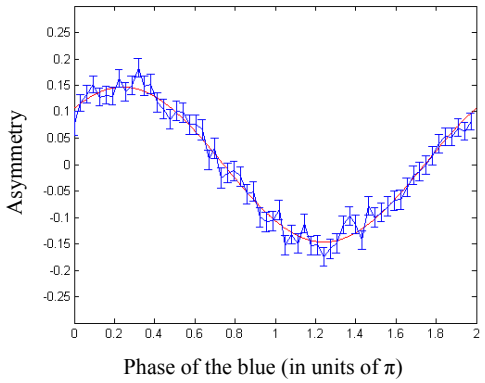

Figure 6.5: Asymmetry of the Ar^{2+} longitudinal momentum as a function of the phase of the blue field. The blue curve represents the experimental points and the red curve a sine fit to it.

6.2.2 Electron correlation

The two-electron correlation graph obtained in the case of the two-color experiment is shown in figure 6.6 A). The pattern resembles the so-called finger-like structure with the distribution located along the diagonal $p_{e1||} = p_{e2||}$ and a depletion in the center. In order to see the influence of the blue field on the correlation plot, the correlation graph is compared with a correlation graph of NSDI of argon with 800 nm, 25 fs pulses. This graph is presented in the same figure, panel B). The intensity for this single red field is higher than for the two color field and estimated to be $3.0 \cdot 10^{14}$ W.cm^2. On this graph, for a single color NSDI, the finger-like structure is also observed as predicted theoretically [YL10].

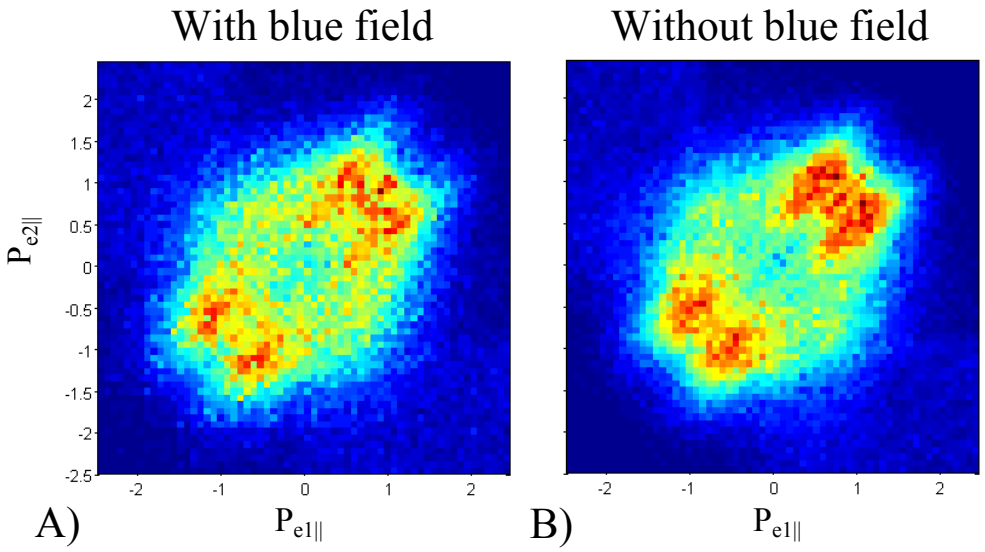

Figure 6.6: Correlation plot for NSDI of argon with (A) or without (B) additional blue field.

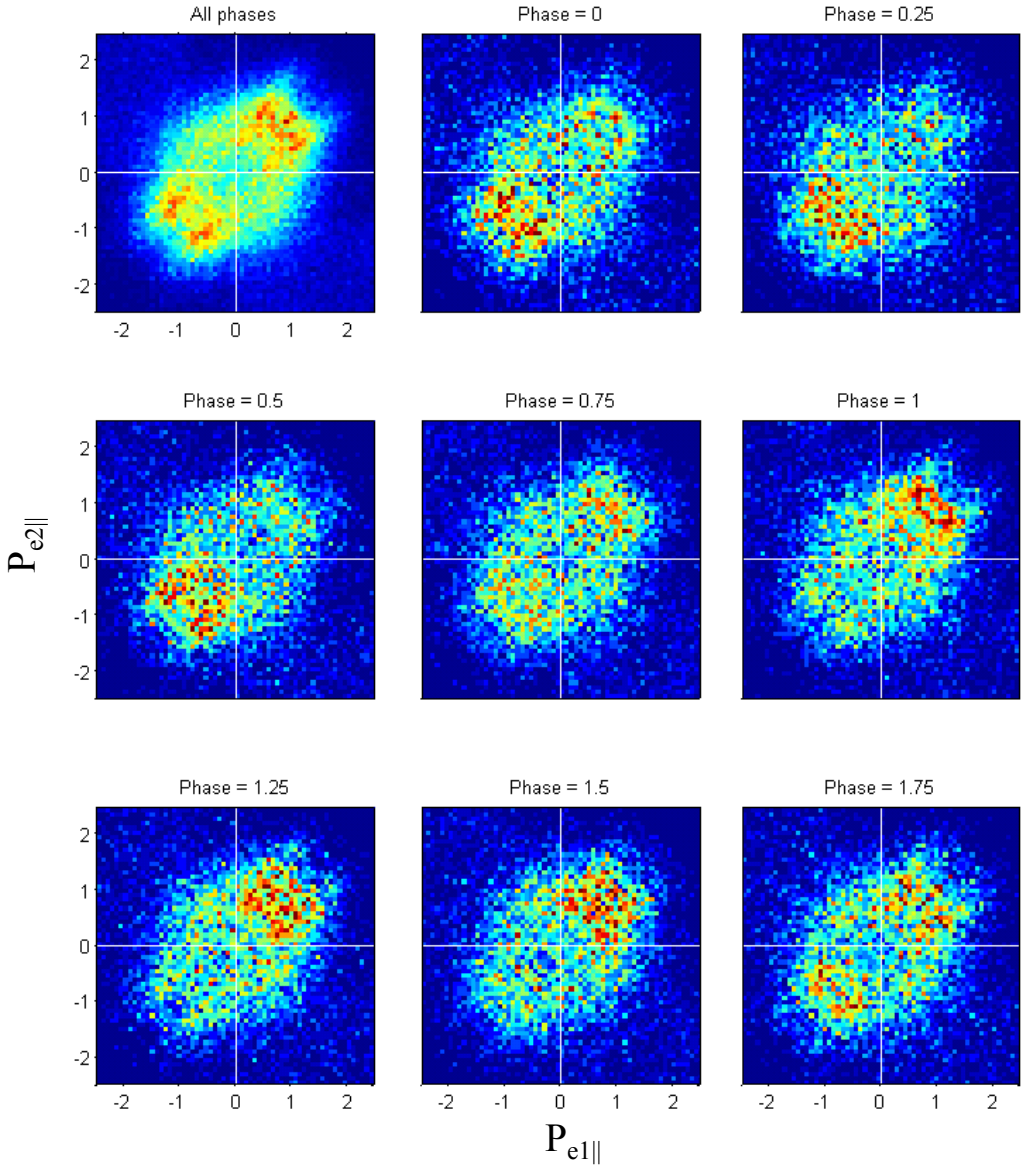

Figure 6.7: Correlation plot for NSDI of argon with different phase characteristics. Top left panel: all phases included. Phase selections are indicated on other panels with the phases given in value of π. The integration window around this central displayed value is $\pm 0.125\,\pi$. Note: the color scale are not shown for visual purpose. In panel with all phases the maximum number of counts goes to 125, in all other panels the maximum of the color scale is fixed to 17 counts.

The resemblance indicates that -for this choice of intensities- the blue field does not significantly affect the state of the system after recollision. The influence of the blue field can be seen on the correlation graphs obtained for different phase of the blue. They are displayed in figure 6.7. The top-left graph is the same than in figure 6.6 A), all phases are included. The other graphs have a phase selection. The interval for the phase selection is $\pm 0.125\,\pi$ around the central value which is indicated on top of each graph in π units. A clear variation on the distribution is seen with a change of phase. For increasing phase value, the distribution moves along the $p_{e1||} = p_{e2||}$ diagonal.

This change of pattern with the phase of the blue field demonstrates the possibility to control the electron trajectories with the laser field. This control is applicable in the case of the NSDI to influence the correlated dynamics between the electron.

Chapter 7

Conclusions and outlook

Advances in the control of intense laser fields have helped to gain deeper insight into the electron dynamics of atoms or molecules. One of the tools to study it is the electron recollision where the electric field of the laser forces an ionized electron to return to the ionic core and interact with it. In the framework of this thesis, we investigated the peculiar case where, upon the interaction with the ion, an additional electron is ionized providing the possibility to observe the dynamics of more than one electron at a time and study their correlation.

Through the utilization of ultra-short laser pulses, we were able to observe the process of non-sequential double ionization in the limit where the returning electron interacts with the ion only a single time. This allows us to identify the transition state of the atom directly after recollision but before the emission of both electrons. We have shown that by controlling the intensity of the laser we can induce the creation of doubly excited state after recollision. In addition, the dynamical properties of these state is extracted from the measured electron spectra. In order to control the formation of this intermediate state, an experimental aspect is the ability to control the electron trajectory with the shape of the laser electric field. This aspect was demonstrated by using CEP tagged few-cycles pulses or using two-color laser pulses.

To perform the experiment, the combination of a Reaction Microscope and a stereo-ATI spectrometer was realized. The latter enables the characterization of the ultra-short pulses. They originate from a Titanium:Sapphire laser system producing amplified 25 fs pulses. Through spectral broadening in a hollow-core fiber their duration was brought down to less than 6 fs with intensities as high as $10^{15}\,\mathrm{W/cm^2}$. These pulses were split into two parts and one went to the stereo-ATI spectrometer for tagging the CEP of every single pulse. The other part was used to ionize atoms inside a ReMi, which allows measuring the three-dimensional momentum vectors of all charged reaction fragments in coincidence. In the specific investigation of NSDI, it was applied for the determination of the momentum components along the laser polarization direction.

The analysis of ion momentum distributions permitted to prove the correct operation of the ReMi and the stereo-ATI and to ensure the observation of NSDI with ultra-short laser pulses. This was done through the analysis of the influence of the laser electric field shape (CEP value) on the single and double ionization of argon and neon atoms. The change of CEP was related to a change in the emission direction of the ions. An asymmetry in emission direction of the ion is present and particularly visible for double ionization where its value is of the order of 25 %. This asymmetry demonstrates the ability to control the electron recollision trajectories using ultra-short pulses.

In the main part of this thesis, we investigated the correlation between the two emitted electrons in non-sequential double ionization by looking at the distribution of one of the electron longitudinal momentum as a function of the other electron momentum. For argon at an intensity of $1.5 \cdot 10^{14}\,\mathrm{W/cm^2}$, a cross-shaped structure was observed. The obtained distribution is mainly populated on the axes and at the center of the graph. This indicates that for most of the events the momentum value of at least one of the electron is close to zero. Comparison with correlation graphs for longer pulse durations yields large differences. Here the correlation graphs exhibit a so-called finger-like or v-shaped structure showing a depletion at the center of the graph (i.e. for $p_{e1||} = p_{e2||} \approx 0$)

and the distributions peaking close to the $p_{e1||} = p_{e2||}$ diagonal. For the experiment with ultra-short pulses, the comparison with two types of theoretical models, one classical and one quantum mechanical, showed that such patterns indicate the excitation of the ion upon recollision.

The appearance of the structure described above, and its difference to results at longer pulse duration was also discussed. For this purpose we studied another target: neon atoms. We demonstrated that the correlation pattern for this atom was similar to the pattern obtained at longer pulse duration. This advocates for the observation of (e,2e)-like ionization independent of the pulse length for neon.

We investigated also the NSDI of argon at an intensity of $0.9 \cdot 10^{14}\,\mathrm{W/cm^2}$. By decreasing the intensity, the returning energy of the electron was lowered. The correlation pattern exhibits slightly different features: while the distribution is still populated in the center, it shows mainly two branches parallel to the $p_{e1||} = p_{e2||}$ diagonal. From the semi-classical model we developed to interpret the correlation measured, we confirm the excitation of the bound electron but at the cost of recapturing the returning electron. The transition state created is thus a doubly excited compound.

For this state, a strong correlation is observed between the ionization times of the electrons and their momentum. This feature is revealed by the semi-classical calculation and confirmed by simulating the classical evolution of a stable doubly excited atom in the laser field. The study showed that we can selectively create such a doubly excited state and deduce its decay time which is on the scale of hundred attoseconds.

Finally we have demonstrated the possibility to control the electron trajectories leading to NSDI in a different manner compared to CEP-tagged ultra-short laser pulses. By superimposing a frequency doubled component of the laser on the fundamental component we reported its influence on the trajectory of the ionized electron. On the one hand the blue field was strong enough for a control of the electron emission, on the other hand it did not affect the overall correlation patterns and so the specific recollision mechanism.

For future experiments, the control of this blue field on the electron trajectories can be altered to extract more information on the process. One possible change is to reduce the effect of the blue field to a simple probe field, if possible not influencing the single and double ionizations. This can be done by changing its polarization direction such that it is perpendicular to the polarization of the red field. In that configuration the electric field in the polarization direction of the red field is not modified. Instead, depending on the relative phase between the red and the blue field, some momentum is given to the electron in the transverse direction. The modulation of the transverse electron momentum with the phase of the blue indicates when the electron starts to "feel" the blue field and is related to its ionization time. For the recolliding electron, the lateral displacement, at the moment of recollision, acquired from the blue field depends on its excursion time. This additional field therefore selects the recollision trajectories. This selection scheme has already been applied for the study of high harmonic generation [EEN$^+$95, KKK$^+$05, BHS$^+$11, SSB$^+$12] and can be extended to rescattered electrons measured in single ionization and NSDI.

The most general idea to conclude about the possibility of the shaping of the electric field is to use ultra-short laser pulses. This would allow to observe single recollision which condition is not fulfilled for the presented two-color experiment. Experimentally, the ultra-short pulses have a sufficiently broad spectrum and no further harmonic generation is needed. The precise control of the electric shape of the field is done by splitting the different parts of the spectrum and affecting them a given delay [WHG$^+$11, ROA$^+$12]. By splitting the spectrum in hundreds of elements and using a pulse shaper to affect the phase of each spectral component, the control of the electric field can be extended to the zeptosecond scale ($10^{-21}\,\mathrm{s}$) [KWB$^+$11].

Finally, there would be many interest to retrieve the transverse components of both electrons in experiments with ultra-short laser pulses. This would add another observable to compare with theories and provides information on the electronic repulsion between the two emitted electrons [RdJE$^+$07]. Due to the temperature of the argon gas jet, the reconstruction of the transverse momentum was not viable here. One can use helium atoms which present a lower initial spread in momentum and so the possibility to reconstruct the transverse momentum of the second electron.

By improving the control and stability of the laser and the combination between the ReMi and the stereo-ATI such an experiment can be performed. In addition to the transverse momentum information, this would bring experimental results on the most theoretically studied system in NSDI.

Appendix A

Atomic units

In atomic physics the commonly used units systems is *atomic units*. The conversion factors are listed in the following tables.

Base units and natural constants

Quantity	Physical description
$r_e = 1\,a.u. = 5.2918 \cdot 10^{-11} m$	Bohr radius of the K-shell of hydrogen
$m_e = 1\,a.u. = 9.1095 \cdot 10^{-31} kg$	rest mass of the electron
$q_e = e = 1\,a.u. = 1.6022 \cdot 10^{-19} As$	charge of the electron
$\hbar = m_e v_e r_e = 1\,a.u.$	reduced Planck constant
$c = e^2/(\hbar\alpha) = 137\,a.u.$	speed of light

Other useful conversion are:

Conversion factors

energy	$E[eV] = 27.2 \cdot E[a.u.]$
momentum	$p[Ns] = 1.995 \cdot 10^{-24} \cdot p[a.u.]$
time	$t[s] = 4.134 \cdot 10^{16} \cdot t[a.u.]$
intensity of a laser field	$1\,a.u.$=$3.51 \cdot 10^{16}\,W/cm^2$
electric field	$1\,a.u.$=$5.142 \cdot 10^{11}\,V/m$
proton mass	$1\,amu$=$1823\,a.u.$

Bibliography

[AD97] MV Ammosov and NB Delone, *Tunneling ionization and above-barrier decay of atoms under the action of pulsed laser radiation*, LASER PHYSICS **7** (1997), no. 1, 79–83 (English), International Workshop on Laser Physics (LPHYS 96), MOSCOW, RUSSIA, JUL 22-26, 1996. 7

[ADK86] M.V. Ammosov, N.B. Delone, and V.P. Krainov, *Tunnel ionization of complex atoms and of atomic ions in an alternating electromagnetic field*, Sov. Phys. JETP **64** (1986), 1191–1194. 6

[AFM+79] P. Agostini, F. Fabre, G. Mainfray, G. Petite, and N. K. Rahman, *Free-free transitions following six-photon ionization of xenon atoms*, Phys. Rev. Lett. **42** (1979), 1127–1130. 6

[AMSC91] S. Augst, D. D. Meyerhofer, D. Strickland, and S. L. Chint, *Laser ionization of noble gases by coulomb-barrier suppression*, J. Opt. Soc. Am. B **8** (1991), no. 4, 858–867. 6

[APJ+09] Mark J Abel, Thomas Pfeifer, Aurélie Jullien, Phillip M Nagel, M Justine Bell, Daniel M Neumark, and Stephen R Leonei, *Carrier-envelope phase-dependent quantum interferences in multiphoton ionization*, Journal of Physics B: Atomic, Molecular and Optical Physics **42** (2009), no. 7, 075601. 63

[AUT+05] A. S. Alnaser, B. Ulrich, X. M. Tong, I. V. Litvinyuk, C. M. Maharjan, P. Ranitovic, T. Osipov, R. Ali, S. Ghimire, Z. Chang, C. D. Lin, and C. L. Cocke, *Simultaneous real-time tracking of wave packets evolving on two different potential curves in* $H_2{}^+$ *and* $D_2{}^+$, Phys. Rev. A **72** (2005), 030702. 2

[BC00] André D. Bandrauk and Szczepan Chelkowski, *Asymmetric electron-nuclear dynamics in two-color laser fields: Laser phase directional control of photofragments in* H_2^+, Phys. Rev. Lett. **84** (2000), 3562–3565. 26

[BHS+11] Leonardo Brugnera, David J. Hoffmann, Thomas Siegel, Felix Frank, Amelle Zaïr, John W. G. Tisch, and Jonathan P. Marangos, *Trajectory selection in high harmonic generation by controlling the phase between orthogonal two-color fields*, Phys. Rev. Lett. **107** (2011), 153902. 102

[BKJ+12] Boris Bergues, Matthias Kübel, Nora G. Johnson, Bettina Fischer, Nicolas Camus, Kelsie J. Betsch, Oliver Herrwerth, Arne Senftleben, A. Max Sayler, Tim Rathje, Thomas Pfeifer, Itzik Ben-Itzhak, Robert R. Jones, Gerhard G. Paulus, Ferenc Krausz, Robert Moshammer, Joachim Ullrich, and Matthias F. Kling, *Attosecond tracing of correlated electron-emission in non-sequential double ionization*, Nat Commun **3** (2012), 813–. 57, 63, 66, 67, 68, 69, 78

[BKP+04] T. Brixner, G. Krampert, T. Pfeifer, R. Selle, G. Gerber, M. Wollenhaupt, O. Graefe, C. Horn, D. Liese, and T. Baumert, *Quantum control by ultrafast polarization shaping*, Phys. Rev. Lett. **92** (2004), 208301. 4

[BLHE12] Wilhelm Becker, XiaoJun Liu, Phay Jo Ho, and Joseph H. Eberly, *Theories of photoelectron correlation in laser-driven multiple atomic ionization*, Rev. Mod. Phys. **84** (2012), 1011–1043. 14, 15

[Che11] Zhangjin Chen, *Validity of the quantitative rescattering model for two-color strong laser pulses*, Journal of Physics B: Atomic, Molecular and Optical Physics **44** (2011), no. 24, 245601. 27

[CK07] P. B. Corkum and Ferenc Krausz, *Attosecond science*, Nat Phys **3** (2007), no. 6, 381–387. 2

[CLL10] Zhangjin Chen, Yaqiu Liang, and C. D. Lin, *Quantitative rescattering theory of correlated two-electron momentum spectra for strong-field nonsequential double ionization of helium*, Phys. Rev. A **82** (2010), 063417. 13, 81

[CLML11] Zhangjin Chen, Yaqiu Liang, D. H. Madison, and C. D. Lin, *Strong-field nonsequential double ionization of ar and ne*, Phys. Rev. A **84** (2011), 023414. 13, 24

[Cor93] P. B. Corkum, *Plasma perspective on strong field multiphoton ionization*, Phys. Rev. Lett. **71** (1993), 1994–1997. 2, 7, 15, 16

[CZB01] Szczepan Chelkowski, Michel Zamojski, and André D. Bandrauk, *Laser-phase directional control of photofragments in dissociative ionization of* h_2^+ *using two-color intense laser pulses*, Phys. Rev. A **63** (2001), 023409. 26

[dJFZ+04] V L B de Jesus, B Feuerstein, K Zrost, D Fischer, A Rudenko, F Afaneh, C D Schröter, R Moshammer, and J Ullrich, *Atomic structure dependence of nonsequential double ionization of he, ne and ar in strong laser pulses*, Journal of Physics B: Atomic, Molecular and Optical Physics **37** (2004), no. 8, L161. 13, 14, 97

[dJRF+04] V.L.B. de Jesus, A. Rudenko, B. Feuerstein, K. Zrost, C.D. Schröter, R. Moshammer, and J. Ullrich, *Reaction microscopes applied to study atomic and molecular fragmentation in intense laser fields: non-sequential double ionization of helium*, Journal of Electron Spectroscopy and Related Phenomena **141** (2004), no. 2-3, 127 – 142, Frontiers of Coincidence Experiments. 3, 20, 21, 56

[DK91] N B Delone and V P Krainov, *Energy and angular electron spectra for the tunnel ionization of atoms by strong low-frequency radiation*, Journal of the Optical Society of America B **8** (1991), no. 6, 1207. 17

[DR06] Jean-Claude Diels and Wolfgang Rudolph, *Ultrashort laser pulse phenomena : Fundamentals, techniques, and applications on a femtosecond time scale*, Academic Press, 2006. 29

[EEN+95] H. Eichmann, A. Egbert, S. Nolte, C. Momma, B. Wellegehausen, W. Becker, S. Long, and J. K. McIver, *Polarization-dependent high-order two-color mixing*, Phys. Rev. A **51** (1995), R3414–R3417. 44, 102

[Ein17] A. Einstein, *Zur quantentheorie der strahlung*, Physikalische Zeitschrift **18** (1917), 121–128. 1

[ELR+03] E Eremina, X Liu, H Rottke, W Sandner, A Dreischuh, F Lindner, F Grasbon, G G Paulus, H Walther, R Moshammer, B Feuerstein, and J Ullrich, *Laser-induced non-sequential double ionization investigated at and below the threshold for electron impact ionization*, Journal of Physics B: Atomic, Molecular and Optical Physics **36** (2003), no. 15, 3269. 3, 65, 75, 78, 81

[EPBSZ10] Bruno Eckhardt, Jakub S. Prauzner-Bechcicki, Krzysztof Sacha, and Jakub Zakrzewski, *Phase effects in double ionization by strong short pulses*, Chemical Physics **370** (2010), 168 – 174. 25

[EPC+08] P. Eckle, A. N. Pfeiffer, C. Cirelli, A. Staudte, R. Dörner, H. G. Muller, M. Büttiger, and U. Keller, *Attosecond ionization and tunneling delay time measurements in helium*, Science **322** (2008), 1525–1529. 4, 17

[ERF+05] Th. Ergler, A. Rudenko, B. Feuerstein, K. Zrost, C. D. Schröter, R. Moshammer, and J. Ullrich, *Time-resolved imaging and manipulation of* h_2 *fragmentation in intense laser fields*, Phys. Rev. Lett. **95** (2005), 093001. 2

[ERF+06] ———, *Spatiotemporal imaging of ultrafast molecular motion: Collapse and revival of the* $D_2{}^+$ *nuclear wave packet*, Phys. Rev. Lett. **97** (2006), 193001. 2

[Erg06] T. Ergler, *Zeitaufgel¨oste untersuchungen zur fragmentationsdynamik von h2 (d2) in ultra-kurzen laserpulsen*, Ph.D. thesis, Heidelberg University, 2006. 45, 93

[FBCK92] D. N. Fittinghoff, P. R. Bolton, B. Chang, and K. C. Kulander, *Observation of nonsequential double ionization of helium with optical tunneling*, Phys. Rev. Lett. **69** (1992), 2642–2645. 3

[FBCK94] ———, *Polarization dependence of tunneling ionization of helium and neon by 120-fs pulses at 614 nm*, Phys. Rev. A **49** (1994), 2174–2177. 3, 39

[FCBS87] R. L. Fork, C. H. Brito Cruz, P. C. Becker, and C. V. Shank, *Compression of optical pulses to six femtoseconds by using cubic phase compensation*, Opt. Lett. **12** (1987), no. 7, 483–485. 1

[FdMFL11] C. Figueira de Morisson Faria and X. Liu, *Electron-electron correlation in strong laser fields*, Journal of Modern Optics **0** (2011), no. 0, 1–56. 11

[FdMFLBS04] C. Figueira de Morisson Faria, X. Liu, W. Becker, and H. Schomerus, *Coulomb repulsion and quantum-classical correspondence in laser-induced nonsequential double ionization*, Phys. Rev. A **69** (2004), 021402. 11

[FdMFLSL04] C. Figueira de Morisson Faria, X. Liu, A. Sanpera, and M. Lewenstein, *Classical and quantum-mechanical treatments of nonsequential double ionization with few-cycle laser pulses*, Phys. Rev. A **70** (2004), 043406. 11

[FdMFSLB04] C. Figueira de Morisson Faria, H. Schomerus, X. Liu, and W. Becker, *Electron-electron dynamics in laser-induced nonsequential double ionization*, Phys. Rev. A **69** (2004), 043405. 72

[FdMFSN12] C. Figueira de Morisson Faria, T. Shaaran, and M. T. Nygren, *Time-delayed nonsequential double ionization with few-cycle laser pulses: Importance of the carrier-envelope phase*, Phys. Rev. A **86** (2012), 053405. 57, 63, 68, 69, 70

[Fis10] Bettina Fischer, *Time resolved studies of* h_2^+ *dissociation with phase-stabalized laser pulses*, Ph.D. thesis, MPIK Heidelberg, 2010. 31, 36, 39

[FKP+10] Bettina Fischer, Manuel Kremer, Thomas Pfeifer, Bernold Feuerstein, Vandana Sharma, Uwe Thumm, Claus Dieter Schröter, Robert Moshammer, and Joachim Ullrich, *Steering the electron in h2+ by nuclear wave packet dynamics*, Phys. Rev. Lett. **105** (2010), no. 22, 223001. 4

[FLCC01] Li-Bin Fu, Jie Liu, Jing Chen, and Shi-Gang Chen, *Classical collisional trajectories as the source of strong-field double ionization of helium in the knee regime*, Phys. Rev. A **63** (2001), 043416. 16

[FMF+01] B. Feuerstein, R. Moshammer, D. Fischer, A. Dorn, C. D. Schröter, J. Deipenwisch, J. R. Crespo Lopez-Urrutia, C. Höhr, P. Neumayer, J. Ullrich, H. Rottke, C. Trump, M. Wittmann, G. Korn, and W. Sandner, *Separation of recollision mechanisms in nonsequential strong field double ionization of ar: The role of excitation tunneling*, Phys. Rev. Lett. **87** (2001), no. 4, 043003. 18, 65

[FWA+11] A. Fleischer, H. J. Wörner, L. Arissian, L. R. Liu, M. Meckel, A. Rippert, R. Dörner, D. M. Villeneuve, P. B. Corkum, and A. Staudte, *Probing angular correlations in sequential double ionization*, Phys. Rev. Lett. **107** (2011), 113003. 9

[GLW+10] E. Goulielmakis, Z. Loh, A. Wirth, R. Santra, N. Rohringer, V. S. Yakovlev, S. Zherebtsov, T. Pfeifer, A. M. Azzeer, M. F. Kling, S. R. Leone, and F. Krausz, *Real-time observation of valence electron motion*, Nature **466** (2010), no. 7307, 739–743. 9

[Gop10] Ram Gopal, *Electron wave packet interferences in ionization with few-cycle laser pulses and the dissociative photoionization of d2 with ultrashort extreme ultraviolet pulses*, Ph.D. thesis, Heidelberg University, 2010. 95

[Gou90] Gouy, *Sur une propriété nouvelle des ondes lumineuses.*, Comptes Rendus de l Académie des sciences **T1110** (1890), 1251. 51

[GSH+08] E. Goulielmakis, M. Schultze, M. Hofstetter, V. S. Yakovlev, J. Gagnon, M. Uiberacker, A. L. Aquila, E. M. Gullikson, D. T. Attwood, R. Kienberger, F. Krausz, and U. Kleineberg, *Single-cycle nonlinear optics*, Science **320** (2008), no. 5883, 1614–1617. 7

[Hal06] John L. Hall, *Nobel lecture: Defining and measuring optical frequencies*, Rev. Mod. Phys. **78** (2006), 1279–1295. 4

[HBKE06] S. L. Haan, L. Breen, A. Karim, and J. H. Eberly, *Variable time lag and backward ejection in full-dimensional analysis of strong-field double ionization*, Phys. Rev. Lett. **97** (2006), 103008. 20

[HKS+01] M. Hentschel, R. Kienberger, Ch. Spielmann, G. A. Reider, N. Milosevic, T. Brabec, P. Corkum, U. Heinzmann, M. Drescher, and F. Krausz, *Attosecond metrology*, Nature **414** (2001), no. 6863, 509–513. 3

[Hän06] Theodor W. Hänsch, *Nobel lecture: Passion for precision*, Rev. Mod. Phys. **78** (2006), 1297–1309. 4

[Hof09] Christian Hofrichter, *A stereo electron spectrometer for carrier-envelope phase measurements of few-cycle laser pulses*, Master's thesis, MPIK, 2009. 38, 63

[HPHE05] Phay J. Ho, R. Panfili, S. L. Haan, and J. H. Eberly, *Nonsequential double ionization as a completely classical photoelectric effect*, Phys. Rev. Lett. **94** (2005), 093002. 15, 16

[HSSP08] S L Haan, Z S Smith, K N Shomsky, and P W Plantinga, *Anticorrelated electrons from weak recollisions in nonsequential double ionization*, Journal of Physics B: Atomic, Molecular and Optical Physics **41** (2008), no. 21, 211002. 81

[HUH+00] R. Holzwarth, Th. Udem, T. W. Hänsch, J. C. Knight, W. J. Wadsworth, and P. St. J. Russell, *Optical frequency synthesizer for precision spectroscopy*, Phys. Rev. Lett. **85** (2000), 2264–2267. 4

[IW98] C. Iaconis and I.A. Walmsley, *Spectral phase interferometry for direct electric-field reconstruction of ultrashort optical pulses*, Opt. Lett. **23** (1998), no. 10, 792–794. 35

[JDR+00] David J. Jones, Scott A. Diddams, Jinendra K. Ranka, Andrew Stentz, Robert S. Windeler, John L. Hall, and Steven T. Cundiff, *Carrier-envelope phase control of femtosecond mode-locked lasers and direct optical frequency synthesis*, Science **288** (2000), no. 5466, 635–639. 4

[JHW+11] Nora G. Johnson, O. Herrwerth, A. Wirth, S. De, I. Ben-Itzhak, M. Lezius, B. Bergues, M. F. Kling, A. Senftleben, C. D. Schröter, R. Moshammer, J. Ullrich, K. J. Betsch, R. R. Jones, A. M. Sayler, T. Rathje, K. Rühle, W. Müller, and G. G. Paulus, *Single-shot carrier-envelope-phase-tagged ion-momentum imaging of nonsequential double ionization of argon in intense 4-fs laser fields*, Phys. Rev. A **83** (2011), no. 1, 013412. 24, 57, 58

[KBJ+12] M Kübel, K J Betsch, Nora G Johnson, U Kleineberg, R Moshammer, J Ullrich, G G Paulus, M F Kling, and B Bergues, *Carrier-envelope-phase tagging in measurements with long acquisition times*, New Journal of Physics **14** (2012), no. 9, 093027. 43, 57

[Kel65] L. V. Keldysh, *Ionization in the field of a strong electromagnetic wave*, JETP **47** (1965), 1307. 5

[KFF+09] Manuel Kremer, Bettina Fischer, Bernold Feuerstein, Vitor L. B. de Jesus, Vandana Sharma, Christian Hofrichter, Artem Rudenko, Uwe Thumm, Claus Dieter Schröter, Robert Moshammer, and Joachim Ullrich, *Electron localization in molecular fragmentation of h2 by carrier-envelope phase stabilized laser pulses*, Phys. Rev. Lett. **103** (2009), no. 21, 213003. 4

[KGU+04] R. Kienberger, E. Goulielmakis, M. Uiberacker, A. Baltuska, V. Yakovlev, F. Bammer, A. Scrinzi, Th. Westerwalbesloh, U. Kleineberg, U. Heinzmann, M. Drescher, and F. Krausz, *Atomic transient recorder*, Nature **427** (2004), no. 6977, 817–821. 17

[KHF+11] M. Kremer, C. Hofrichter, B. Fischer, V. Sharma, N. Camus, T. Pfeifer, R. Moshammer, and J. Ullrich, *Minimizing dispersive distortions in carrier-envelope phase sweeping with glass wedges*, Opt. Lett. **36** (2011), no. 8, 1455–1457. 36

[KI09] Ferenc Krausz and Misha Ivanov, *Attosecond physics*, Rev. Mod. Phys. **81** (2009), 163–234. 7

[KKK+05] I Jong Kim, Chul Min Kim, Hyung Taek Kim, Gae Hwang Lee, Yong Soo Lee, Ju Yun Park, David Jaeyun Cho, and Chang Hee Nam, *Highly efficient high-harmonic generation in an orthogonally polarized two-color laser field*, Phys. Rev. Lett. **94** (2005), 243901. 102

[Kre09] Manuel Kremer, *Einfluß der träger-einhüllenden-phase auf die wechselwirkung ultrakurzer laserpulse mit molekülen*, Ph.D. thesis, Heidelberg University, 2009. 35, 36

[KSV+06] M. F. Kling, Ch. Siedschlag, A. J. Verhoef, J. I. Khan, M. Schultze, Th. Uphues, Y. Ni, M. Uiberacker, M. Drescher, F. Krausz, and M. J. J. Vrakking, *Control of electron localization in molecular dissociation*, Science **312** (2006), no. 5771, 246–248. 4

[KT93] Daniel J. Kane and Rick Trebino, *Single-shot measurement of the intensity and phase of an arbitrary ultrashort pulse by using frequency-resolved optical gating*, Opt. Lett. **18** (1993), no. 10, 823–825. 35

[KTK+01] Masayuki Kakehata, Hideyuki Takada, Yohei Kobayashi, Kenji Torizuka, Yoshihiko Fujihira, Tetsuya Homma, and Hideo Takahashi, *Single-shot measurement of carrier-envelope phase changes by spectral interferometry*, Opt. Lett. **26** (2001), no. 18, 1436–1438. 35, 36

[KWB+11] Jens Köhler, Matthias Wollenhaupt, Tim Bayer, Cristian Sarpe, and Thomas Baumert, *Zeptosecond precision pulse shaping*, Opt. Express **19** (2011), no. 12, 11638–11653. 102

[LFdMF04] X. Liu and C. Figueira de Morisson Faria, *Nonsequential double ionization with few-cycle laser pulses*, Phys. Rev. Lett. **92** (2004), 133006. 23, 72

[LL77] L. D. Landau and E. M. Lifshitz, *Quantum mechanics*, Pergamon Press, 1977. 6

[LL10] Qing Liao and Peixiang Lu, *Energy correlation in above-threshold nonsequential double ionization at 800 nm*, Phys. Rev. A **82** (2010), 021403. 81

[LLMM82] A. L'Huillier, L. A. Lompre, G. Mainfray, and C. Manus, *Multiply charged ions formed by multiphoton absorption processes in the continuum*, Phys. Rev. Lett. **48** (1982), 1814–1817. 3, 7, 8, 47

[LLMM83] Anne L'Huillier, L. A. Lompre, G. Mainfray, and C. Manus, *Multiply charged ions induced by multiphoton absorption in rare gases at 0.53 μm*, Phys. Rev. A **27** (1983), no. 5, 2503–2512. 3

[LP79] J G Leopold and I C Percival, *Ionisation of highly excited atoms by electric fields. iii. microwave ionisation and excitation*, Journal of Physics B: Atomic and Molecular Physics **12** (1979), no. 5, 709. 79

[LPW+04] F. Lindner, G. G. Paulus, H. Walther, A. Baltuška, E. Goulielmakis, M. Lezius, and F. Krausz, *Gouy phase shift for few-cycle laser pulses*, Phys. Rev. Lett. **92** (2004), no. 11, 113001. 51

[LRE+04] X. Liu, H. Rottke, E. Eremina, W. Sandner, E. Goulielmakis, K. O. Keeffe, M. Lezius, F. Krausz, F. Lindner, M. G. Schätzel, G. G. Paulus, and H. Walther, *Nonsequential double ionization at the single-optical-cycle limit*, Phys. Rev. Lett. **93** (2004), no. 26, 263001. 4, 23

[LTC98] S Larochelle, A Talebpour, and S L Chin, *Non-sequential multiple ionization of rare gas atoms in a ti:sapphire laser field*, Journal of Physics B: Atomic, Molecular and Optical Physics **31** (1998), no. 6, 1201. 3

[LTR+08] Yunquan Liu, S. Tschuch, A. Rudenko, M. Dürr, M. Siegel, U. Morgner, R. Moshammer, and J. Ullrich, *Strong-field double ionization of ar below the recollision threshold*, Phys. Rev. Lett. **101** (2008), no. 5, 053001. 22, 75

[LYL+10] Yunquan Liu, Difa Ye, Jie Liu, A. Rudenko, S. Tschuch, M. Dürr, M. Siegel, U. Morgner, Qihuang Gong, R. Moshammer, and J. Ullrich, *Multiphoton double ionization of ar and ne close to threshold*, Phys. Rev. Lett. **104** (2010), no. 17, 173002. 19, 22, 70, 72, 75

[Mai60] T. H. Mainman, *Stimulated optical radiation in ruby*, Nature **187** (1960), no. 4736, 493–494. 1

[MCLL09] Samuel Micheau, Zhangjin Chen, Anh-Thu Le, and C. D. Lin, *Quantitative rescattering theory for nonsequential double ionization of atoms by intense laser pulses*, Phys. Rev. A **79** (2009), 013417. 13, 24, 57

[MCU09] F. Mauger, C. Chandre, and T. Uzer, *Strong field double ionization: The phase space perspective*, Phys. Rev. Lett. **102** (2009), 173002. 16, 79

[MCU10a] ———, *Dynamics of recollisions for the double ionization of atoms in intense laser fields*, Phys. Rev. A **81** (2010), 063425. 19, 79

[MCU10b] ———, *From recollisions to the knee: A road map for double ionization in intense laser fields*, Phys. Rev. Lett. **104** (2010), 043005. 79

[MFLU+02] R. Moshammer, B. Feuerstein, J. Crespo López-Urrutia, J. Deipenwisch, A. Dorn, D. Fischer, C. Höhr, P. Neumayer, C. D. Schröter, J. Ullrich, H. Rottke, C. Trump, M. Wittmann, G. Korn, and W. Sandner, *Correlated two-electron dynamics in strong-field double ionization*, Phys. Rev. A **65** (2002), 035401. 4

[MFS+00] R. Moshammer, B. Feuerstein, W. Schmitt, A. Dorn, C. D. Schröter, J. Ullrich, H. Rottke, C. Trump, M. Wittmann, G. Korn, K. Hoffmann, and W. Sandner, *Momentum distributions of neon+ ions created by an intense ultrashort laser pulse*, Phys. Rev. Lett. **84** (2000), no. 3, 447–450. 3, 47

[Mil88] D. R. Miller, *Free jet sources*, Atomic and Molecular Beam Methods (Giacinto Scoles, ed.), Oxford University Press, 1988, pp. 14–53. 50

[MKCU12] F. Mauger, A. Kamor, C. Chandre, and T. Uzer, *Mechanism of delayed double ionization in a strong laser field*, Phys. Rev. Lett. **108** (2012), 063001. 79

[MPBB06] D B Milosevic, G G Paulus, D Bauer, and W Becker, *Above-threshold ionization by few-cycle pulses*, Journal of Physics B: Atomic, Molecular and Optical Physics **39** (2006), no. 14, R203. 63

[MUF+03] R Moshammer, J Ullrich, B Feuerstein, D Fischer, A Dorn, C D Schröter, J R Crespo Lopez-Urrutia, C Höhr, H Rottke, C Trump, M Wittmann, G Korn, K Hoffmann, and W Sandner, *Strongly directed electron emission in non-sequential double ionization of ne by intense laser pulses*, Journal of Physics B: Atomic, Molecular and Optical Physics **36** (2003), no. 6, L113. 3, 72

[MUU+96] R. Moshammer, J. Ullrich, M. Unverzagt, W. Schmitt, P. Jardin, R. E. Olson, R. Dörner, V. Mergel, and H. Schmidt-Böcking, *The dynamics of target ionization by fast highly charged projectiles*, Nuclear Instruments and Methods in Physics Research Section B: Beam Interactions with Materials and Atoms **107** (1996), no. 1-4, 62 – 66, Swift Heavy Ions in Matter. 47

[NGS+08] T. Nubbemeyer, K. Gorling, A. Saenz, U. Eichmann, and W. Sandner, *Strong-field tunneling without ionization*, Phys. Rev. Lett. **101** (2008), 233001. 8

[Nor13] Bengt Norden, *Development of "femtochemistry" rewarded*, http://www.nobelprize.org/nobel_prizes/chemistry/laureates/1999/advanced-chemistryprize1999.pdf, 2013, Online; accessed 28-February-2013. 1

[NSS96] M. Nisoli, S. De Silvestri, and O. Svelto, *Generation of high energy 10 fs pulses by a new pulse compression technique*, Applied Physics Letters **68** (1996), no. 20, 2793–2795. 2

[OK11] Kotaro Okamura and Takayoshi Kobayashi, *Octave-spanning carrier-envelope phase stabilized visible pulse with sub-3-fs pulse duration*, Opt. Lett. **36** (2011), no. 2, 226–228. 2

[PBSEZ08] Jakub S. Prauzner-Bechcicki, Krzysztof Sacha, Bruno Eckhardt, and Jakub Zakrzewski, *Quantum model for double ionization of atoms in strong laser fields*, Phys. Rev. A **78** (2008), 013419. 22

[PCS+11a] Adrian N. Pfeiffer, Claudio Cirelli, Mathias Smolarski, Darko Dimitrovski, Mahmoud Abu-samha, Lars Bojer Madsen, and Ursula Keller, *Attoclock reveals natural coordinates of the laser-induced tunnelling current flow in atoms*, Nature Physics **8** (2011), 1–5. 7

[PCS+11b] Adrian N. Pfeiffer, Claudio Cirelli, Mathias Smolarski, Reinhard Dorner, and Ursula Keller, *Timing the release in sequential double ionization*, Nat Phys **7** (2011), no. 5, 428–433. 4, 9

[PDMT03] J S Parker, B J S Doherty, K J Meharg, and K T Taylor, *Time delay between singly and doubly ionizing wavepackets in laser-driven helium*, Journal of Physics B: Atomic, Molecular and Optical Physics **36** (2003), no. 21, L393. 9, 10

[PDT+06] J. S. Parker, B. J. S. Doherty, K. T. Taylor, K. D. Schultz, C. I. Blaga, and L. F. DiMauro, *High-energy cutoff in the spectrum of strong-field nonsequential double ionization*, Phys. Rev. Lett. **96** (2006), 133001. 9, 10, 20

[PEH01] Raphael Panfili, J. Eberly, and Stan Haan, *Comparing classical and quantum simulations of strong-field double-ionization*, Opt. Express **8** (2001), no. 7, 431–435. 15

[Pfl12] Thomas Pflüger, *Electron impact ionization studies of small rare gas clusters*, Ph.D. thesis, Heidelberg University, 2012. 49

[PGW+01] G G Paulus, F Grasbon, W Walther, P Villoresi, M Nisoli, S Stagira, E Priori, and De Silvestri, *Absolute-phase phenomena in photoionization with few-cycle laser pulses*, Nature **414** (2001), 182–184. 8

[PLW+03] G. G. Paulus, F. Lindner, H. Walther, A. Baltuška, E. Goulielmakis, M. Lezius, and F. Krausz, *Measurement of the phase of few-cycle laser pulses*, Phys. Rev. Lett. **91** (2003), 253004. 63, 96

[PM94] Michael D. Perry and Gerard Mourou, *Terawatt to petawatt subpicosecond lasers*, Science **264** (1994), no. 5161, 917–924. 2, 31

[PMMT07] J S Parker, K J Meharg, G A McKenna, and K T Taylor, *Single-ionization of helium at ti:sapphire wavelengths: rates and scaling laws*, Journal of Physics B: Atomic, Molecular and Optical Physics **40** (2007), no. 10, 1729. 9

[PNX+94] G. G. Paulus, W. Nicklich, Huale Xu, P. Lambropoulos, and H. Walther, *Plateau in above threshold ionization spectra*, Phys. Rev. Lett. **72** (1994), 2851–2854. 97

[PPt66] A. M. Peremolov, V. S. Popov, and M. V. terent'ev, *ionization of atoms in an alternating electric field*, Soviet Physics JETP **23** (1966), no. 5, 924–934. 6

[pri] *(private communication)*. 81

[RCD+11] D. Ray, Zhangjin Chen, S. De, W. Cao, I. V. Litvinyuk, A. T. Le, C. D. Lin, M. F. Kling, and C. L. Cocke, *Momentum spectra of electrons rescattered from rare-gas targets following their extraction by one- and two-color femtosecond laser pulses*, Phys. Rev. A **83** (2011), 013410. 26, 27, 96, 97

[RdJE+07] A. Rudenko, V. L. B. de Jesus, Th. Ergler, K. Zrost, B. Feuerstein, C. D. Schröter, R. Moshammer, and J. Ullrich, *Correlated two-electron momentum spectra for strong-field nonsequential double ionization of he at 800 nm*, Phys. Rev. Lett. **99** (2007), no. 26, 263003. 3, 4, 12, 20, 21, 47, 102

[REZ+08] A. Rudenko, Th. Ergler, K. Zrost, B. Feuerstein, V. L. B. de Jesus, C. D. Schröter, R. Moshammer, and J. Ullrich, *Intensity-dependent transitions between different pathways of strong-field double ionization*, Phys. Rev. A **78** (2008), no. 1, 015403. 75

[ROA+12] Philipp Raith, Christian Ott, Christopher P. Anderson, Andreas Kaldun, Kristina Meyer, Martin Laux, Yizhu Zhang, and Thomas Pfeifer, *Fractional high-order harmonic combs and energy tuning by attosecond-precision split-spectrum pulse control*, Applied Physics Letters **100** (2012), no. 12, 121104. 4, 102

[RUB+08] D. Ray, B. Ulrich, I. Bocharova, C. Maharjan, P. Ranitovic, B. Gramkow, M. Magrakvelidze, S. De, I. V. Litvinyuk, A. T. Le, T. Morishita, C. D. Lin, G. G. Paulus, and C. L. Cocke, *Large-angle electron diffraction structure in laser-induced rescattering from rare gases*, Phys. Rev. Lett. **100** (2008), 143002. 97

[RZF+04] A. Rudenko, K. Zrost, B. Feuerstein, V. L. B. de Jesus, C. D. Schröter, R. Moshammer, and J. Ullrich, *Correlated multielectron dynamics in ultrafast laser pulse interactions with atoms*, Phys. Rev. Lett. **93** (2004), 253001. 4, 75

[RZS+04] A Rudenko, K Zrost, C D Schröter, V L B de Jesus, B Feuerstein, R Moshammer, and J Ullrich, *Resonant structures in the low-energy electron continuum for single ionization of atoms in the tunnelling regime*, Journal of Physics B: Atomic, Molecular and Optical Physics **37** (2004), no. 24, L407. 61

[SBC+06] G. Sansone, E. Benedetti, F. Calegari, C. Vozzi, L. Avaldi, R. Flammini, L. Poletto, P. Villoresi, C. Altucci, R. Velotta, S. Stagira, S. De Silvestri, and M. Nisoli, *Isolated single-cycle attosecond pulses*, Science **314** (2006), no. 5798, 443–446. 4

[SE01] Krzysztof Sacha and Bruno Eckhardt, *Pathways to double ionization of atoms in strong fields*, Phys. Rev. A **63** (2001), no. 4, 043414. 81

[SFdMFS12] T. Shaaran, C. Figueira de Morisson Faria, and H. Schomerus, *Causality and quantum interference in time-delayed laser-induced nonsequential double ionization*, Phys. Rev. A **85** (2012), 023423. 69

[SFK+10] M. Schultze, M. Fieß, N. Karpowicz, J. Gagnon, M. Korbman, M. Hofstetter, S. Neppl, A. L. Cavalieri, Y. Komninos, Th. Mercouris, C. A. Nicolaides, R. Pazourek, S. Nagele, J. Feist, J. Burgdörfer, A. M. Azzeer, R. Ernstorfer, R. Kienberger, U. Kleineberg, E. Goulielmakis, F. Krausz, and V. S. Yakovlev, *Delay in photoemission*, Science **328** (2010), no. 5986, 1658–1662. 7

[SKS91] D. E. Spence, P. N. Kean, and W. Sibbett, *60-fsec pulse generation from a self-mode-locked ti:sapphire laser*, Opt. Lett. **16** (1991), no. 1, 42–44. 2, 31

[SLW+98] B. Sheehy, R. Lafon, M. Widmer, B. Walker, L. F. DiMauro, P. A. Agostini, and K. C. Kulander, *Single- and multiple-electron dynamics in the strong-field tunneling limit*, Phys. Rev. A **58** (1998), 3942–3952. 3

[SM85] Donna Strickland and Gerard Mourou, *Compression of amplified chirped optical pulses*, Optics Communications **55** (1985), no. 6, 447 – 449. 2, 31

[SNFdMF10] T. Shaaran, M. T. Nygren, and C. Figueira de Morisson Faria, *Laser-induced nonsequential double ionization at and above the recollision-excitation-tunneling threshold*, Phys. Rev. A **81** (2010), 063413. 12

[SRM+11a] A. M. Sayler, Tim Rathje, W. Müller, Ch. Kürbis, Klaus Rühle, Gero Stibenz, and G. G. Paulus, *Real-time pulse length measurement of few-cycle laser pulses using above-threshold ionization*, Opt. Express **19** (2011), no. 5, 4464–4471. 8, 23, 37, 40

[SRM+11b] A. M. Sayler, Tim Rathje, Walter Müller, Klaus Rühle, R. Kienberger, and G. G. Paulus, *Precise, real-time, every-single-shot, carrier-envelope phase measurement of ultrashort laser pulses*, Opt. Lett. **36** (2011), no. 1, 1–3. 39, 40, 42

[SRS+07] A. Staudte, C. Ruiz, M. Schöffler, S. Schössler, D. Zeidler, Th. Weber, M. Meckel, D. M. Villeneuve, P. B. Corkum, A. Becker, and R. Dörner, *Binary and recoil collisions in strong field double ionization of helium*, Phys. Rev. Lett. **99** (2007), 263002. 3, 20, 21

[SSB+12] Dror Shafir, Hadas Soifer, Barry D. Bruner, Michal Dagan, Yann Mairesse, Serguei Patchkovskii, Misha Yu. Ivanov, Olga Smirnova, and Nirit Dudovich, *Resolving the time when an electron exits a tunnelling barrier*, Nature **485** (2012), no. 7398, 343–346. 4, 25, 102

[SYDK93] K. J. Schafer, Baorui Yang, L. F. DiMauro, and K. C. Kulander, *Above threshold ionization beyond the high harmonic cutoff*, Phys. Rev. Lett. **70** (1993), 1599–1602. 7

[TDF12] Aihong Tong, Yongju Deng, and Guoqiang Feng, *Dependence of electron correlation on intensity ratio of orthogonal two-color laser pulses*, Optics Communications **285** (2012), no. 9, 2368 – 2372. 27

[TL05] X M Tong and C D Lin, *Empirical formula for static field ionization rates of atoms and molecules by lasers in the barrier-suppression regime*, Journal of Physics B: Atomic, Molecular and Optical Physics **38** (2005), no. 15, 2593. 67

[TZLY11] Qing-Bin Tang, Dong-Ling Zhang, Ying-Bin Li, and Ben-Hai Yu, *Role of nuclear coulomb attraction in nonsequential double ionization of argon atom*, Communications in Theoretical Physics **56** (2011), no. 5, 927. 66

[UMD+03] J Ullrich, R Moshammer, A Dorn, R Dörner, L Ph H Schmidt, and H Schmidt-Böcking, *Recoil-ion and electron momentum spectroscopy: reaction-microscopes*, Reports on Progress in Physics **66** (2003), no. 9, 1463. 3, 47

[WBS+03] M. Weckenbrock, A. Becker, A. Staudte, S. Kammer, M. Smolarski, V. R. Bhardwaj, D. M. Rayner, D. M. Villeneuve, P. B. Corkum, and R. Dörner, *Electron-electron momentum exchange in strong field double ionization*, Phys. Rev. Lett. **91** (2003), 123004. 4, 47

[WC11] H J Wörner and P B Corkum, *Imaging and controlling multielectron dynamics by laser-induced tunnel ionization*, Journal of Physics B: Atomic, Molecular and Optical Physics **44** (2011), no. 4, 041001. 9

[WGW+00] Th. Weber, H. Giessen, M. Weckenbrock, G. Urbasch, A. Staudte, L. Spielberger, O. Jagutzki, V. Mergel, M. Vollmer, and R. Dorner, *Correlated electron emission in multiphoton double ionization*, Nature **405** (2000), no. 6787, 658–661. 3, 9, 47

[WHG+11] A. Wirth, M. Th. Hassan, I. Grguras, J. Gagnon, A. Moulet, T. T. Luu, S. Pabst, R. Santra, Z. A. Alahmed, A. M. Azzeer, V. S. Yakovlev, V. Pervak, F. Krausz, and E. Goulielmakis, *Synthesized light transients*, Science **334** (2011), no. 6053, 195–200. 4, 7, 9, 102

[WHH+09] T. Wittmann, B. Horvath, W. Helml, M.G. Sch
"atzel, X. Gu, A.L. Cavalieri, GG Paulus, and R. Kienberger, *Single-shot carrier-envelope phase measurement of few-cycle laser pulses*, Nature Physics **5** (2009), no. 5, 357–362. 4

[WSD+94] B. Walker, B. Sheehy, L. F. DiMauro, P. Agostini, K. J. Schafer, and K. C. Kulander, *Precision measurement of strong field double ionization of helium*, Phys. Rev. Lett. **73** (1994), no. 9, 1227–1230. 3, 15

[WWS+00a] Th. Weber, M. Weckenbrock, A. Staudte, L. Spielberger, O. Jagutzki, V. Mergel, F. Afaneh, G. Urbasch, M. Vollmer, H. Giessen, and R. Dörner, *Recoil-ion momentum distributions for single and double ionization of helium in strong laser fields*, Phys. Rev. Lett. **84** (2000), no. 3, 443–446. 3, 47

[WWS+00b] Th Weber, M Weckenbrock, A Staudte, L Spielberger, O Jagutzki, V Mergel, F Afaneh, G Urbasch, M Vollmer, H Giessen, and R Dörner, *Sequential and nonsequential contributions to double ionization in strong laser fields*, Journal of Physics B: Atomic, Molecular and Optical Physics **33** (2000), no. 4, L127. 3

[WZS+04] M. Weckenbrock, D. Zeidler, A. Staudte, Th. Weber, M. Schöffler, M. Meckel, S. Kammer, M. Smolarski, O. Jagutzki, V. R. Bhardwaj, D. M. Rayner, D. M. Villeneuve, P. B. Corkum, and R. Dörner, *Fully differential rates for femtosecond multiphoton double ionization of neon*, Phys. Rev. Lett. **92** (2004), no. 21, 213002. 4, 20, 47, 72

[XRK+12] Xinhua Xie, Stefan Roither, Daniil Kartashov, Emil Persson, Diego G. Arbó, Li Zhang, Stefanie Gräfe, Markus S. Schöffler, Joachim Burgdörfer, Andrius Baltuška, and Markus Kitzler, *Attosecond probe of valence-electron wave packets by subcycle sculpted laser fields*, Phys. Rev. Lett. **108** (2012), 193004. 4, 95

[XYL10] G. G. Xin, D. F. Ye, and J. Liu, *Dependence of the correlated-momentum patterns in double ionization on the carrier-envelope phase and intensity of a few-cycle laser pulse*, Phys. Rev. A **82** (2010), 063423. 20, 22, 24, 77, 79

[YCL08] D. F. Ye, J. Chen, and J. Liu, *Classical trajectory perspective on double-ionization dynamics of diatomic molecules irradiated by ultrashort intense laser pulses*, Phys. Rev. A **77** (2008), no. 1, 013403. 22, 77, 79

[YL10] D. F. Ye and J. Liu, *Strong-field double ionization at the transition to below the recollision threshold*, Phys. Rev. A **81** (2010), 043402. 22, 66, 70, 79, 81, 84, 98

[YLL08] D. F. Ye, X. Liu, and J. Liu, *Classical trajectory diagnosis of a fingerlike pattern in the correlated electron momentum distribution in strong field double ionization of helium*, Phys. Rev. Lett. **101** (2008), 233003. 20, 21, 70, 77, 79

[Zew88] Ahmed H. Zewail, *Laser femtochemistry*, Science **242** (1988), no. 4886, 1645–1653. 1

[Zew00] ———, *Femtochemistry: Atomic-scale dynamics of the chemical bond*, The Journal of Physical Chemistry A **104** (2000), no. 24, 5660–5694. 1

[ZHT+11] Yueming Zhou, Cheng Huang, Aihong Tong, Qing Liao, and Peixiang Lu, *Correlated electron dynamics in nonsequential double ionization by orthogonal two-color laser pulses*, Opt. Express **19** (2011), no. 3, 2301–2308. 27

[ZLZ+10] Yueming Zhou, Qing Liao, Qingbin Zhang, Weiyi Hong, and Peixiang Lu, *Controlling nonsequential double ionization via two-color few-cycle pulses*, Opt. Express **18** (2010), no. 2, 632–638. 27

[ZQC+10] Yue-Ming Zhou, Liao Qing, Huang Cheng, Tong Ai-Hong, and Lu Pei-Xiang, *Electron correlation in nonsequential double ionization of helium by two-color pulses*, Chinese Physics Letters **27** (2010), no. 12, 123201. 27

Acknowledgements

Finally, my sincere thanks are given to all those without whom this work would not have been possible.
First of all, I would like to thank the head of this group at my arrival at the Max-Planck-Institute für Kernphysik, Joachim Ullrich, who gave me the opportunity to stay in a very exciting environment for studying atomic physics, not only because of the best infrastructure and equipment one can imagine, but also due to an excellent working atmosphere. He always took care that research would be conducted in the best direction and always managed to induce motivation.
My best regards go to my direct supervisor Robert Moshammer. Comes first all the wise advices or time helping in the lab to solve the technical issues encountered along these three years. Even more importantly, he taught me how to conduct a work as close as possible to what one expects from an experimental physicist. Particularly: always being critical with your experimental data and questioning what possible errors could appear and also being able to explain and present them in an intelligible way.
I would also like to express my gratitude to Thomas Pfeifer. He substantially contributed to the solution of technical issues and to data interpretation, which finally led to what is presented in this manuscript. Among all his qualities, his contagious enthusiasm and passion for scientific matters may be the most important.
I would also like to thank all those with whom I shared long hours in the lab trying to run the experiments. Up until the end I can really say that I enjoyed working with them and that I learned from everybody. In my first steps running the laser, the stereo-ATI and the reaction microscope, I was very lucky to benefit considerably from the generation preceding me: Manuel, Bettina and Vandana. They all have tremendous contributions in me being able to couple ultra-short laser pulses into the reaction microscope and recording particles momentum. I really also enjoyed working with Lutz, who chronologically came after me but was always full of resource and good mood helping to overcome problems and stress.
Experimentally, I am also largely indebted to Claus Dieter Schröter and Bernd Knap whose contributions are maybe not directly visible in the final experimental results but who helped considerably in fixing everyday bugs in the lab, I therefore thank them here.
I also thank Andreas Krupp for the nice time working together.
Finally, I would like to show my appreciation to my office colleagues, Thomas and Johannes, whose jokes and discussions always helped me to surmount less appreciable moments of the PhD, and to everyone in the group, with a special mention to the Konni's and the Pfeifer's guys, with whom I also spend a lot of time outside the institute walls.
I express my thanks to the people of the groups of Mathias Kling and of Jens Biegert. It was a real pleasure to collaborate with them and share joy and grief inherent to beam times.
Last but not least, I would like to express my thanks to all the people who did not participate in any scientific matter, but helped my during my life in Heidelberg. On top of the list, Linda who help me with every other aspect of my life and was always a source of support. Vincent, from whom entertainment never failed. Jens, without whom my integration in Heidelberg would have been difficult.
I would also like to thank more remote people, my parents, who always sustain me in all matters and help me achieving my choices and my brother encouraging and pushing me.